frontiers in Molecular Neuroscience

ORIGINAL RESEARCH
published: 06 April 2018
doi: 10.3389/fnmol.2018.00113

The LILI Motif of M3-S2 Linkers Is a Component of the NMDA Receptor Channel Gate

Marek Ladislav[1,2†], *Jiri Cerny*[1†], *Jan Krusek*[1], *Martin Horak*[1], *Ales Balik*[1*] *and Ladislav Vyklicky*[1*]

[1]Department of Cellular Neurophysiology, Institute of Physiology of the Czech Academy of Sciences, Prague, Czechia,
[2]Department of Physiology, Faculty of Science, Charles University in Prague, Albertov, Czechia

N-methyl-D-aspartate receptors (NMDARs) mediate excitatory synaptic transmission in the central nervous system, underlie the induction of synaptic plasticity, and their malfunction is associated with human diseases. Native NMDARs are tetramers composed of two obligatory GluN1 subunits and various combinations of GluN2A-D or, more rarely, GluN3A-B subunits. Each subunit consists of an amino-terminal, ligand-binding, transmembrane and carboxyl-terminal domain. The ligand-binding and transmembrane domains are interconnected via polypeptide chains (linkers). Upon glutamate and glycine binding, these receptors undergo a series of conformational changes leading to the opening of the Ca^{2+}-permeable ion channel. Here we report that different deletions and mutations of amino acids in the M3-S2 linkers of the GluN1 and GluN2B subunits lead to constitutively open channels. Irrespective of whether alterations were introduced in the GluN1 or the GluN2B subunit, application of glutamate or glycine promoted receptor channel activity; however, responses induced by the GluN1 agonist glycine were larger, on average, than those induced by glutamate. We observed the most prominent effect when residues GluN1(L657) and GluN2B(I655) were deleted or altered to glycine. In parallel, molecular modeling revealed that two interacting pairs of residues, the LILI motif (GluN1(L657) and GluN2B(I655)), form a functional unit with the TTTT ring (GluN1(T648) and GluN2B(T647)), described earlier to control NMDAR channel gating. These results provide new insight into the structural organization and functional interplay of the LILI and the TTTT ring during the course of NMDAR channel opening and closing.

Keywords: glutamate receptor gating, electrophysiology, spontaneous activity, channel open probability, protein block alphabet, molecular modeling

OPEN ACCESS

Edited by:
Argentina Lario Lago, University of California, San Francisco, United States

Reviewed by:
Antonio Rodriguez Moreno, Universidad Pablo de Olavide, Spain
John J. Woodward, Medical University of South Carolina, United States

***Correspondence:**
Ales Balik
ales.balik@fgu.cas.cz
Ladislav Vyklicky
ladislav.vyklicky@fgu.cas.cz

†*Co-first authors.*

Received: *22 January 2018*
Accepted: *22 March 2018*
Published: *06 April 2018*

Citation:
Ladislav M, Cerny J, Krusek J, Horak M, Balik A and Vyklicky L (2018) The LILI Motif of M3-S2 Linkers Is a Component of the NMDA Receptor Channel Gate. Front. Mol. Neurosci. 11:113. doi: 10.3389/fnmol.2018.00113

Abbreviations: 7CKA, 7-Chlorokynurenic acid; AA, amino acid; DTNB, 5,5′-dithiobis(2-nitrobenzoic acid); DTT, dithiothreitol; ECS, extracellular solution; HEK, human embryonic kidney; iGluRs, glutamate-activated ionotropic receptors; LBD, ligand-binding domain; MCT, mean closed time; MOT, mean open time; NMDAR, N-methyl-D-aspartate receptor; Po, channel open probability; RI_{Glu}, relative glutamate current; RI_{Gly}, relative glycine current; RI_{Spont}, relative spontaneous current; TMD, transmembrane domain; WT, wild-type.

INTRODUCTION

Excitatory signal transduction in the mammalian brain is primarily mediated by glutamate-activated ionotropic receptors (iGluRs) represented by α-amino-3-hydroxyl-5-methyl-4-isoxazole-propionate (AMPA), kainate and N-methyl-D-aspartate receptor (NMDAR) subtypes (Dingledine et al., 1999; Traynelis et al., 2010). Virtually all CNS circuits employ NMDAR-mediated excitatory postsynaptic current to regulate physiological functions and, in addition, this component has been implicated in various forms of synaptic plasticity thought to underly learning and memory formation (Dingledine et al., 1999; Lynch, 2004). In addition to NMDAR-mediated postsynaptic Ca^{2+} current, unconventional presynaptic NMDARs were identified at several types of synapses, where they modulate presynaptic neurotransmitter release (Dore et al., 2017; Bouvier et al., 2018). Part of this NMDAR action is Ca^{2+}-insensitive metabotropic signal transduction where a conformation change in the cytoplasmatic part of receptor activates an intracellular signaling pathway. Postsynaptically, metabotropic NMDAR signaling is capable to trigger long-term depression of synaptic transmission (Nabavi et al., 2013; Dore et al., 2016).

Native NMDARs are tetramers assembled from two obligatory glycine-binding GluN1 subunits in combination with two glutamate-binding GluN2A-D or glycine-binding GluN3A-B subunits (Ulbrich and Isacoff, 2008; Traynelis et al., 2010). Like other iGluR subunits, NMDAR subunits exhibit a conserved domain organization. The most distal part to the cell membrane is the amino-terminal domain linked to the ligand-binding domain (LBD), which is connected to the transmembrane domain (TMD) which, in turn, is connected to the intracellular carboxy domain (Traynelis et al., 2010). The clamshell-like LBD (S1 and S2 lobes) and the TMD, composed of M1-M4 transmembrane helices, are central to receptor function. The heteromeric LBD dimer forms a tight interface at the level of the S1 lobes while the bottom S2 lobes remain relatively mobile without a significant intradimer dimerization contact. Interdimer interfaces encompass residue contacts in upper (S1) and lower (S2) lobe (Furukawa et al., 2005; Karakas and Furukawa, 2014; Lee et al., 2014). Agonist binding evokes movement at the level of the S2 lobe (Furukawa et al., 2005; Yao et al., 2013) and it was suggested that agonist-induced conformation changes impact three polypeptide linkers connecting to the TMD forming the ion channel (Karakas and Furukawa, 2014). Recent structural data indicate that NMDAR agonist activation involves a rearrangement of inter-LBD interfaces (Tajima et al., 2016; Zhu et al., 2016). Based on the analysis of the available crystal structures of NMDAR and of isolated LBD structures, the clamshell-like displacement of the S2 with respect to the S1 is relatively small and insufficient to explain the magnitude of the displacement at the level of the TMD.

Channel opening is the key step in the NMDAR gating that allows the flux of ions including Ca^{2+} across the membrane. Crystal structures of the NMDAR with glutamate and glycine bound indicate that the M3 helices of the TMD tightly surround the central ion channel axis (closed conformation) and the M1 and M4 helices are much less packed at the periphery (Karakas and Furukawa, 2014; Lee et al., 2014). Several lines of evidence indicate that a rearrangement of M3 helices in the activated conformation of the receptor makes the central cavity of the channel accessible to ions, therefore implying a crucial role of the M3-S2 linkers in channel opening (Sobolevsky et al., 2004).

Modular composition, with linkers connecting functional domains, is a common characteristic of membrane-located ion channels. For BK potassium channel it has been shown that the length of the linker between the ion channel and the intracellular regulatory domain impacts channel activity. The probability of channel opening increased in presence of a shorter linker and decreased when the linker was extended by additional amino acids (AA; Niu et al., 2004). The concept of mechanical coupling between the LBD and the M3 helix in ionotropic glutamate receptors has been tested by artificial extension of GluN1 and GluN2A M3-S2 linkers with glycine residues inserted into the distal part of the linkers (in the proximity of the LBD) and the activity of mutated NMDAR was significantly impaired (Kazi et al., 2014). Open probability (Po) of the ion channel decreased with the extended linker length; however, this was subunit specifical, indicating distinct roles of the two subunits in the process of channel opening, where the GluN1 subunit mainly regulates the duration of the opening while the GluN2 subunit impacts the frequency of opening (Kazi et al., 2014). The opposite approach, where the length of the linker was reduced by deletion (GluN1(ΔT648) and GluN2A(ΔT644)) the Po was unaffected or decreased, respectively. Simultaneously performed homology modeling led to ambiguous results (Kazi et al., 2014). Moreover, previously published data showed that mutations of specific amino acids in the M3 helix and its proximity (the TMD part of the M3-S2 linker) induce various degrees of spontaneous NMDAR activity. Constitutively open channels were identified in SYTANLAAF motif (S = 1, F = 9) where T3A, A4C and A7C were mutated in the GluN1 subunit, and A3C and A7C in GluN2 subunits (Jones et al., 2002; Kashiwagi et al., 2002; Sobolevsky et al., 2007; Chang and Kuo, 2008; Xu et al., 2012).

The structure of the M3-S2 linkers and the related ends of the M3 helices has not been determined with high resolution in the solved crystal and cryo-EM structures, preventing clear understanding of how their structure and function contribute to the ion channel gating at the atomic level (Karakas and Furukawa, 2014; Lee et al., 2014; Tajima et al., 2016; Zhu et al., 2016). Structural data, however, indicate that the M3-S2 linkers adopt different orientations—while the GluN1 M3-S2 linkers are almost parallel with the longitudinal receptor axis, the GluN2 M3-S2 linkers are parallel with the membrane (Karakas and Furukawa, 2014; Lee et al., 2014). This suggests different roles of the GluN1 and the GluN2 subunits in channel gating and may contribute to the understanding of the specific molecular mechanism of allosteric coupling between the glutamate- and glycine-binding sites (Mayer et al., 1989).

The goal of this study was to determine the role of the M3-S2 linkers in NMDAR gating. Our results indicate that a

novel structural motif formed by two pairs of GluN1(L657) and GluN2B(I655) residues (LILI motif) located at the transition of M3 helices to S2 linkers are functionally linked with the TTTT ring located within the NMDAR channel pore to control channel gating.

MATERIALS AND METHODS

Transfection and Maintenance of Cells

Human embryonic kidney (HEK 293T) cells (American Type Culture Collection, ATTC No. CRL1573, Rockville, MD, USA) were cultured in Opti-MEM I (Invitrogen, Carlsbad, CA, USA) with 5% fetal bovine serum (PAN Biotech, Aidenbach, Germany) at 37°C in 5% CO_2. The day before transfection, the cells were plated in 24-well plates at a density of 2×10^5 cells per well. The next day, the cells were transfected with expression vectors containing wild-type (WT) or mutated glutamate receptor subunit GluN1–1a (GluN1; GenBank accession no. U08261) and GluN2B(GenBank accession no. M91562) and GFP (green fluorescent protein; pQBI 25, Takara, Tokyo, Japan) genes. Briefly, equal amounts (0.25 mg) of cDNAs encoding for GluN1, GluN2B and GFP were mixed with 0.9 μL of Matra-A Reagent (IBA, Göttingen, Germany) and added to confluent HEK 293T cells. After trypsinization, the cells were resuspended in Opti-MEM I containing 1% fetal bovine serum supplemented with 15 mM $MgCl_2$, 1 mM D, L-2-amino-5-phosphonovaleric acid and 1 μM ketamine, and plated on 30 mm poly-L-lysine-coated glass coverslips. Transfected cells were revealed by GFP epifluorescence.

Site-directed mutagenesis was performed using the QuikChange Site-Directed Mutagenesis Kit (Agilent Technologies, Santa Clara, CA, USA) in accordance with the instructions of the manufacturer, using manually designed primers purchased from Sigma-Aldrich. DpnI-treated PCR reaction was transformed into competent XL10-Gold *E. coli* cells, positive clones were selected, and isolated DNA plasmids were sequenced. All mutations were verified by DNA sequencing (SEQme, Dobris, Czech Republic and/or Eurofins Genomics, Germany). Amino acids are numbered according to the full-length protein, including the signal peptide, with the initiating methionine as number 1.

Electrophysiological Recording

Experiments were performed 18–48 h after the end of transfection on cultured HEK 293T cells transfected with vectors containing GluN1/GluN2B/GFP. Whole-cell and single-channel activity were recorded at room temperature using a patch-clamp amplifier (Axopatch 200A; Molecular Devices, Sunnyvale, CA, USA). Agonist-induced whole-cell responses were low-pass filtered at 2 kHz with a 4-pole Bessel filter (Frequency Devices, Haverhill, MA, USA), sampled at 5 kHz, and analyzed using pClamp software version 10 (Molecular Devices). Patch pipettes (3–6 MΩ) were pulled from borosilicate glass and filled with an intracellular solution containing (in mM): 120 gluconic acid, 15 CsCl, 10 BAPTA, 10 HEPES, 3 $MgCl_2$, 1 $CaCl_2$ and 2 ATP-Mg^{2+} salt (pH adjusted to 7.2 with CsOH). Extracellular solution (ECS) contained the following (in mM): 160 NaCl, 2.5 KCl, 10 HEPES, 10 glucose, 0.2 EDTA and 0.7 $CaCl_2$ (pH adjusted to 7.3 with NaOH).

Steady-state single-channel recordings using the cell-attached patch-clamp technique at room temperature were analog-filtered at 10 kHz with a 4-pole Bessel filter and sampled at 25 kHz. Standard bath solution was the same as the control solution in the whole-cell recording. Thick-wall borosilicate patch pipettes were pulled and fire-polished achieving resistances between 12 MΩ and 25 MΩ when measured in the bath and filled with an ECS containing (in mM): 160 NaCl, 2.5 KCl, 1 mM EDTA and 10 HEPES (pH-adjusted to 8.0 with NaOH) as well as 0.1 glycine and 1 glutamate. Recordings were performed at a very low concentration of protons and in the absence of divalent ions (1 mM EDTA) to negate any differences in sensitivity to these modulators (Popescu and Auerbach, 2003; Amico-Ruvio and Popescu, 2010). Inward openings were detected by applying a pipette potential of +100 mV.

Analysis of single-channel cell-attached records was performed in Nicolai and Sachs (2013). According to Colquhoun and Hawkes (1990), we chose records that were sufficiently long (>5000 events) and entirely free of overlapping openings, which indicated high confidence (99%) of measuring single-channel activity. The lowest Po we observed was 0.03. For this Po, simultaneous opening of two channels should be visible approx. every 140 events, which is over 35-fold fewer events than our chosen minimum. The data were idealized with an SKM algorithm, digitally low-pass filtering at 12.5 kHz and applying 0.12 ms (3 samples) dead time. Analysis of idealized data was performed with the maximum interval likelihood (MIL) algorithm (Qin et al., 1997; Amico-Ruvio and Popescu, 2010). Po, mean open time (MOT) and mean closed time (MCT) values were averaged for each construct and compared with each other.

Homology Modeling

We have used the recently available crystal structures (PDB IDs—4tll, 4tlm and 4pe5; Karakas and Furukawa, 2014; Lee et al., 2014) as templates for homology modeling of an all-atom complete structure including the linker region using the MODELLER 9v14 suite of programs (Sali and Blundell, 1993). The crystal structures carry several sequence modifications, including deletions, substitutions and introduction of disulfide bridges in order to stabilize the interaction between amino-terminal domains as well as in the TMD region. The overall NMDAR crystal structure quite likely reflects liganded receptor with the channel in the closed state. The homologous sequences were aligned using MUSCLE and visually inspected within Unipro UGENE program. The residues missing in the template structures were modeled using the "automodel" function of MODELLER, including symmetry restraints for the Cα atoms of corresponding pairs of subunits.

Studied mutations (substitutions and deletions) within the linker region were introduced using the MODELLER package,

based on the WT homology model. The complete atomic models of GluN1/GluN2B receptor and its mutants were further used for large-scale molecular modeling of linkers.

Conformational Sampling

Conformational sampling and refinement of linker regions was performed using the "loopmodel" function of MODELLER without any symmetry restraints, allowing a different structure for each linker. The full conformational space of selected linkers is too complex to be efficiently sampled by a classical molecular dynamics simulation. We have thus employed a Monte Carlo-like procedure, randomizing and refining the linker structure based on the simplified atomistic force field of MODELLER, which is capable of reproducing the crystal orientation and native contacts of a randomized loop for known structures. The "loopmodel" function involving the "refine.fast" routine was used for this enhanced sampling. The whole linker sequence LVLDRPEERITGIND of GluN1 and MIQEEYVDQVSGLSD sequence of GluN2B was selected for the refinement. Further, the shorter patches LVLDRPEE and MIQEEYVD, close to the TMD, were also modeled separately. For each WT and mutated linker region, we have performed 1000 "loopmodel" runs with different random seed setting and the Discrete Optimized Protein Energy (DOPE) score for each model was calculated. The DOPE score is based on a statistical potential optimized for model assessment. The DOPE score is designed to select the best structures from a set of MODELLER prepared models. For the NMDAR structure containing two GluN1 and two GluN2B subunits, this produced 2000 models of each region.

Analysis of Conformations

The complex ensemble of structures for each linker variant was further analyzed in terms of Protein Blocks (PB; de Brevern et al., 2000) assigned using the PBxplore package (Barnoud et al., 2017). For easier PB "sequence" processing, three "letters" of the alphabet were redefined to contain only standard one letter AA codes (B → Q, J → S, O → R) allowing us to use common sequence analysis tools. For each model, we have assigned its conformational descriptors in terms of the PB structural alphabet. PB represents a more detailed extension of the commonly used helix/sheet/coil secondary structure classification while still allowing conversion of complex 3D structural data into a simple 1D sequence-like data. The 2000 PB "sequences" for each sampled linker region sequence were combined and their structural content plotted using the weblogo program version 3.3 employing a user-defined color palette. The results from a separate run producing 1000 models were qualitatively identical to the larger run, proving the extent of simulations as sufficient.

Visualization of Structures

Graphical representation and analysis of residues surrounding selected regions were performed using PyMOL version 1.8.3 and VMD version 1.8.7.

Statistical Analysis

All data are expressed as mean ± SEM. Statistical differences between two groups of data was evaluated using a *t*-test and $P < 0.050$ was taken as the limit of significance. Multiple comparisons were made using one-way analysis of variance (ANOVA) and a Dunnett's *post hoc* analysis was applied only when a significant ($P < 0.050$) effect was evident (SigmaStat v3.5).

RESULTS

Deletions in the M3-S2 Linkers Promote Ion Channel Opening

There is a causal relation between glutamate and glycine binding to the NMDAR and channel opening. Simple mechanistic view suggests that conformational changes in the LBD result in the movement of M3-S2 linkers followed by a centrifugal displacement of GluN1 and GluN2B M3 helices and channel opening. Kazi et al. (2014) have shown that extension in the distal part of the linker (close to the LBD) impaired agonist-dependent channel opening. Therefore, we hypothesized that, in an opposite way, we could control the initial steps of the NMDAR opening and mimic glutamate activation by shortening the GluN2B M3-S2 linkers and glycine activation by shortening the GluN1 M3-S2 linkers. To prove our hypothesis and elucidate the role of the M3-S2 linkers, we made a series of single AA deletions in the GluN1(L655–E662) and GluN2B(M654–D661) M3-S2 linker, in its initial segment located in the proximity of the ion channel vestibule. The relatively sparse structural data for linkers suggest a rather extended polypeptide chain without any loops that would compromise the effect of deletion on the length of linkers (see **Figures 1A,B** for the homology and orientation). The mutated receptors were screened electrophysiologically.

The experimental protocol consisted of recording responses to a change of the ECS containing 2 mM Mg^{2+} to the solution containing: (i) 10 μM 7-Chlorokynurenic acid (7CKA; a competitive glycine site inhibitor, Kemp et al., 1988) with no added Mg^{2+}, glutamate, or glycine (spontaneous activity; I_{7CKA}); (ii) 1 mM glutamate and 10 μM 7CKA with no added Mg^{2+} or glycine (glutamate-induced responses; I_{Glu}); (iii) 0.1 mM glycine with no added Mg^{2+} or glutamate (glycine-induced responses; I_{Gly}); and (iv) 1 mM glutamate and 0.1 mM glycine with no added Mg^{2+} (glutamate and glycine-induced responses; $I_{Gly+Glu}$). Spontaneous activity and activity induced by a single agonist is expressed normalized with respect to the responses induced by glutamate together with glycine. Thus, relative spontaneous current (RI_{Spont}) was defined as: $RI_{Spont} = I_{7CKA}/I_{Glu+Gly}$ (*Equation 1*); relative glutamate responses (RI_{Glu}) were defined as: $RI_{Glu} = I_{Glu}/I_{Glu+Gly} - RI_{Spont}$ (*Equation 2*); and relative glycine responses as: $RI_{Gly} = I_{Gly}/I_{Glu+Gly} - RI_{Spont}$ (*Equation 3*). As expected, in the WT GluN1/GluN2B receptors, spontaneous activity and the responses to only glutamate or only glycine were negligible when compared to those induced by 1 mM glutamate and 0.1 mM glycine

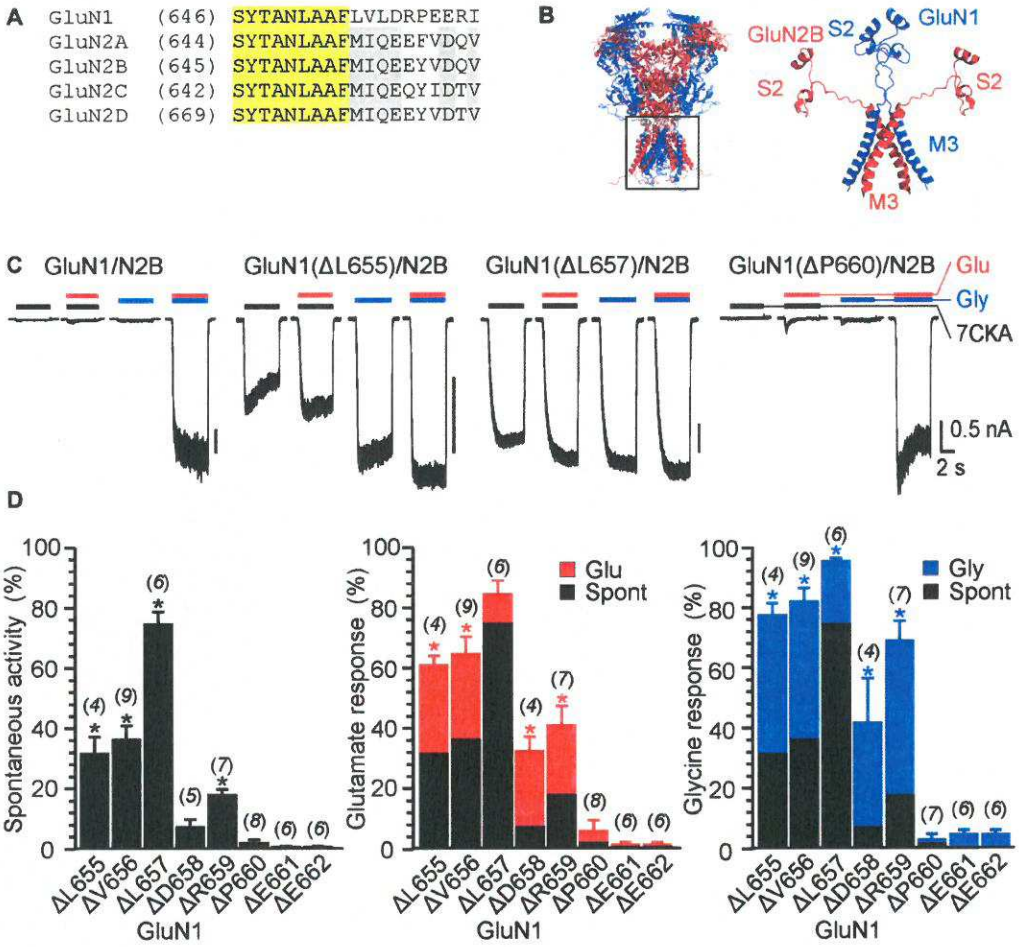

FIGURE 1 | The effect of single-deletion mutations of GluN1 linker on receptor activity. **(A)** Amino acids (AA) sequence alignment for the outer segment of the pore-forming region of the M3 and the initial segment of the M3-S2 linker. AA number is given in parentheses. Conserved motifs in N-methyl-D-aspartate (NMDA) receptor subunits are colored yellow (GluN1/GluN2) and gray (GluN2A-D). **(B)** Homology model of GluN1/GluN2B and the structure of the M3 and M3-S2 linkers are shown. GluN1 is colored in blue and GluN2B is colored in red. Note the different orientation of the M3-S2 linkers in GluN1 and GluN2B. **(C)** Representative current responses of GluN1/GluN2B wild-type (WT), GluN1(ΔL655)/GluN2B, GluN1(ΔL657)/GluN2B and GluN1(ΔP660)/GluN2B. Application of extracellular solution (ECS) containing 7-Chlorokynurenic acid (7CKA; 10 μM) with no added Mg^{2+}, glutamate, or glycine is indicated by a black bar (7CKA); application of 1 mM glutamate and 7CKA (10 μM) with no added Mg^{2+} or glycine is indicated by a red bar (Glu); application of 0.1 mM glycine with no added Mg^{2+} or glutamate is indicated by a blue bar (Gly). In between the applications of Mg^{2+}-free ECS, the cells were bathed in ECS containing 2 mM Mg^{2+}. **(D)** Summary graphs of the mean ± SEM (*n*) of the relative responses—RI_{Spont} (black columns), RI_{Glu} (red columns) and RI_{Gly} (blue columns; see Equations 1–3)—in receptors with a single residue deleted in GluN1. Differences in the relative responses determined for WT and mutated receptors were statistically significant; one-way ANOVA ($P < 0.001$); followed by multiple comparisons of the relative responses of mutated receptors vs. WT (RI_{Spont} 0.44 ± 0.06 ($n = 24$); RI_{Glu} 0.63 ± 0.30 ($n = 24$); RI_{Gly} 1.1 ± 0.2 ($n = 24$)); Dunnett's test; *$P < 0.050$.

(RI_{Spont} = 0.44 ± 0.06%; n = 24; RI_{Gly} = 1.1 ± 0.2%; n = 24; RI_{Glu} = 0.63 ± 0.30%; n = 24; **Figure 1C**). It is quite likely that this minor activity reflects indirect effect of Mg^{2+} wash out on membrane properties, rather than NMDAR activity.

Figure 1C shows an example of activity recorded for WT, GluN1(ΔL655)/GluN2B, GluN1(ΔL657)/GluN2B receptors and GluN1(ΔP660)/GluN2B receptors. The responses of GluN1(ΔL657)/GluN2B were characterized by a high degree of spontaneous activity (RI_{Spont} = 75 ± 4%; n = 6) that was further increased by glycine (RI_{Gly} = 21 ± 4%; n = 6) or glutamate (RI_{Glu} = 10 ± 6%; n = 6). Deletions at the linker region distal to the M3 helix e.g., GluN1(ΔD658)/GluN2B exhibited less spontaneous activity, however both RI_{Glu} and RI_{Gly} were still present. Similarly, deletions at the M3-S2 linker of the GluN2B altered the channel gating. **Figure 2A** shows an example of the activity recorded for GluN1/GluN2B(ΔM654), GluN1/GluN2B(ΔI655) and GluN1/GluN2B(ΔY659) receptors. For GluN1/GluN2B(ΔI655) the RI_{Spont} (17 ± 1%; n = 4) was relatively small compared to RI_{Gly} (61 ± 4%; n = 4), and RI_{Glu} (32 ± 7%; n = 4). Similarly to GluN1, deletions at the linker region

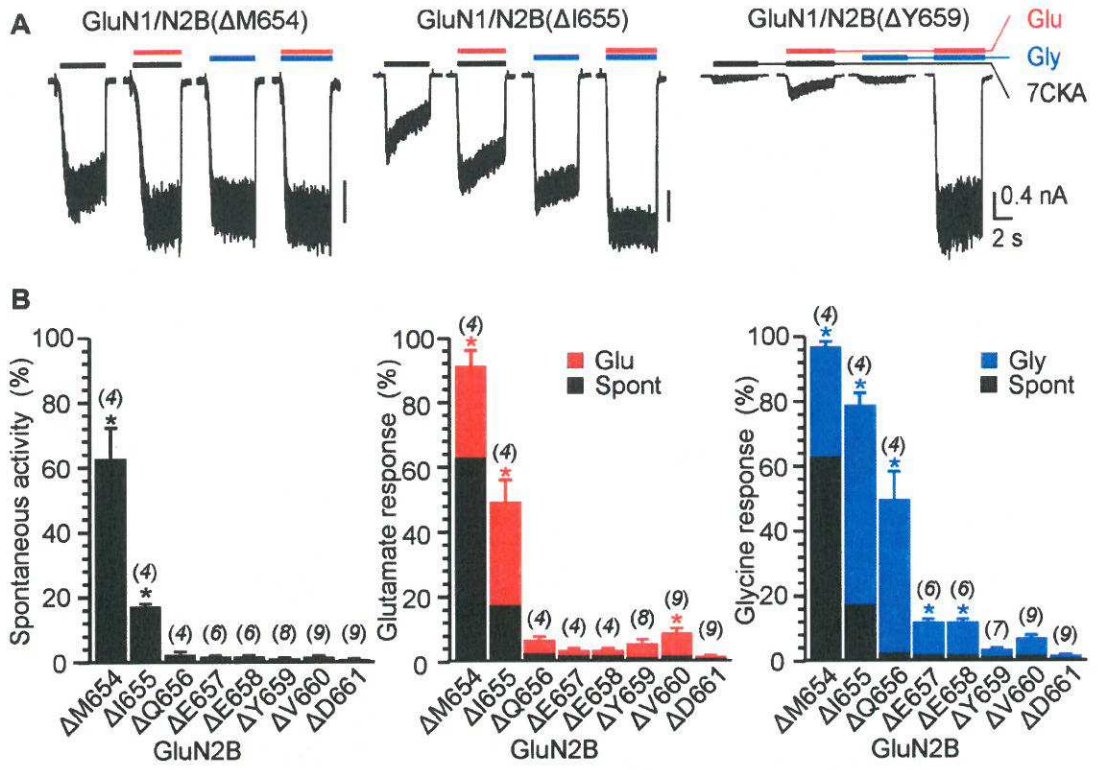

FIGURE 2 | The effect of single-deletion mutations of GluN2B linker on receptor activity. **(A)** Representative current responses of GluN1/GluN2B(ΔM654), GluN1/GluN2B(ΔI655) and GluN1/GluN2B(ΔY659). Application of ECS containing 7CKA (10 μM) with no added Mg^{2+}, glutamate, or glycine is indicated by a black bar (7CKA); application of 1 mM glutamate and 7CKA (10 μM) with no added Mg^{2+} or glycine is indicated by a red bar (Glu); application of 0.1 mM glycine with no added Mg^{2+} or glutamate is indicated by a blue bar (Gly). In between the applications of Mg^{2+}-free ECS, the cells were bathed in ECS containing 2 mM Mg^{2+}. **(B)** Summary graphs of the mean ± SEM (*n*) of the relative responses—RI_{Spont} (black columns), RI_{Glu} (red columns) and RI_{Gly} (blue columns; see Equations 1–3)—in receptors with a single residue deleted in GluN2B. Differences in the relative responses determined for WT and mutated receptors were statistically significant; one-way ANOVA ($P < 0.001$); followed by multiple comparisons of the relative responses of mutated receptors vs. WT (RI_{Spont} 0.44 ± 0.06 ($n = 24$); RI_{Glu} 0.63 ± 0.30 ($n = 24$); RI_{Gly} 1.1 ± 0.2 ($n = 24$)); Dunnett's test; *$P < 0.050$.

distal to the M3 helix e.g., GluN1/GluN2B(ΔY659) exhibited minimal spontaneous activity as well as RI_{Glu} and RI_{Gly}.

Similarly to single deletions, the deletion of two adjacent AAs altered the receptor channel activity. In the case of GluN1(ΔL655; ΔV656)/GluN2B and GluN1(ΔL657; ΔD658)/GluN2B RI_{Spont} was high (85% and 83%, respectively) and RI_{Gly} and RI_{Glu} had only a minor effect (Supplementary Figure S1A). As the double deletions were introduced to the more distal part of the linker—e.g., GluN1(ΔE661; ΔE662)/GluN2B the spontaneous activity was diminished, however, RI_{Gly} and RI_{Glu} were still present 28 ± 0.2% ($n = 3$) and 19 ± 2% ($n = 3$), respectively. Similarly to GluN1, double deletions introduced to the GluN2B affected NMDAR channel gating, but in contrast to GluN1 RI_{Spont} was lower (1%–12%; Supplementary Figure S1B).

Deletions in the M3-S2 linker of GluN1 and GluN2B subunits profoundly affect NMDAR channel function and the results summarized in **Figures 1D**, **2B** allowed us to draw the following conclusions: (i) NMDARs with mutated linkers open spontaneously and as a consequence of receptor activation by a single agonist; (ii) the effect of deletions is stratified—spontaneous activity and single ligand-induced responses are more pronounced for deletions closer to the M3 helix; (iii) the degree of spontaneous activity and single-agonist responses, as well as the length of the linker region affected by deletions, differ for GluN1 and GluN2B subunits; (iv) irrespective of whether deletions have been introduced in GluN1 or GluN2B subunits, application of glutamate or glycine promoted receptor channel activity; (v) irrespective of whether deletions have been introduced to the M3-S2 linker of GluN1 or GluN2B, responses induced by glycine were (on average) larger than those induced by glutamate (**Figures 3A,B**); and (vi) none of the single and double deletions in the linker region mimicked maximal receptor activation (100%) by a single agonist (insensitive to glutamate and sensitive to glycine and vice versa insensitive to glycine and sensitive to glutamate).

To avoid activity induced by residual glycine (typical contamination of high-quality water and chemicals is in the

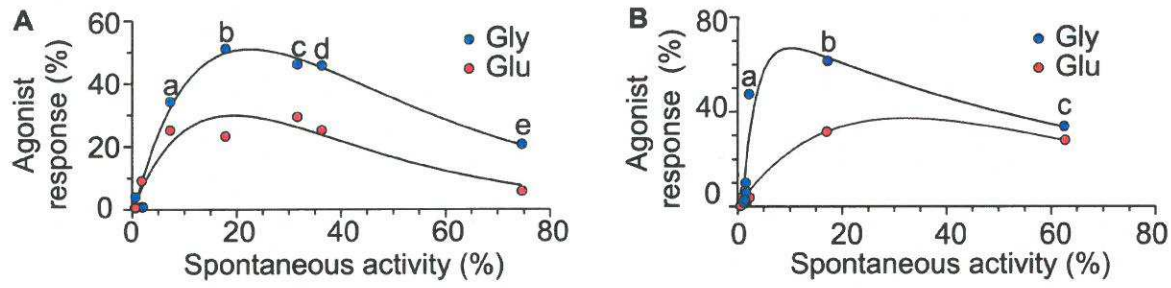

FIGURE 3 | The relation between spontaneous activity and single agonist-induced responses. **(A)** Plot of the RI_{Spont} activity vs. RI_{Glu} (red symbols) and RI_{Gly} (blue symbols) in receptors with single-deletion mutations in GluN1 linker (*a* = ΔD658; *b* = ΔR659; *c* = ΔL655; *d* = ΔV656; *e* = ΔL657). **(B)** Plot of the RI_{Spont} activity vs. RI_{Glu} (red symbols) and RI_{Gly} (blue symbols) in receptors with single AA deletion mutations in GluN2B linker (*a* = ΔQ656; *b* = ΔI655; *c* = ΔM654).

concentration range of tens of nM, which is potentially not negligible considering that the glycine EC50 is nM for WT GluN1/GluN2B receptors, Chen et al., 2008), 7CKA was used as a competitive glycine site inhibitor (Kemp et al., 1988) in the above experiments. To exclude the possibility that 7CKA can on its own affect RI_{Spont} and RI_{Glu}, we performed control experiments in which the activity was compared in solutions prepared in a way to maximally avoid glycine contamination and that containing 10 μM 7CKA. The values of RI_{Spont} recorded in the presence of 7CKA and in its absence were correlated (r = 0.997; $P < 0.01$) with a slope of 1.14 ± 0.02 (Supplementary Figure S2). Similarly, the values of RI_{Glu} recorded in the presence of 7CKA and in its absence were correlated (r = 0.604; P = 0.013) with a slope of 1.71 ± 0.30 (Supplementary Figure S2). These results indicated that 7CKA and/or background glycine only had a minor effect on gating of mutated NMDARs.

Computational Analysis of Mutation-Induced Structural Changes in the M3-S2 Linker

To elucidate the molecular basis for the role of the M3-S2 linker in coupling the LBD to the ion channel, we employed computational methods. The presented model of the NMDAR is based on crystal structures of the heterotetrameric GluN1/GluN2B receptor (Karakas and Furukawa, 2014; Lee et al., 2014). Missing experimental electron density in the available crystal structures does not allow localization of residues in the linker regions and the related structural information is mostly missing; we, therefore, decided to explore linker structures computationally. The structural information for the linker regions, missing in the crystal structures, is a consequence of local disorder. This could be interpreted either by intrinsically disordered linkers not adopting any structure, or by a set of overlapping local structures and their transitions.

Conformational descriptors in terms of PB were used to reveal intrinsic structural preferences in the linker region (see Supplementary Figure S3A). PB are structural prototypes defined by de Brevern et al. (2000). Complex three-dimensional structural information of a protein backbone can be encoded as a one-dimensional sequence of PB "letters". The PB cover all possible protein conformations and an automated procedure assigns each amino acid residue in a protein structure into one of the sixteen available PB. This procedure represents a significant extension of the commonly used secondary structure helix/sheet/coil descriptors, allowing fine analysis of protein flexibility (Craveur et al., 2015).

The results summarized as a PB structural alphabet logo indicate that only the first three residues in each linker (GluN1 LVL and GluN2B MIQ) have the potential to carry a high content of secondary structure (Supplementary Figure S3B). The consensus shows that these three residues cover the whole transition from helical to extended conformation, with the first residue visiting mostly helical or "end of helix" conformations, while the structure of remaining residues is already dominated by extended conformations. In general, the GluN1 linker structure is more disordered, while the structure of the GluN2B linker shows a higher content of extended conformations in the linker region. One potential problem with single AA deletions in the M3-S2 linker is that each may in principle induce multiple changes in the secondary structure that are difficult to predict. But the comparison of the M3-S2 linker between the WT and single AA deleted models revealed that single AA deletions in the GluN1(L655 to E662) as well as in the GluN2B(M654 to D661) had only a minor effect on the linker secondary structure. In theory, for a fully extended conformation, a single AA deletion induces shortening of the protein by ~3.4 Å; however, the extended conformation content is relatively low after averaging all the data, indicating that even the GluN2B linker is rather flexible and not stretched to its maximum length. Although the PB sequence logo is dominated by letters corresponding to extended conformations, the extended conformation is found only locally, not spanning over a longer patch of residues within the same model. There is also no evidence of shortening the M3-S2 distance by forming a patch of a more compact secondary structure element (like α-helix). Further, the effect of the deletion remains mostly local, compensated by conformation change of the nearest

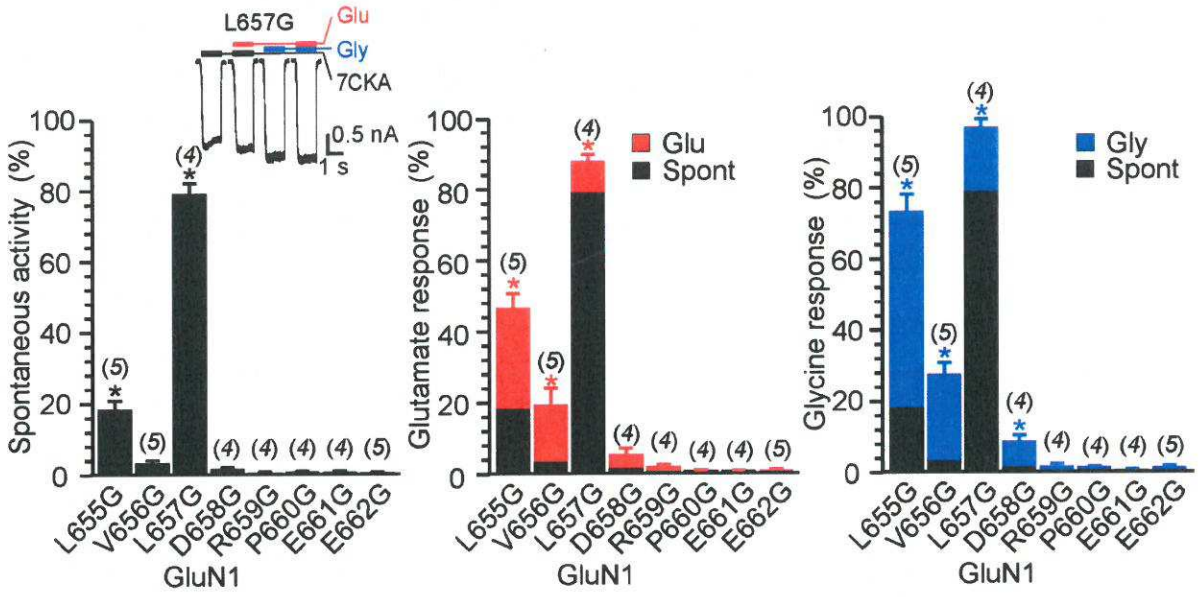

FIGURE 4 | The effect of glycine mutagenesis of the GluN1 M3-S2 linker. Summary graphs of the mean ± SEM (*n*) of the relative responses—RI_{Spont} (black columns), RI_{Glu} (red columns) and RI_{Gly} (blue columns; see Equation 1–3)—in receptors with a single residue mutated to glycine in the GluN1 linker. Inset, representative current response of GluN1(L657G)/GluN2B. Application of ECS containing 7CKA (10 μM) with no added Mg^{2+}, glutamate, or glycine is indicated by a black bar (7CKA); application of 1 mM glutamate and 7CKA (10 μM) with no added Mg^{2+} or glycine is indicated by a red bar (Glu); application of 0.1 mM glycine with no added Mg^{2+} or glutamate is indicated by a blue bar (Gly). In between the applications of Mg^{2+}-free ECS the cells were bathed in ECS containing 2 mM Mg^{2+}. Differences in the relative responses determined for WT and mutated receptors were statistically significant; one-way ANOVA ($P < 0.001$); followed by multiple comparisons of the relative responses of mutated receptors vs. WT (RI_{Spont} 0.44 ± 0.06 ($n = 24$); RI_{Glu} 0.63 ± 0.30 ($n = 24$); RI_{Gly} 1.1 ± 0.2 ($n = 24$)); Dunnett's test; *$P < 0.050$.

neighboring residues and does not propagate to the more distant regions.

Effect of Substitutions in the M3-S2 Linkers of the GluN1 and GluN2B on Channel Gating

To further strengthen the hypothesis that altered NMDAR gating caused by AA deletions in the linker region is primarily due to the disruption of specific interactions at the linker-to-channel transition we decided to analyze the effect of glycine substitution of single AAs in the linker region. To rule out the effect of shortening we employed computational methods to analyze conformations of linkers with one AA substituted by glycine. Comparison of the M3-S2 linkers between WT and single-substituted models (Supplementary Figure S3C) revealed that single residue substituted by glycine in the GluN1(L655–E662) as well as in the GluN2B(M654–D661) had only a minor effect on the linker secondary structure and therefore it is unlikely that the linker length was considerably altered.

Next, we prepared a series of single glycine substitution mutations in the GluN1(L655–E662) and GluN2B(M654–D661) linker regions and analyzed functional consequences for the NMDAR channel gating. Insets in **Figures 4**, **5** show an example of activity recorded in GluN1(L657G)/GluN2B and GluN1/GluN2B(I655G). While in GluN1(L657G)/GluN2B receptors RI_{Spont} was high and glutamate or glycine increased the current only a little, in GluN1/GluN2B(I655G) receptors RI_{Spont} was low and glutamate or glycine increased the current substantially. Other glycine substitution mutations in the linker region more distal to the M3 helix—GluN1(D658G to E662G) and GluN2B(E658G to D661G)–exhibited only minor spontaneous or single agonist-induced activity (**Figures 4**, **5**). Functional consequences of glycine mutagenesis are similar to those of deletions, indicating on the importance of specific linker-linker interactions rather than simply altered linker length.

Single-Channel Analysis of M3-S2 Linker Mutated Receptors

The data in **Figures 1–5** express the degree of impairment of mutated receptors in terms of a relative number reflecting receptor activation by glutamate and glycine co-application. It has been shown earlier that at saturating concentrations of glutamate and glycine GluN1/GluN2B WT receptors open with a low probability ~10% (Chen et al., 1999). Next, the single-channel analysis was used to assess the Po of mutated GluN1/GluN2B receptors as a measure of impairment of the NMDAR channel gating. For each receptor type, we obtained long-duration recordings ($\geq 10^5$ events) of steady-state currents from cell-attached membrane patches containing only one active channel (**Figure 6**). Inward sodium currents were obtained in the presence of saturating concentrations

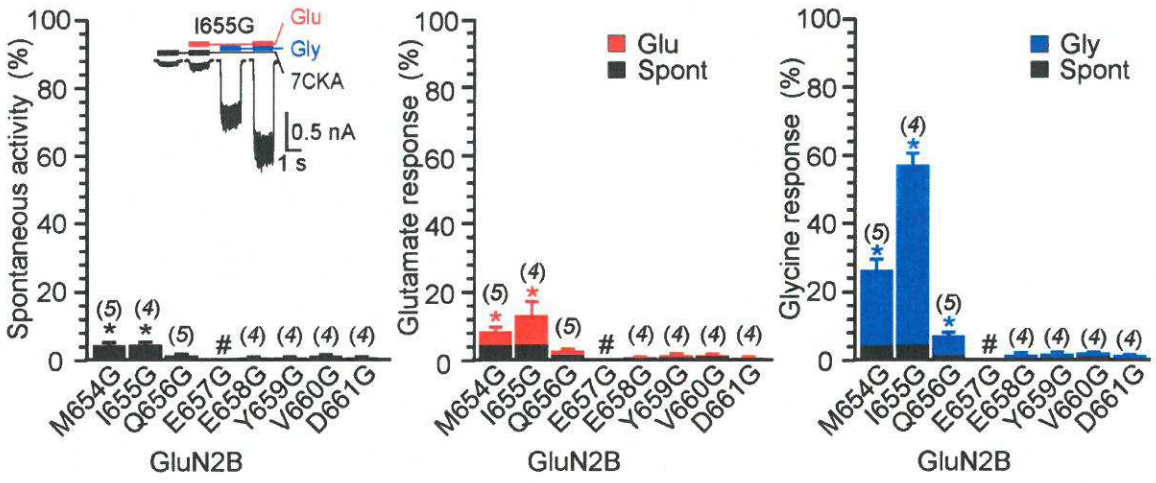

FIGURE 5 | The effect of glycine mutagenesis of the GluN2B M3-S2 linker. Summary graphs of the mean ± SEM (*n*) of the relative responses–RI_{Spont} (black columns), RI_{Glu} (red columns) and RI_{Gly} (blue columns; see Equation 1–3)–in receptors with a single residue mutated to glycine in the GluN2B linker. Inset, representative current responses of GluN1/GluN2B(I655G). Application of ECS containing 7CKA (10 μM) with no added Mg^{2+}, glutamate, or glycine is indicated by a black bar (7CKA); application of 1 mM glutamate and 7CKA (10 μM) with no added Mg^{2+} or glycine is indicated by a red bar (Glu); application of 0.1 mM glycine with no added Mg^{2+} or glutamate is indicated by a blue bar (Gly). In between the applications of Mg^{2+}-free ECS the cells were bathed in ECS containing 2 mM Mg^{2+}. Differences in the relative responses determined for WT and mutated receptors were statistically significant; one-way ANOVA ($P < 0.001$); followed by multiple comparisons of the relative responses of mutated receptors vs. WT (RI_{Spont} 0.44 ± 0.06 ($n = 24$); RI_{Glu} 0.63 ± 0.30 ($n = 24$); RI_{Gly} 1.1 ± 0.2 ($n = 24$)); Dunnett's test; $^*P < 0.050$. $^\#$Indicates a nonresponding mutation.

of agonists (1 mM glutamate and 0.1 mM glycine) under conditions that minimized inhibitory effects of contaminating divalent ions (1 mM EDTA) at a holding potential +100 mV (estimated membrane potential ~ −130 mV). The records contained unitary currents of uniform amplitudes, with no obvious superimposed openings; typical currents occurred as bursts of frequent openings separated by long silent periods. First, we analyzed single-channel records to estimate Po, MOT and MCT, as global measures of gating kinetics for WT and mutated receptors (GluN1(ΔL657)/GluN2B and GluN1(ΔP660)/GluN2B). For comparison, we have also introduced a glycine mutation at the position GluN1(L657) to preserve the number of AAs within the linker, however with a minimal effect on the space occupied by L657 in the WT NMDAR. By these metrics, GluN1(L657G)/GluN2B and GluN1(ΔL657)/GluN2B receptors had, respectively, a 7.5-fold and a 5.7-fold higher Po relative to the WT receptor. For either mutated receptor, the higher activity was due to shorter closures (MCT 11- and 4.1-fold, respectively) and longer openings (MOT 12- and 4.3-fold, respectively; **Figures 6A–C** and **Table 1**). As expected, the receptors with deletions in the linker region distal to the M3 helix e.g., GluN1(ΔP660)/GluN2B exhibited Po values more comparable with WT receptor (**Figure 6D** and **Table 1**).

LILI Motif and NMDAR Gating

Our results suggest that along the way to the ion channel opening, the M3-S2 linker transduces the signal from the LBD leading to the pore opening, however, not exclusively only by simple mechanical coupling. We hypothesize that the overall effect of the deletions and substitutions on the NMDAR gating we describe can be explained by an interaction of two pairs of specific M3-S2 linker residues at a site located in the proximity of the M3 helices (LILI motif) rather than a simple shortening of the linker. These interactions may form the basis for a novel extracellular NMDAR site controlling the process of gating. Mutations in either the GluN1 or the GluN2B M3-S2 linkers disrupt the receptor gating. Therefore, the NMDAR channel can open spontaneously and be activated to a similar extent by glutamate (in the absence of glycine) and by glycine (in the absence of glutamate).

Measurements of spontaneous activity and single-agonist-induced responses in both the single-AA-deleted and glycine-substituted M3-S2 linker mutants agree on the importance of the GluN1 LVL as well as the GluN2B MIQ residues and indicate that the extracellular gating motif is located at this site close to the M3 helices. To understand the detailed structural organization of the NMDAR channel at its M3-to-linker transition we have further extracted and analyzed a set of lowest energy conformations (according to their DOPE score from MODELLER) for LVLDRPEE and MIQEEYVD linker residues from the above-mentioned NMDAR models. Within the LVL and MIQ regions, we have identified a specific role of the GluN1(L657) in the NMDAR channel gating. This explains the experimentally observed spontaneous activity after the deletion of this residue. On the other hand, the GluN2B(I655) serves as a potential binding partner to the gating GluN1(L657) (**Figure 7**). Further, comparing the structural propensities of the GluN1 and the GluN2B linkers close to the transmembrane helices, we can speculate that mutations in the already more

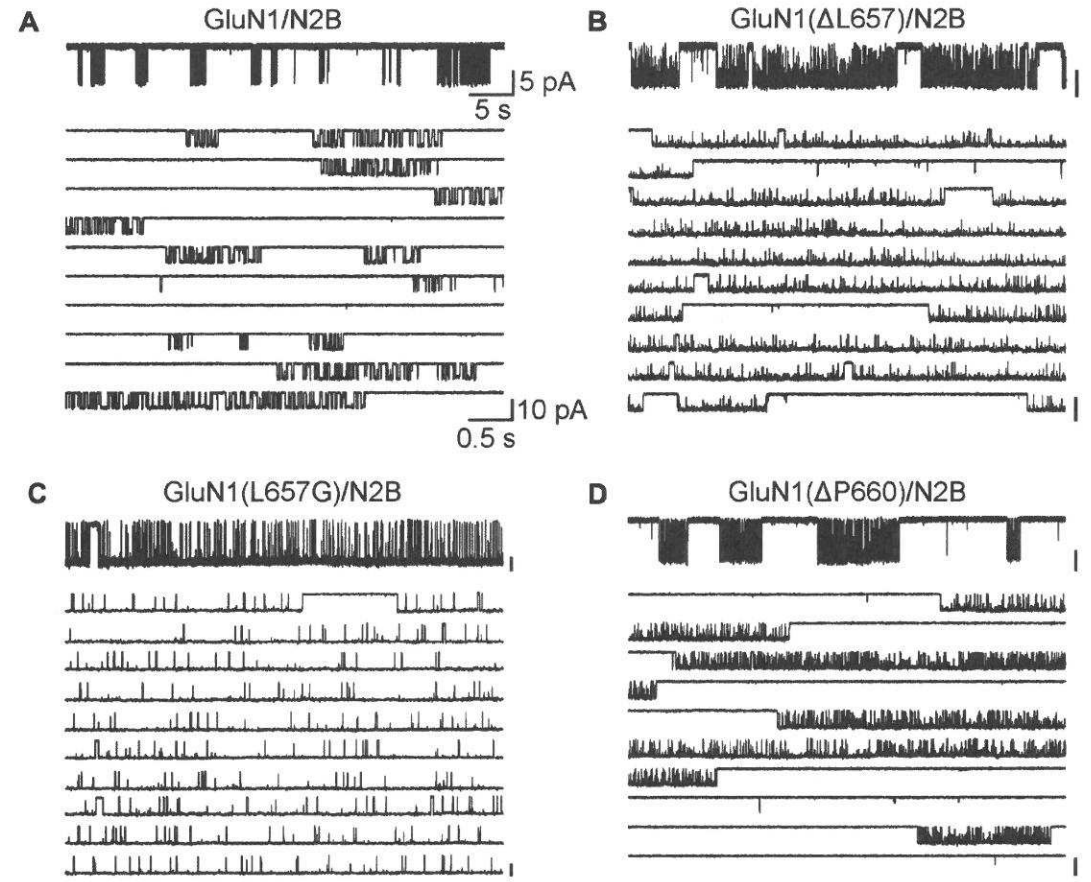

FIGURE 6 | The GluN1(ΔL657) and GluN1(L657G) mutations alter single-channel properties. **(A–D)** Portions of steady-state cell-attached patch records, each containing only one active channel filtered at 1 kHz (for the purpose of the presentation only) from HEK293 cells expressing WT receptors **(A)**, GluN1(ΔL657)/GluN2B **(B)**, GluN1(L657G)/GluN2B **(C)**, or GluN1(ΔP660)/GluN2B **(D)** receptors. Each record is expanded below to 10 traces (1 kHz). Unitary currents were activated in these patches by 1 mM glutamate and 0.1 mM glycine.

flexible GluN1 induce an easier loss of helical structure and a higher solvent accessibility of the channel mouth and can lead to spontaneous activity.

Based on the residues involved in the extracellular gate we will use the "LILI" shortcut to address this motif throughout the text. The LILI motif in the gating conformation was identified within the most stable NMDAR models (**Figure 7A**, Supplementary Figure S4). An important structural feature of the LILI motif is that the two GluN1 leucine residues are not arranged symmetrically but rather stacked over each other, while both interacting with the GluN2B isoleucine residues (**Figures 7B,D,E**). This arrangement allows for tight van der Waals (vdW) interactions (alternatively called dispersion or hydrophobic) efficiently shielding the channel entrance from water (**Figure 7C**). It also offers an explanation for the opening mechanism involving the GluN1 linker with its unexpected orientation along the direction of the channel longitudinal axis. A naive model of the mechanism of opening a channel composed of four transmembrane helices would involve simultaneous pulling of all four linkers in the direction parallel to the membrane plane (which is the case only for the GluN2 linker).

TABLE 1 | Summary of single-channel properties.

	Po	MCT (ms)	MOT (ms)	Amplitude (pA)	Total events (*n*)
GluN1/GluN2B	0.12 ± 0.02	49 ± 11	5.1 ± 0.5	8.0 ± 0.4	4.4×10^5 (6)
GluN1(ΔL657)/GluN2B	0.68 ± 0.09*	12 ± 4*	22 ± 5	6.3 ± 0.4	6.0×10^5 (5)
GluN1(ΔP660)/GluN2B	0.21 ± 0.05	20 ± 3*	4.8 ± 0.6	7.2 ± 0.4	4.0×10^5 (4)
GluN1(L657G)/GluN2B	0.90 ± 0.03*	4.6 ± 1.0*	63 ± 14*	7.2 ± 1.3	1.0×10^5 (6)

*The values represent the mean ± SEM (n) for each data set. *P < 0.05; one-way ANOVA, Dunnett's test.*

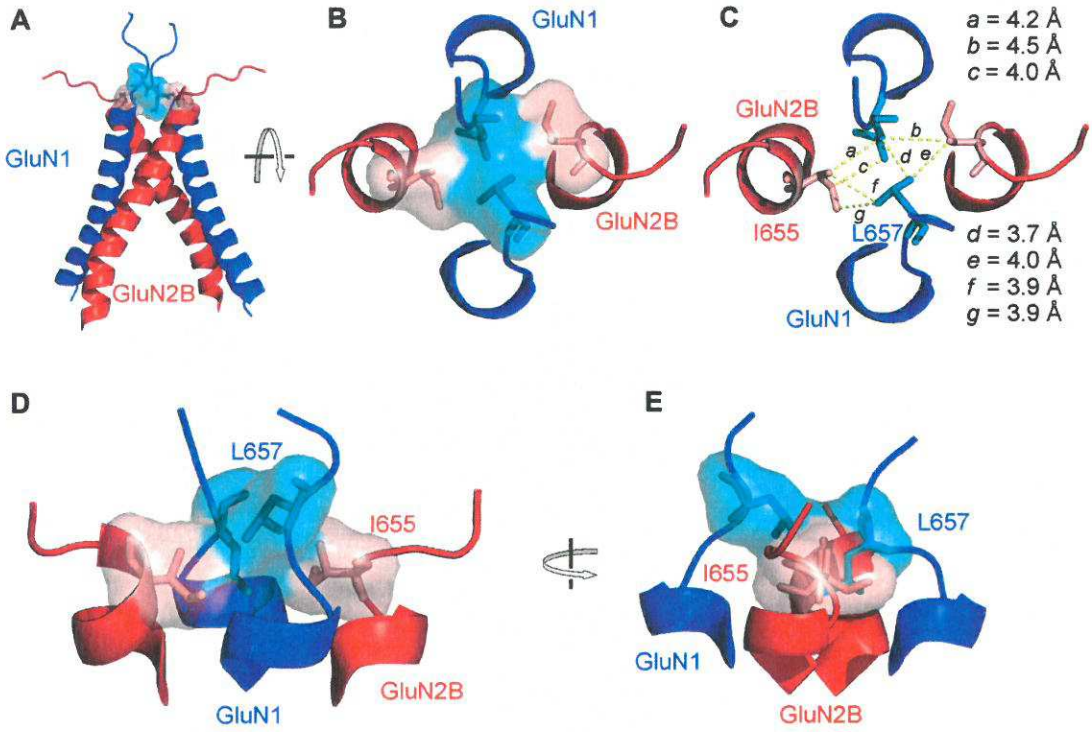

FIGURE 7 | The structural arrangement of the NMDAR channel gate. **(A)** Ribbon diagram showing the GluN1 (blue) and GluN2B (red) M3 helices with the initial portion of the M3-S2 linkers. Semitransparent molecular surface representation of GluN1 L657 and GluN2B I655 is indicated in light blue and light red, respectively. **(B)** The extracellular channel gate of the GluN1/GluN2B receptor is shown in a closed conformation and viewed from the extracellular side of the membrane. **(C)** The same view is shown with molecular distances between L657 and I655 residues indicated. **(D,E)** The structure of the gate viewed from the side with the GluN1 M3 helices in the front and in the back **(D)** and rotated by 90° along the longitudinal axis **(E)**.

The stability of the LILI motif can be attributed to a tight vdW interaction of the nonpolar leucine and isoleucine residues. To further strengthen this hypothesis, we used the NMDAR model to test the structural to functional consequences of the GluN1(L657) substitution for glycine, alanine, valine, phenylalanine and glutamine (**Figure 8** and Supplementary Figure S5). The selection includes nonpolar amino acids with increasing size and hydrophobicity of the side chain as well as a polar glutamine of a size similar to the substituted leucine. The results of the simulation indicate that when GluN1(L657) was substituted by a small AA glycine, the vdW interaction that existed in the LILI motif was substantially weakened and the introduced GIGI motif became unstable with the expected loss of gating ability (**Figure 8B**, L657G). This is in agreement with the experimentally observed high degree of spontaneous activity (**Figures 4**, **8A**, Supplementary Figure S5A, L657G). The substitution of GluN1(L657) for alanine and valine allowed partial restoration of the vdW interaction between the residues. However, the interaction with the GluN2B(I655) led to the partial unfolding of the GluN1 M3 helix (**Figure 8B**, L657A, L657V). The modeling of the L657F substitution revealed a favorable interaction of the larger phenylalanine residue with GluN2B(I655), although the other phenylalanine residue was not in direct interaction due to steric constraints (**Figure 8B**, L657F). Mutations in this series of hydrophobic amino acids markedly reduced spontaneous activity when compared to that observed for the GluN1(L657) substitution by glycine (**Figure 8A** and Supplementary Figure S5A). The activity induced by glutamate or by glycine decreased in a similar order as spontaneous activity (L657A > L657V > L657F, **Figure 8A**, Supplementary Figure S5A) and this agrees well with the computational prediction. In the case of the GluN1(L657) substitution for glutamine, vdW interaction is expected to be negligible and as a consequence, the polar glutamine was expelled and oriented towards the water environment (Supplementary Figure S5B, L657Q). The functional examination showed an increase of spontaneous and single-agonist-evoked activity of the glutamine mutated NMDAR (Supplementary Figure S5A, L657Q).

In addition, the role of the LILI motif in NMDAR gating is supported by experiments in which leucine and isoleucine were substituted by cysteine. Reducing agent dithiothreitol (DTT) potentiated WT receptors by 93 ± 7% (n = 6) while GluN1(L657C)/GluN2B(I655C) receptor responses were potentiated significantly more, by 739 ± 84% (n = 4; t-test $P < 0.001$). The effect of DTT was reversible upon application of oxidizing agent 5,5′-dithiobis(2-nitrobenzoic acid) (DTNB; see Supplementary Figure S6).

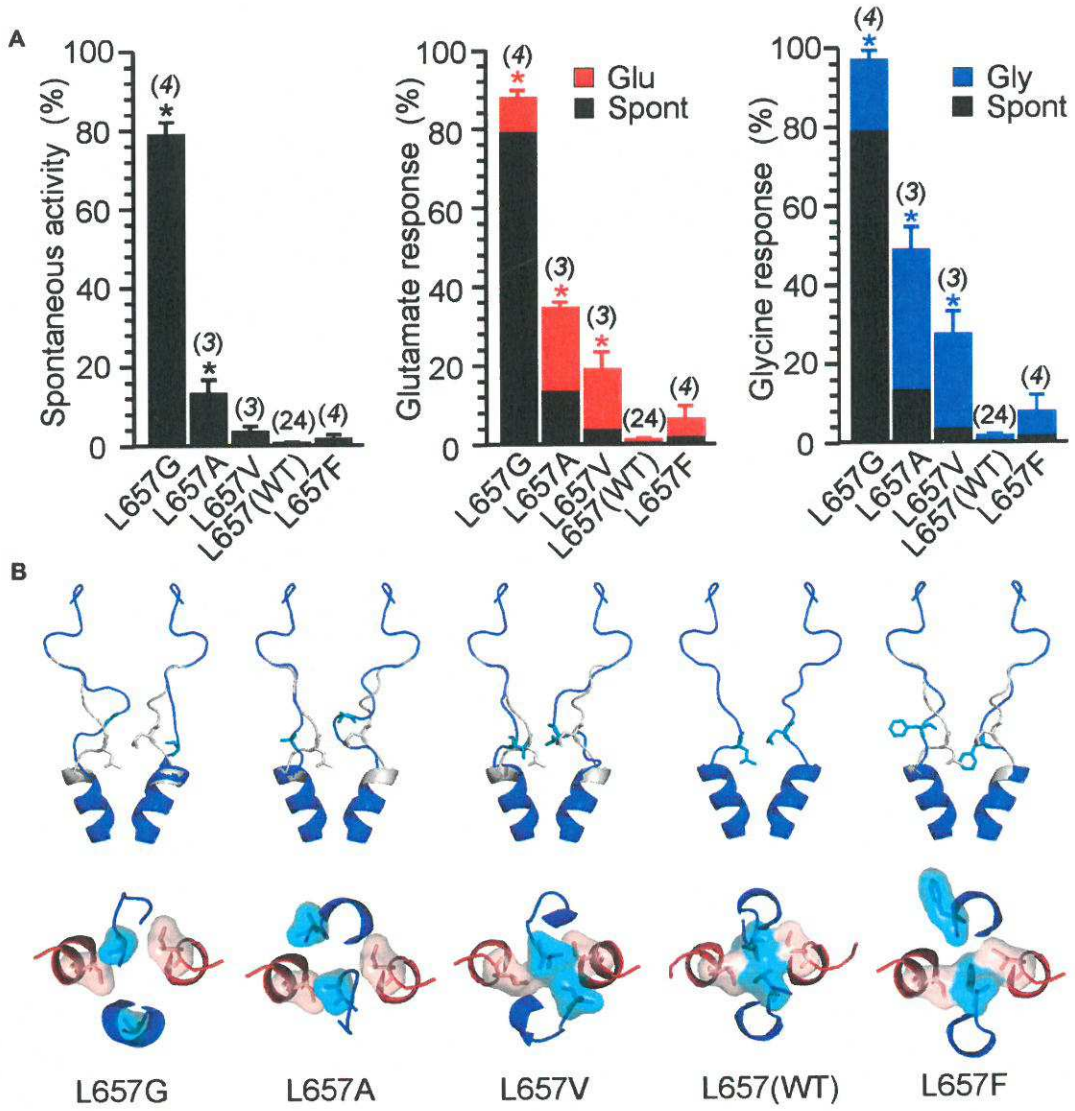

FIGURE 8 | Consequences of GluN1(L657) mutations. **(A)** Summary graphs of the mean ± SEM (*n*) of the relative responses—RI_{Spont} (black columns), RI_{Glu} (red columns) and RI_{Gly} (blue columns; see Equations 1–3)—in receptors with a single residue GluN1(L657) mutated to glycine (G), alanine (A), valine (V), phenylalanine (F) and glutamine (Q). Differences in the relative responses determined for WT and mutated receptors were statistically significant; one-way ANOVA ($P < 0.001$); followed by multiple comparisons of the relative responses of mutated receptors vs. WT (RI_{Spont} 0.44 ± 0.06 ($n = 24$); RI_{Glu} 0.63 ± 0.30 ($n = 24$); RI_{Gly} 1.1 ± 0.2 ($n = 24$)); Dunnett's test; *$P < 0.050$. **(B)** Ribbon representation of GluN1 subunits (blue) and GluN2B subunits (red) at the extracellular channel vestibule viewed from the membrane and the extracellular side. The computational models show the most frequent (typical) position (structure) of GluN1(L657) in the WT (indicated in gray) and when mutated to glycine (G), alanine (A), valine (V), leucine—wild type (L) and phenylalanine (F; indicated in blue).

DISCUSSION

Our results indicate that an extracellular LILI motif which is formed by the M3-S2 linkers (at the transition between the M3 helices and the linkers) is an important element that connects conformational changes at the level of the LBD induced by agonist binding and unbinding to the NMDAR channel opening and closing. We propose that the LBD pulling energy displaces GluN1 and GluN2 M3-S2 linkers which leads to disassembly of the compact form of the LILI motif which then serves as the first step in conformational transitions leading to the M3 helix separation, displacement, and finally to channel opening. In addition to classic NMDAR ion channel action, unconventional NMDAR signaling has been described recently including metabotropic NMDAR signaling (Nabavi et al., 2013; Dore et al., 2016, 2017; Bouvier et al., 2018). Since some form of NMDAR dependent long-term depression can be induced without Ca^{2+} influx, we suppose that altered ion channel gating

would have a minor effect on the metabotropic action of NMDAR (to confirm this conclusion is beyond the scope of this work).

NMDAR channel opening occurs as a consequence of glycine binding to the GluN1 subunit and glutamate binding to the GluN2 subunit (Kuryatov et al., 1994; Laube et al., 1997). The results of our experiments in which the linker length was shortened or structure altered indicate that the GluN1 and the GluN2B M3-S2 linkers contribute unequally to channel opening and are consistent with previously published data in which the linker length was prolonged (Kazi et al., 2014) and when residues were substituted by alanine (Chang and Kuo, 2008). However, the exact relationship between the degree of individual linker displacement and the degree of channel opening remains to be resolved. Indeed, our data indicate that the deletion of a single AA at the linker site outside the gate already has a profound effect on channel gating (**Figures 1, 2**). The exact prediction of the possible linker shortening induced by a single AA deletion strongly depends on local linker structure, however, the upper limit for a fully extended structure of one AA is about 3.4 Å and a common shortening obtained from the analysis of our models is on the order of 1.5 Å. Our recently published data indicate that the extracellular NMDAR channel vestibule has to open widely (the diagonal C_α to C_α distance of 37 × 38 Å at the level of GluN1(D658) and GluN2B(E657)) to open the ion channel at the site of the TTTT ring (GluN1 T648 and GluN2B T647) to the minimum cross-section of the channel permeation pathway in the conducting states (Vyklicky et al., 1988, 2015). A similarly widely opened channel vestibule was proposed for the NMDAR just prior to channel opening (Dai and Zhou, 2013). This makes it likely that the degree of linker displacement and the degree of the channel opening at the vestibule are not directly linked. This is further supported by crystallographic data indicating that the movement evoked at the level of the S2 lobe by agonist binding (Furukawa et al., 2005; Karakas and Furukawa, 2014; Lee et al., 2014), which is expected to be responsible for the linker pull, is relatively small.

The LILI motif represents a common hub for the mechanical pulling by the GluN1 and the GluN2 M3-S2 linkers. The nature of these forces is precisely balanced such that only joint mechanical pulling from both pairs of linkers allows the compact form of the LILI motif to disassemble and subsequently to initiate channel opening. On the structural level, the gate must be fine-tuned and even small changes (**Figure 8B**) have a profound effect on channel gating. Previous crystallographic and functional studies suggested an additional site located within the highly conserved SYTANLAAF motif of the M3 helix of both the GluN1 and the GluN2 subunits (Kashiwagi et al., 2002; Sobolevsky et al., 2007, 2009; Chang and Kuo, 2008; Vyklicky et al., 2015). This region contains the narrowest portion of the ion channel—the TTTT ring, the group of four threonines GluN1(T648) and GluN2B(T647) (Beck et al., 1999; Sobolevsky et al., 2002). Surprisingly, NMDARs with threonines mutated to alanines (GluN1(T648A) or GluN2B(T647A)) formed constitutively (spontaneously) open channels (Kashiwagi et al., 2002; Sobolevsky et al., 2007; Chang and Kuo, 2008; Vyklicky et al., 2015). This indirectly indicates the role of the TTTT ring in the stabilization of the closed conformation of the NMDAR channel. This is also in line with computational approaches indicating a compact geometry at the level of the TTTT ring that allows optimal distance to form vdW contacts as well as hydrogen bonds among the side chain atoms of the threonine residues (Vyklicky et al., 2015).

We have employed computational methods (molecular modeling features of MODELLER package, including the conjugate gradient optimization and molecular dynamics) to reveal the individual molecular steps in the process of NMDAR channel opening. The available crystal structures of the heterotetrameric GluN1/GluN2B receptor were solved with agonists bound (Furukawa et al., 2005; Karakas and Furukawa, 2014; Lee et al., 2014) and therefore it is likely that they represent a transitory state of the channel just prior to its opening—an activated closed state. Although we cannot completely exclude the speculation that the crystal structure could also represent a desensitized state, our observation of the asymmetric behavior of NMDAR models at the channel entrance might suggest that the crystal structure represents an average of the oscillating movements of the M3 helices. At the level of the LILI motif, this state is characterized by vdW interactions between diagonally located leucines (L657) of the GluN1 subunits and adjacent isoleucines (I655) of the GluN2B subunits (**Figures 9A,B**).

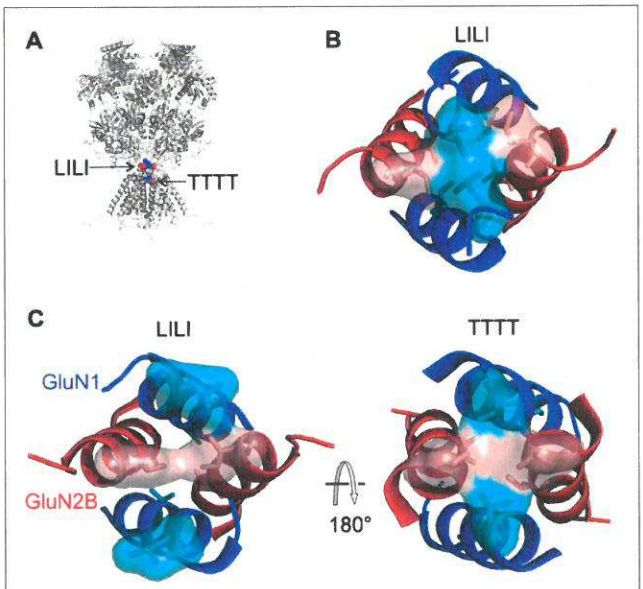

FIGURE 9 | Model of the NMDAR channel opening. **(A)** The location of LILI and TTTT gates is shown. **(B)** The LILI gate in the activated closed state serves as a "plug" shielding the channel entrance from the water. During the opening, the upward pulling of the GluN1 M3-S2 linker resulting from glycine binding and the sideward pulling of the GluN2 M3-S2 linker resulting from glutamate binding, as induced by the ligand-binding domain (LBD) conformational change, leads to the breaking of the tight hydrophobic LILI-gate, exposing the channel entrance to water. **(C)** An intermediate state involving the formation of the second gate, the TTTT ring. However, once water reaches the TTTT ring, it competes with the hydrogen bonding and the vdW contacts among the threonines and as a consequence the M3 helices separate, leading to the open NMDAR channel.

The opening of the channel was modeled similarly to our previous work (Vyklicky et al., 2015) by stepwise elongation of the distance between pairs of GluN1 and GluN2B domains anchored by the Cα atoms of the topmost residues within the pore-forming helices. As discussed previously, the TTTT ring (**Figure 9A**) does not form a tight interaction in the available crystal structures and this interaction is formed only during the process of NMDAR opening. A more detailed picture of the NMDAR opening process involves the currently proposed LILI motif. For the modeling, the initial, crystal-derived geometry of the transmembrane helices was identical to the previous work and the currently used model differed only in the newly identified geometry of the linkers. The modeling connected the starting LILI model with the previously described TTTT ring intermediate and the fully opened NMDAR channel.

Based on the modeling we predict that the upward pulling of the GluN1 M3-S2 linker resulting from glycine binding and the sideward pulling of the GluN2 M3-S2 linker (see **Figure 1B** for linker orientation) resulting from glutamate binding leads to the breaking of the tight hydrophobic interaction in the LILI motif that serves as a "plug" thus exposing the channel entrance to water (**Figure 9C**, *left*). The breaking of the interaction in the LILI motif results from a combination of the separation of the outer segments of the M3 helices and the rotation of these helices induced by pulling the M3-S2 linkers. The modeling suggests that during the reorganization at the LILI motif level the originally more separate TTTT residues form a tightly interacting ring (Vyklicky et al., 2015). However, once water reaches the TTTT ring (**Figure 9C**, *right*) it competes with the hydrogen bonding and the vdW contacts among the threonines and as a consequence, the M3 helices separate and form a bistable state oscillating between open and closed conformations lasting for the duration of the receptor activation by agonists. In this model, the LILI gate and TTTT ring form a functionally interconnected unit that controls the NMDAR channel gating.

From a different point of view, the GluN1(L657) is located in the vulnerable region of the receptor where structural changes (**Figure 8**) have profound functional consequences. Recent human genetic studies show the existence of multiple alterations in genes encoding NMDAR subunits (GRIN1, GRIN2A-B; Yuan et al., 2015; Hu et al., 2016). Missense mutations localized in the M3-S2 linkers of GluN1, GluN2A-C, and GluN3A-B subunits (GluN1(L655–D669) three missense mutations; GluN2A(M653-D667) one missense mutation; GluN2B(M654–D668) three missense mutations; GluN2C(M651–D665) four missense mutations; GluN3A(M768–D782) four missense mutations; GluN3B(M668–D682) three missense mutations; *note—no mutations were observed in GluN2D(M678–D692)*) were found (ClinVar[1], accessed 29-3-2018; Exome Aggregation Consortium, Cambridge, MA[2], accessed 29-3-2018; and UCSC Genome Browser[3], accessed 29-3-2018). These mutations are associated with clinical symptomatology such as mental retardation (GluN1(E662K); Hamdan et al., 2011); motor delay, delayed speech and language development (GluN2B(D668N)), and/or are likely pathogenic (GluN2B(E657G, D668Y); ClinVar[1]). Since the effects of LBD and TMD alterations are bidirectional, missense mutations may affect not only channel gating but also LBD cleft closure and thus change agonist potency, deactivation time course, and sensitivity to competitive antagonists and allosteric modulators (Jones et al., 2002; Sobolevsky et al., 2002; Yuan et al., 2005). This, together with the data presented here, indicates the structure-functional importance of the linker region and implies that receptor malfunction manifests by divergent clinical symptomatology. Finally, our data also provide a structural basis for actions of compounds affecting the efficacy of signal transduction from the LBD to the NMDAR channel gating and thus may promote the development of new drugs for treatment NMDAR channelopathies associated with severe neurological and psychiatric symptoms.

Here we identify a novel step in the gating mechanism of the NMDAR. Multidisciplinary approach was used to show that amino acids localized at the transition of the M3-S2 linkers to the M3 helices of the GluN1 and GluN2B are critically involved in stabilizing the ion channel in the closed conformation and further that GluN1(L657) and GluN2B(I655) complement the function of the previously identified GluN1(T648) and GluN2B(T647) gating residues located in the ion channel. These results provide insight into the structural organization of M3-S2 linkers and the functional interplay of the LILI motif with the TTTT ring during the course of NMDAR channel opening and closing.

AUTHOR CONTRIBUTIONS

AB and LV designed the study. ML and JK carried out and analyzed the electrophysiology experiments. JC performed molecular modeling. AB, MH and LV wrote the article.

FUNDING

This work was supported by the Czech Science Foundation 17-02300S (LV); Technology Agency of the Czech Republic TE01020028 (LV), Ministry of Health of the Czech Republic NV15-29370A (LV), European Regional Development Fund-Projects "PharmaBrain" CZ.02.1.01/0.0/0.0/16_025/0007444, Grant Agency of Charles University: 880216 (ML); Research Project of the AS CR RVO: 67985823, from the Ministry of Education, Youth and Sports of the Czech Republic: LQ1604 National Sustainability Program II (Project BIOCEV-FAR) and by the project "BIOCEV" (CZ.1.05/1.1.00/02.0109).

ACKNOWLEDGMENTS

We thank M. Kuntosova for excellent technical assistance.

SUPPLEMENTARY MATERIAL

The Supplementary Material for this article can be found online at: https://www.frontiersin.org/articles/10.3389/fnmol.2018.00113/full#supplementary-material

[1]https://www.ncbi.nlm.nih.gov/clinvar
[2]http://exac.broadinstitute.org
[3]https://genome.ucsc.edu/

REFERENCES

Amico-Ruvio, S. A., and Popescu, G. K. (2010). Stationary gating of GluN1/GluN2B receptors in intact membrane patches. *Biophys. J.* 98, 1160–1169. doi: 10.1016/j.bpj.2009.12.4276

Barnoud, J., Santuz, H., Craveur, P., Joseph, A. P., Jallu, V., De Brevern, A. G., et al. (2017). PBxplore: a tool to analyze local protein structure and deformability with Protein Blocks. *PeerJ* 5:e4013. doi: 10.7717/peerj.4013

Beck, C., Wollmuth, L. P., Seeburg, P. H., Sakmann, B., and Kuner, T. (1999). NMDAR channel segments forming the extracellular vestibule inferred from the accessibility of substituted cysteines. *Neuron* 22, 559–570. doi: 10.1016/s0896-6273(00)80710-2

Bouvier, G., Larsen, R. S., Rodríguez-Moreno, A., Paulsen, O., and Sjöström, P. J. (2018). Towards resolving the presynaptic NMDA receptor debate. *Curr. Opin. Neurobiol.* 51, 1–7. doi: 10.1016/j.conb.2017.12.020

Chang, H. R., and Kuo, C. C. (2008). The activation gate and gating mechanism of the NMDA receptor. *J. Neurosci.* 28, 1546–1556. doi: 10.1523/JNEUROSCI.3485-07.2008

Chen, P. E., Geballe, M. T., Katz, E., Erreger, K., Livesey, M. R., O'Toole, K. K., et al. (2008). Modulation of glycine potency in rat recombinant NMDA receptors containing chimeric NR2A/2D subunits expressed in *Xenopus laevis* oocytes. *J. Physiol.* 586, 227–245. doi: 10.1113/jphysiol.2007.143172

Chen, N., Luo, T., and Raymond, L. A. (1999). Subtype-dependence of NMDA receptor channel open probability. *J. Neurosci.* 19, 6844–6854.

Colquhoun, D., and Hawkes, A. G. (1990). Stochastic properties of ion channel openings and bursts in a membrane patch that contains two channels: evidence concerning the number of channels present when a record containing only single openings is observed. *Proc. R. Soc. Lond. B Biol. Sci.* 240, 453–477. doi: 10.1098/rspb.1990.0048

Craveur, P., Joseph, A. P., Esque, J., Narwani, T. J., Noël, F., Shinada, N., et al. (2015). Protein flexibility in the light of structural alphabets. *Front. Mol. Biosci.* 2:20. doi: 10.3389/fmolb.2015.00020

Dai, J., and Zhou, H. X. (2013). An NMDA receptor gating mechanism developed from MD simulations reveals molecular details underlying subunit-specific contributions. *Biophys. J.* 104, 2170–2181. doi: 10.1016/j.bpj.2013.04.013

de Brevern, A. G., Etchebest, C., and Hazout, S. (2000). Bayesian probabilistic approach for predicting backbone structures in terms of protein blocks. *Proteins* 41, 271–287. doi: 10.1002/1097-0134(20001115)41:3<271::aid-prot10>3.0.co;2-z

Dingledine, R., Borges, K., Bowie, D., and Traynelis, S. F. (1999). The glutamate receptor ion channels. *Pharmacol. Rev.* 51, 7–61.

Dore, K., Aow, J., and Malinow, R. (2016). The emergence of NMDA receptor metabotropic function: insights from imaging. *Front. Synaptic. Neurosci.* 8:20. doi: 10.3389/fnsyn.2016.00020

Dore, K., Stein, I. S., Brock, J. A., Castillo, P. E., Zito, K., and Sjostrom, P. J. (2017). Unconventional NMDA receptor signaling. *J. Neurosci.* 37, 10800–10807. doi: 10.1523/JNEUROSCI.1825-17.2017

Furukawa, H., Singh, S. K., Mancusso, R., and Gouaux, E. (2005). Subunit arrangement and function in NMDA receptors. *Nature* 438, 185–192. doi: 10.1038/nature04089

Hamdan, F. F., Gauthier, J., Araki, Y., Lin, D. T., Yoshizawa, Y., Higashi, K., et al. (2011). Excess of *de novo* deleterious mutations in genes associated with glutamatergic systems in nonsyndromic intellectual disability. *Am. J. Hum. Genet.* 88, 306–316. doi: 10.1016/j.ajhg.2011.02.001

Hu, C., Chen, W., Myers, S. J., Yuan, H., and Traynelis, S. F. (2016). Human GRIN2B variants in neurodevelopmental disorders. *J. Pharmacol. Sci.* 132, 115–121. doi: 10.1016/j.jphs.2016.10.002

Jones, K. S., VanDongen, H. M., and VanDongen, A. M. (2002). The NMDA receptor M3 segment is a conserved transduction element coupling ligand binding to channel opening. *J. Neurosci.* 22, 2044–2053.

Karakas, E., and Furukawa, H. (2014). Crystal structure of a heterotetrameric NMDA receptor ion channel. *Science* 344, 992–997. doi: 10.1126/science.1251915

Kashiwagi, K., Masuko, T., Nguyen, C. D., Kuno, T., Tanaka, I., Igarashi, K., et al. (2002). Channel blockers acting at N-methyl-D-aspartate receptors: differential effects of mutations in the vestibule and ion channel pore. *Mol. Pharmacol.* 61, 533–545. doi: 10.1124/mol.61.3.533

Kazi, R., Dai, J., Sweeney, C., Zhou, H. X., and Wollmuth, L. P. (2014). Mechanical coupling maintains the fidelity of NMDA receptor-mediated currents. *Nat. Neurosci.* 17, 914–922. doi: 10.1038/nn.3724

Kemp, J. A., Foster, A. C., Leeson, P. D., Priestley, T., Tridgett, R., Iversen, L. L., et al. (1988). 7-Chlorokynurenic acid is a selective antagonist at the glycine modulatory site of the N-methyl-D-aspartate receptor complex. *Proc. Natl. Acad. Sci. U S A* 85, 6547–6550. doi: 10.1073/pnas.85.17.6547

Kuryatov, A., Laube, B., Betz, H., and Kuhse, J. (1994). Mutational analysis of the glycine-binding site of the NMDA receptor: structural similarity with bacterial amino acid-binding proteins. *Neuron* 12, 1291–1300. doi: 10.1016/0896-6273(94)90445-6

Laube, B., Hirai, H., Sturgess, M., Betz, H., and Kuhse, J. (1997). Molecular determinants of agonist discrimination by NMDA receptor subunits: analysis of the glutamate binding site on the NR2B subunit. *Neuron* 18, 493–503. doi: 10.1016/s0896-6273(00)81249-0

Lee, C. H., Lü, W., Michel, J. C., Goehring, A., Du, J., Song, X., et al. (2014). NMDA receptor structures reveal subunit arrangement and pore architecture. *Nature* 511, 191–197. doi: 10.1038/nature13548

Lynch, M. A. (2004). Long-term potentiation and memory. *Physiol. Rev.* 84, 87–136. doi: 10.1152/physrev.00014.2003

Mayer, M. L., Vyklicky, L. Jr., and Clements, J. (1989). Regulation of NMDA receptor desensitization in mouse hippocampal neurons by glycine. *Nature* 338, 425–427. doi: 10.1038/338425a0

Nabavi, S., Kessels, H. W., Alfonso, S., Aow, J., Fox, R., and Malinow, R. (2013). Metabotropic NMDA receptor function is required for NMDA receptor-dependent long-term depression. *Proc. Natl. Acad. Sci. U S A* 110, 4027–4032. doi: 10.1073/pnas.1219454110

Nicolai, C., and Sachs, F. (2013). Solving ion channel kinetics with the QuB software. *Biophys. Rev. Lett.* 8, 191–211. doi: 10.1142/S1793048013300053

Niu, X., Qian, X., and Magleby, K. L. (2004). Linker-gating ring complex as passive spring and Ca^{2+}-dependent machine for a voltage- and Ca^{2+}-activated potassium channel. *Neuron* 42, 745–756. doi: 10.1016/j.neuron.2004.05.001

Popescu, G., and Auerbach, A. (2003). Modal gating of NMDA receptors and the shape of their synaptic response. *Nat. Neurosci.* 6, 476–483. doi: 10.1038/nn1044

Qin, F., Auerbach, A., and Sachs, F. (1997). Maximum likelihood estimation of aggregated Markov processes. *Proc. Biol. Sci.* 264, 375–383. doi: 10.1098/rspb.1997.0054

Sali, A., and Blundell, T. L. (1993). Comparative protein modelling by satisfaction of spatial restraints. *J. Mol. Biol.* 234, 779–815. doi: 10.1006/jmbi.1993.1626

Sobolevsky, A. I., Beck, C., and Wollmuth, L. P. (2002). Molecular rearrangements of the extracellular vestibule in NMDAR channels during gating. *Neuron* 33, 75–85. doi: 10.1016/s0896-6273(01)00560-8

Sobolevsky, A. I., Prodromou, M. L., Yelshansky, M. V., and Wollmuth, L. P. (2007). Subunit-specific contribution of pore-forming domains to NMDA receptor channel structure and gating. *J. Gen. Physiol.* 129, 509–525. doi: 10.1085/jgp.200609718

Sobolevsky, A. I., Rosconi, M. P., and Gouaux, E. (2009). X-ray structure, symmetry and mechanism of an AMPA-subtype glutamate receptor. *Nature* 462, 745–756. doi: 10.1038/nature08624

Sobolevsky, A. I., Yelshansky, M. V., and Wollmuth, L. P. (2004). The outer pore of the glutamate receptor channel has 2-fold rotational symmetry. *Neuron* 41, 367–378. doi: 10.1016/s0896-6273(04)00008-x

Tajima, N., Karakas, E., Grant, T., Simorowski, N., Diaz-Avalos, R., Grigorieff, N., et al. (2016). Activation of NMDA receptors and the mechanism of inhibition by ifenprodil. *Nature* 534, 63–68. doi: 10.1038/nature17679

Traynelis, S. F., Wollmuth, L. P., McBain, C. J., Menniti, F. S., Vance, K. M., Ogden, K. K., et al. (2010). Glutamate receptor ion channels: structure, regulation and function. *Pharmacol. Rev.* 62, 405–496. doi: 10.1124/pr.109.002451

Ulbrich, M. H., and Isacoff, E. Y. (2008). Rules of engagement for NMDA receptor subunits. *Proc. Natl. Acad. Sci. U S A* 105, 14163–14168. doi: 10.1073/pnas.0802075105

Vyklicky, V., Krausova, B., Cerny, J., Balik, A., Zapotocky, M., Novotny, M., et al. (2015). Block of NMDA receptor channels by endogenous neurosteroids: implications for the agonist induced conformational states of the channel vestibule. *Sci. Rep.* 5:10935. doi: 10.1038/srep10935

Vyklicky, L. Jr., Krusek, J., and Edwards, C. (1988). Differences in the pore sizes of the N-methyl-D-aspartate and kainate cation channels. *Neurosci. Lett.* 89, 313–318. doi: 10.1016/0304-3940(88)90545-9

Xu, M., Smothers, C. T., Trudell, J., and Woodward, J. J. (2012). Ethanol inhibition of constitutively open N-methyl-D-aspartate receptors. *J. Pharmacol. Exp. Ther.* 340, 218–226. doi: 10.1124/jpet.111.187179

Yao, Y., Belcher, J., Berger, A. J., Mayer, M. L., and Lau, A. Y. (2013). Conformational analysis of NMDA receptor GluN1, GluN2, and GluN3 ligand-binding domains reveals subtype-specific characteristics. *Structure* 21, 1788–1799. doi: 10.1016/j.str.2013.07.011

Yuan, H., Erreger, K., Dravid, S. M., and Traynelis, S. F. (2005). Conserved structural and functional control of N-methyl-D-aspartate receptor gating by transmembrane domain M3. *J. Biol. Chem.* 280, 29708–29716. doi: 10.1074/jbc.M414215200

Yuan, H., Low, C. M., Moody, O. A., Jenkins, A., and Traynelis, S. F. (2015). Ionotropic GABA and glutamate receptor mutations and human neurologic diseases. *Mol. Pharmacol.* 88, 203–217. doi: 10.1124/mol.115.097998

Zhu, S., Stein, R. A., Yoshioka, C., Lee, C. H., Goehring, A., Mchaourab, H. S., et al. (2016). Mechanism of NMDA receptor inhibition and activation. *Cell* 165, 704–714. doi: 10.1016/j.cell.2016.03.028

Conflict of Interest Statement: The authors declare that the research was conducted in the absence of any commercial or financial relationships that could be construed as a potential conflict of interest.

frontiers in Molecular Neuroscience

ORIGINAL RESEARCH
published: 06 April 2018
doi: 10.3389/fnmol.2018.00110

Surface Expression, Function, and Pharmacology of Disease-Associated Mutations in the Membrane Domain of the Human GluN2B Subunit

Vojtech Vyklicky[1†], Barbora Krausova[1†], Jiri Cerny[1], Marek Ladislav[1,2], Tereza Smejkalova[1], Bohdan Kysilov[1], Miloslav Korinek[1], Sarka Danacikova[1,2], Martin Horak[1], Hana Chodounska[3], Eva Kudova[3] and Ladislav Vyklicky[1]*

[1] Department of Cellular Neurophysiology, Institute of Physiology of the Czech Academy of Sciences (CAS), Prague, Czechia, [2] Department of Physiology, Faculty of Science, Charles University, Prague, Czechia, [3] Institute of Organic Chemistry and Biochemistry, Czech Academy of Sciences (CAS), Prague, Czechia

N-methyl-D-aspartate receptors (NMDARs), glutamate-gated ion channels, mediate signaling at the majority of excitatory synapses in the nervous system. Recent sequencing data for neurological and psychiatric patients have indicated numerous mutations in genes encoding for NMDAR subunits. Here, we present surface expression, functional, and pharmacological analysis of 11 *de novo* missense mutations of the human hGluN2B subunit (P553L; V558I; W607C; N615I; V618G; S628F; E657G; G820E; G820A; M824R; L825V) located in the pre-M1, M1, M2, M3, and M4 membrane regions. These variants were identified in patients with intellectual disability, developmental delay, epileptic symptomatology, and autism spectrum disorder. Immunofluorescence microscopy indicated that the ratio of surface-to-total NMDAR expression was reduced for hGluN1/hGluN2B(S628F) receptors and increased for for hGluN1/hGluN2B(G820E) receptors. Electrophysiological recordings revealed that agonist potency was altered in hGluN1/hGluN2B(W607C; N615I; and E657G) receptors and desensitization was increased in hGluN1/hGluN2B(V558I) receptors. The probability of channel opening of hGluN1/hGluN2B (V558I; W607C; V618G; and L825V) receptors was diminished ~10-fold when compared to non-mutated receptors. Finally, the sensitivity of mutant receptors to positive allosteric modulators of the steroid origin showed that glutamate responses induced in hGluN1/hGluN2B(V558I; W607C; V618G; and G820A) receptors were potentiated by 59–96% and 406-685% when recorded in the presence of 20-oxo-pregn-5-en-3β-yl sulfate (PE-S) and androst-5-en-3β-yl hemisuccinate (AND-hSuc), respectively. Surprisingly hGluN1/hGluN2B(L825V) receptors were strongly potentiated, by 197 and 1647%, respectively, by PE-S and AND-hSuc. Synaptic-like responses induced by brief glutamate application were also potentiated and the deactivation decelerated. Further, we have used homology modeling based on the available crystal structures of GluN1/GluN2B NMDA receptor followed by molecular dynamics simulations to try to relate the functional consequences of mutations to structural changes. Overall, these data suggest that *de novo* missense mutations of the hGluN2B subunit located

OPEN ACCESS

Edited by:
Argentina Lario Lago, University of California, San Francisco, United States

Reviewed by:
Angelo Keramidas, The University of Queensland, Australia
Bodo Laube, Technische Universität Darmstadt, Germany

***Correspondence:**
Ladislav Vyklicky
ladislav.vyklicky@fgu.cas.cz

[†]*Co-first authors.*

Received: *15 December 2017*
Accepted: *20 March 2018*
Published: *06 April 2018*

Citation:
Vyklicky V, Krausova B, Cerny J, Ladislav M, Smejkalova T, Kysilov B, Korinek M, Danacikova S, Horak M, Chodounska H, Kudova E and Vyklicky L (2018) Surface Expression, Function, and Pharmacology of Disease-Associated Mutations in the Membrane Domain of the Human GluN2B Subunit. Front. Mol. Neurosci. 11:110. doi: 10.3389/fnmol.2018.00110

in membrane domains lead to multiple defects that manifest by the NMDAR loss of function that can be rectified by steroids. Our results provide an opportunity for the development of new therapeutic neurosteroid-based ligands to treat diseases associated with hypofunction of the glutamatergic system.

Keywords: NMDA receptor, GluN2B, *de novo* missense mutations, neuropsychiatric disorder, neurosteroids

INTRODUCTION

The N-methyl-D-aspartate receptor (NMDAR) is a heteromeric ligand-gated ion channel permeable to Ca^{2+} that is expressed in neurons and glia. Virtually all brain and spinal cord circuits rely on excitation evoked by transient activation of NMDARs by glutamate, giving rise to NMDAR excitatory postsynaptic currents (EPSCs) to regulate physiological functions. In addition, NMDAR signaling is implicated in various forms of synaptic plasticity (Dingledine et al., 1999; Lynch, 2004; Traynelis et al., 2010; Huganir and Nicoll, 2013).

NMDAR is composed of two obligatory subunits (GluN1) and two variable ones, which can include either GluN2(A-D) or GluN3(A-B) (Traynelis et al., 2010). The GluN1 subunit is expressed throughout the central nervous system, whereas the four subtypes of GluN2(A-D) subunits have differential temporal and spatial expression patterns (Akazawa et al., 1994; Monyer et al., 1994). Expression of the GluN2B subunit (encoded by *GRIN2B* gene) dominates during rapid cortical synaptogenesis in late embryogenesis and early postnatal development, and its expression level starts to decline after birth in most brain regions (Hall et al., 2007). Several lines of evidence indicate that GluN2B subunit plays an important role in brain development, circuit formation, differentiation, and synaptic plasticity (Cohen and Greenberg, 2008). The importance of this subunit is stressed by the neonatal lethality of *GRIN2B* knock-out mice (Kutsuwada et al., 1996).

NMDAR dysfunction is implicated in a variety of nervous system disorders. Early studies indicated that glutamate triggers excitotoxicity (Olney, 1969). This form of neuronal death is dependent on calcium influx through NMDARs (Choi, 1987) and is implicated in neurological disorders such as neurodegenerative diseases, stroke, epilepsy, and traumatic brain injury (Parsons and Raymond, 2014).

Recent advances in high-throughput DNA sequencing have allowed examination of the prevalence of mutations in genes encoding NMDAR subunits among afflicted individuals. While the gene encoding for the GluN2B subunit is the most frequently *de novo* mutated *GRIN* gene in psychiatric and neurodevelopmental disorders, *de novo* mutations of *GRIN1* and *GRIN2A* genes encoding for GluN1 and GluN2A are less frequent and, interestingly, in *GRIN2C*, *GRIN3A*, and *GRIN3B*, only rare truncating mutations affecting both healthy individuals and patients suffering from neurodevelopmental disorders have been reported (Tarabeux et al., 2011; Soto et al., 2014).

GRIN2B variants—*de novo* nonsynonymous mutations, missense, nonsense, frame shift, or splice site mutations—were identified in individuals from patient cohorts with defined neurodevelopmental and psychiatric disorders such as intellectual disability, developmental delay, autism spectrum disorder, epileptic encephalopathy, schizophrenia, and to a lesser extent, attention deficit hyperactivity disorder, cerebral visual impairment, and Alzheimer's disease, as has been recently reviewed (Soto et al., 2014; Burnashev and Szepetowski, 2015; Hu et al., 2016). *GRIN2B* variants were found in the amino-terminal domain (ATD), ligand-binding domain (LBD), transmembrane domain (TMD), and carboxyl-terminal domain (CTD); rare *de novo* mutations in the ATD and CTD, but not the LBD and TMD domains, are present in the exomes of a large control population sample (Lek et al., 2016). This implies that mutations in the LBD and TMD domains may significantly alter the NMDAR channel properties. Indeed, in line with this hypothesis are results of functional examination of disease-causing mutations in the LBD (Adams et al., 2014; Lemke et al., 2014; Swanger et al., 2016). In the case of the TMD, the connections between genetic variation and consequences for the NMDAR channel function and/or trafficking are much less understood.

In this study, our goal was to elucidate the consequences of NMDAR mutations found in individuals diagnosed with neurodevelopmental disorders, in regard to the receptor-channel function and surface expression. We investigated 11 disease-associated variants in the *GRIN2B* gene located in the TMD region of the GluN2B subunit which are found as heterozygous *de novo* missense mutations. We found that some diheteromeric variants of the NMDAR have markedly decreased probability of channel opening and altered receptor surface expression. In addition, the effects of two structurally different neurosteroids, 20-oxo-pregn-5-en-3β-yl sulfate (PE-S; pregnenolone sulfate) and androst-5-en-3β-yl hemisuccinate (AND-hSuc), were tested as a pharmacological tool to correct the impaired function of mutated NMDARs.

METHODS

Transfection and Maintenance of Cells

Human embryonic kidney (HEK293T) cells (American Type Culture Collection, ATTC No. CRL1573, Rockville, MD, USA) were cultured in Opti-MEM I (Invitrogen, Carlsbad, CA, USA) with 5% fetal bovine serum (FBS; PAN Biotech, Aidenbach, Germany) at 37°C in 5% CO_2. One day before transfection, cells were plated in 24-well plates at a density of 2×10^5 cells per well. The next day, the cells were transfected with expression vectors containing human wild-type (WT) NMDAR subunits hGluN1-1a (GenBank accession no. NP_015566) and hGluN2B (GenBank accession no. NP_000825) (both genes were generous gifts from Prof. S. Traynelis, Emory University School of Medicine, Atlanta, GA) (Hedegaard et al., 2012) and green

fluorescent protein (GFP; pQBI 25, Takara, Tokyo, Japan) genes. Briefly, equal amounts (0.2 μg) of cDNAs encoding for hGluN1, hGluN2B and GFP were mixed with 0.6 μL of MATra-A Reagent (IBA, Göttingen, Germany) and added to confluent HEK293T cells cultured in 24-well plates. After trypsinization, the cells were resuspended in Opti-MEM I containing 1% FBS supplemented with 20 mM $MgCl_2$, 3 mM kynurenic acid, 1 mM D,L-2-amino-5-phosphonovaleric acid and 1 μM ketamine, and plated on 30 mm collagen and poly-L-lysine-coated glass coverslips. Transfected cells were revealed by GFP epifluorescence.

Site-directed mutagenesis of the gene encoding for hGluN2B subunit was performed using the QuikChange II XL Site-Directed Mutagenesis Kit (Agilent Technologies, Santa Clara, CA, USA) in accordance with the instructions of the manufacturer using manually designed primers purchased from Sigma-Aldrich. DpnI-treated product of PCR reaction was transformed into ultracompetent XL10-Gold *E.coli* cells, positive clones were selected, and DNA plasmids were isolated using High-Speed Plasmid Mini Kit (Geneaid, New Taipei City, Taiwan) according to the manufacturer instructions. All mutations were verified by DNA sequencing (GenSeq, Benesov u Prahy, Czech Republic and/or Eurofins Genomics, Germany). Amino acids are numbered according to the full-length protein, including the signal peptide, with the initiating methionine as number 1.

Transport

Heterologous Cell Culture

African Green Monkey kidney fibroblast (COS-7) cells were grown in Minimum Essential Medium with Earle's salts (Thermo Fischer Scientific) with 10% FBS (v/v), as described previously (Kaniakova et al., 2012).

Expression Vectors

The human version of the cDNAs encoding for the full-length GluN1-1a subunit tagged with yellow fluorescent protein (YFP-hGluN1) was generated by the QuikChange II XL site-directed mutagenesis kit according to the manufacturer's instructions, and the construct was verified by DNA sequencing.

Immunofluorescence Microscopy

COS-7 or HEK293T cells were transfected in 12-well plates with a total of 1.8 μg of cDNAs (in case of co-transfection, equal amounts of cDNAs containing YFP-hGluN1 and hGluN2B subunits were used) and 4 μl Lipofectamine™ 2000 (Thermo Fischer Scientific), as described previously (Kaniakova et al., 2012). COS-7 cells were preferred for microscopy because they attach well to glass coverslips while extensive washing procedures are being performed. HEK293T cells that attach to glass less firmly were used to confirm differences in the surface expression observed on COS-7 cells. After 24–36 h, the cells were washed in PBS, and then incubated on ice for 10 min in blocking solution containing PBS and 10% normal goat serum (v/v). After this blocking step, the cells were labeled with primary rabbit anti-GFP (Merck Millipore; Burlington, MA, USA; 1:1,000) and secondary goat anti-rabbit Alexa Fluor® 555 (Thermo Fischer Scientific; 1:1,000) antibodies. Antibodies were diluted in the blocking solution and the cells were incubated with each antibody for 30 min. The cells were then washed twice in PBS, fixed in 4% paraformaldehyde in PBS (w/v) for 20 min, and mounted using ProLong Antifade reagent (Thermo Fischer Scientific). Images were taken on an Olympus Cell^R fluorescence microscope, and the intensity of the surface and total fluorescence signals was analyzed using ImageJ software, as described previously (Lichnerova et al., 2014).

Quantitative Assay of Surface and Total Expression

COS-7 cells were prepared as described in the Immunofluorescence Microscopy section. After 38–40 h, COS-7 cells were washed with PBS, fixed for 15 min in 4% paraformaldehyde (w/v) in PBS and incubated for 1 h in PBS containing 0.2% bovine serum albumin (BSA; w/v) without (surface expression) or with (total expression) 0.1% Triton X-100 (TX-100; v/v). Cells were incubated in a primary rabbit anti-GFP antibody (Millipore, Billerica, MA; 1:500 for surface expression and 1:1,000 for total expression) diluted in PBS with 0.2% BSA for 1 h. After being washed in PBS, cells were incubated with a secondary antibody (horseradish peroxidase-conjugated donkey anti-rabbit IgG; GE Healthcare, UK; 1:1,000) for 1 h and washed in PBS. Next, 400 μl of ortho-phenylenediamine (OPD; final concentration 0.4 mg/ml) dissolved in phosphate-citrate buffer containing sodium phosphate (Sigma, St. Louis, MO) was added to cells for 30 min (surface expression) or 15 min (total expression). The color reaction was terminated with 100 μl of 3 M HCl and the optical density was determined at 492 nm using a Personal Densitometer SI (GE Healthcare, Pittsburgh, PA). The average background signal measured from cells transfected with empty vector was subtracted from data obtained from cells transfected with NMDA receptor subunits.

Electrophysiological Recording

Whole-Cell Recordings

Experiments were performed 18–36 h after the end of transfection on cultured HEK293T cells transfected with vectors containing hGluN1/hGluN2B/GFP. Whole-cell voltage clamp current recordings were performed at room temperature (21–25°C) at a holding potential of −60 mV using a patch-clamp amplifier (Axopatch 200B; Molecular Devices, Sunnyvale, CA, USA) after a capacitance and series resistance (<10 MΩ) compensation of 80–90%. Data were collected (low-pass filtered at 2 kHz and sampled at 10 kHz) and analyzed using pClamp 10 (Molecular Devices).

Patch pipettes (3–5 MΩ) were filled with an intracellular solution (ICS) containing (in mM): 120 gluconic acid, 15 CsCl, 10 BAPTA, 10 HEPES, 3 $MgCl_2$, 1 $CaCl_2$, and 2 ATP-Mg salt (pH-adjusted to 7.2 with CsOH) and extracellular solution (ECS) contained the following (in mM): 160 NaCl, 2.5 KCl, 10 HEPES, 10 glucose, 0.2 EDTA, and 0.7 $CaCl_2$ (pH-adjusted to 7.3 with NaOH). Glycine (30 μM), an NMDAR co-agonist, was present in the control and test solutions. All steroid solutions were made from freshly prepared 20 mM 20-oxo-pregn-5-en-3β-yl sulfate (PE-S; pregnenolone sulfate), and 5 mM androst-5-en-3β-yl hemisuccinate (AND-hSuc) (Krausova et al., 2018) stock in dimethyl sulfoxide (DMSO). The final dilution to ECS was made

at 50°C and followed by 1 min sonication (SONOREX DIGITEC DT 100/H, BADELIN electronic, Berlin, Germany). The same concentration of DMSO was added to all extracellular solutions. Drug applications were made with a microprocessor-controlled multibarrel fast-perfusion system. Changes in the glutamate-induced current in HEK293T cells transfected with hGluN1 and hGluN2B subunits were used to estimate the rate of solution exchange around the cell. Standard ECS was switched to the ECS diluted by water (50%) during glutamate application. The osmolarity was adjusted by sucrose to match the standard ECS. Glutamate (1 mM), glycine (10 μM) and pH was maintained constant in both solutions. The solution exchange rate was estimated to be $\tau = 12.0 \pm 0.9$ ms ($n = 6$) for the dish attached cells and $\tau \sim 200$ μs for open tip pipette (Vyklicky et al., 2016).

Single-Channel Recordings

Outside-out patches were pulled from transfected HEK293T cells, and single-channel recordings were performed at a holding potential of −60 mV (−74 mV after liquid junction potential correction) using an Axopatch 200 A amplifier (filtered at 10 kHz with a 4-pole Bessel filter, and sampled at 25 kHz). ECS and ICS were the same as solutions used for the whole-cell recording. Thick-wall borosilicate patch pipettes were pulled, coated with Sylgard 184 (Dow Corning), and fire-polished achieving resistances between 5 and 10 MΩ. Analysis of single-channel currents was performed using pClamp 10. Recordings were filtered at 2 kHz with an 8-pole Bessel filter. Opening and closing transitions were detected using a 50% threshold criterion. Openings briefer than 446 μs (2.5 × filter rise time) were excluded from the analysis (Colquhoun and Sakmann, 1985).

Data Analysis

Agonist Dose-Response Analysis

Normalized amplitudes *(I)* were fit to the following logistic equation:

$$I = 1/(1 + (\mathrm{EC}_{50}[agonist])^{h}), \quad (1)$$

where EC_{50} is the concentration of agonist that produces a half-maximal response, [*agonist*] is the glutamate or glycine concentration, and h is the apparent Hill coefficient. Dose-response for glutamate was determined from responses made in the presence of 30 μM glycine and dose-response for glycine was determined from responses made in the continuous presence of 1 mM glutamate.

Open Probability

The channel open probability (P_o) was assessed from the kinetics of the MK-801 (1 μM) inhibition of responses to 1 mM glutamate that was fitted to the kinetic model using Gepasi software (version 3.21; Mendes, 1993, 1997; Mendes and Kell, 1998). The glutamate binding steps were not considered because, in the presence of 1 mM glutamate, NMDAR exists with high probability (>99.6% as predicted from calculations using rate constants determined earlier; Cais et al., 2008) only in doubly liganded states with the channel closed (R) or open (O), and/or in a desensitized state (D).

$$D \underset{k_d}{\overset{k_r}{\rightleftharpoons}} R \underset{k_c}{\overset{k_o}{\rightleftharpoons}} O \underset{k_u}{\overset{k_b}{\rightleftharpoons}} B$$

B stands for MK-801 blocked state. The fitting procedure consisted of two steps (Turecek et al., 2004). In the first step, the response induced by 1 mM glutamate in HEK293T cells transfected with the WT or mutated hGluN1/hGluN2B receptors was analyzed for the peak (I_P) and steady state response (I_{SS}), and onset of desensitization was determined by the single exponential function (τ_d). Desensitization (D) and the kinetic constants describing the onset of desensitization (k_d) and resensitization (k_r) were determined from Equations 2–4:

$$D = 1 - (I_{SS}/I_P) \quad (2)$$

$$k_d = D/\tau_d \quad (3)$$

$$k_r = (1 - D)/\tau_d \quad (4)$$

In the second step, k_d and k_r were fixed at values obtained from the first step, and the close rate (k_c) at an arbitrary value of 200 s^{-1}. The NMDAR response recorded in the presence of 1 mM glutamate, and 1 μM MK-801 was fitted to the model while the opening rate (k_o) was set as a free parameter. MK-801 blocking rate (k_b) was set to 25 μM^{-1} s^{-1} (Huettner and Bean, 1988; Jahr, 1992; Rosenmund et al., 1995). The binding of MK-801 was virtually irreversible over the time course of the experiment for the WT and the mutated receptors, with the exception of hGluN1/hGluN2B(N615I) (Supplementary Figure S1). In the case of hGluN1/hGluN2B(N615I) receptors, the onset of MK-801 inhibition was fitted to the model where the MK-801 unblocking rate (k_u) was set as a free parameter. Microscopic open probability (P_o) was calculated as:

$$P_o = 100 \times k_o/(k_o + k_c) \quad (5)$$

Voltage Dependence of the Mg^{2+} Effect

The I–V relation of the Mg^{2+} inhibitory effect was fitted to the Boltzmann function equation of the form:

$$I(V) = ag_0(V - V_{\mathrm{rev}})/(a + [\mathrm{Mg}^{2+}]e^{-bV}) \quad (6)$$

in which g_0 is the estimated conductance of the NMDAR whole-cell response in the absence of extracellular Mg^{2+}, V_{rev} is the reversal potential of NMDA-induced current, and a, b are parameters with the following interpretation:

$$a = K_{\mathrm{d}}e^{bV} \quad (7)$$

where K_{d} represents the apparent dissociation constant for Mg^{2+} binding to the NMDAR at a given membrane potential (V) and

$$b = 2\delta F/(RT) \quad (8)$$

where δ indicates the apparent electrical distance of the Mg^{2+} binding site from the outside of the membrane and F, R, and T have their standard thermodynamic meanings (Abdrachmanova et al., 2002). Unless otherwise noted, recordings were performed at a holding potential of −60 mV (values of the holding potential were corrected for the liquid junction potential, 14 mV).

Analysis of the Steroid Effect

The relative degree of steroid-induced potentiation determined for different steroid doses in individual HEK293T cells was fit to the following logistic equation:

$$I = I_{\max}/(1+(EC_{50}/[steroid])^{h}) \quad (9)$$

where I_{max} is the maximal value of potentiation, EC_{50} is the concentration of the steroid that produces half-maximal potentiation of glutamate induced current, [*steroid*] is the steroid concentration and h is the apparent Hill coefficient.

Molecular Modeling

Homology Modeling

We have used our recently refined all-atom homology model of rat NMDAR based on available crystal structures as templates (PDB IDs-4tll, 4tlm, and 4pe5) (Karakas and Furukawa, 2014; Lee et al., 2014). The receptor in these crystal structures contains various sequence modifications (deletions, substitutions, and introduction of disulfide bridges) in order to stabilize the interaction between amino-terminal domains as well as in the TMD region. The homologous sequences were aligned using MUSCLE and visually inspected within Unipro UGENE program. The all-atom model, including the residues missing in the template structures, was prepared using the automodel function of the MODELLER 9v14 suite of programs (Sali and Blundell, 1993; Webb and Sali, 2014), including symmetry restraints for the Cα atoms of corresponding pairs of subunits. We have further created a WT receptor model with MODELLER, using the rat NMDAR model as a template. This NMDAR model quite likely reflects liganded receptor with the channel in the closed state prior to opening.

Modeling the Effect of Rare Mutations

Amino acid substitutions within the TMD were introduced using MODELLER. The WT model and each of 11 mutated NMDAR models were subjected to a 10 ns molecular dynamics (MD) simulation. The parameters of implicit solvation/lipid membrane model (EEF1/IMM1) (Lazaridis, 2003) simulations were assigned using the web-based graphical user interface CHARMM-GUI (Jo et al., 2008), and the Langevin MD simulation with 2 fs time step was performed using the CHARMM (Brooks et al., 2009) MD package version c41b1.

Visualization of Structures

Graphical representation and analysis of residues surrounding selected regions were performed using PyMOL version 1.8.3.

Statistical Analysis

All data are expressed as mean ± SEM. Group differences were analyzed using a one-way ANOVA followed by multiple comparison procedures, and Student's *t*-test or Mann-Whitney Rank Sum Test was used for comparison between experimental groups using the statistical software package SigmaStat 3.5 (Systat Software Inc., San Jose, CA, USA).

RESULTS

Rare Variants in the TMD Reduce Surface NMDAR Expression

Recently, we elucidated the effects of different NMDAR mutations in an effort to identify sites of action for inhibitory steroids (Vyklicky et al., 2015). A secondary result of these experiments was the finding that mutations in the TMD and adjacent regions often dysregulated the NMDAR function. We therefore screened available databases (https://www.ncbi.nlm.nih.gov/clinvar/) and selected 11 *de novo* mutations (P553L; V558I; W607C; N615I; V618G; S628F; E657G; G820E; G820A; M824R; L825V) located in the pre-M1, M1, M2, M3, and M4 membrane regions of the hGluN2B subunit (**Figure 1**, **Table 1**).

There is no or incomplete information available about the effects of these missense mutations on NMDAR function. We therefore evaluated the amplitude of glutamate-induced responses, relative cell-surface expression, agonist potency, receptor desensitization, relative P_o, and pharmacological properties of each of these variants as an initial step in understanding the potential role NMDAR channelopathy may play in the pathophysiology of neurological diseases. HEK293T cells transfected with WT receptors responded to glutamate (1 mM; applied in the continuous presence of 30 μM glycine) with peak currents of 66 pA/pF. Receptors with mutated hGluN2B subunit either did not respond to glutamate application (currents <5 pA) (P553L; S628F; G820E; M824R) or responded with significantly reduced amplitudes (W607C; N615I; V618G; E657G; G820A). The amplitude of responses was not significantly different for hGluN1/hGluN2B(V558I) and hGluN1/hGluN2B(L825V) receptors (Supplementary Figure S2). The differences in the peak amplitude normalized with respect to the cell capacitance must be interpreted cautiously since this is influenced by factors that we cannot fully control. We have hypothesized that reduced protein levels and/or altered receptor function may underlie reduced responses to 1 mM glutamate in HEK293T cells expressing mutated NMDARs.

Next, we used immunofluorescence microscopy to determine the surface and total protein levels of the mutated NMDARs. First, we generated a gene encoding for YFP-hGluN1 (see Methods). In the second step, COS-7 cells were transfected with genes encoding for YFP-hGluN1 and WT or mutated hGluN2B subunits. Quantitative analysis of images indicated that the ratio of surface-to-total NMDAR expression was significantly reduced for YFP-hGluN1/hGluN2B(W607C) receptors compared to WT receptors (**Figures 2A,B**), and the surface expression of YFP-hGluN1/hGluN2B(S628F) receptors (**Figure 2C**) was quite likely completely lost since the ratio of the surface-to-total receptor levels was the same as that determined for COS-7 cells transfected with YFP-hGluN1 subunit only (Horak et al., 2008; Kaniakova et al., 2012). In addition, the microscopy assay in cells expressing YFP-hGluN1/hGluN2B(G820E) receptors indicated increased surface expression compared to the WT receptors (**Figure 2D**). **Figure 2E** shows relative surface expression of the WT and mutated hGluN2B subunits. YFP-hGluN1 is not surface expressed unless it is co-expressed with the hGluN2B subunit (Okabe et al., 1999; Standley et al.,

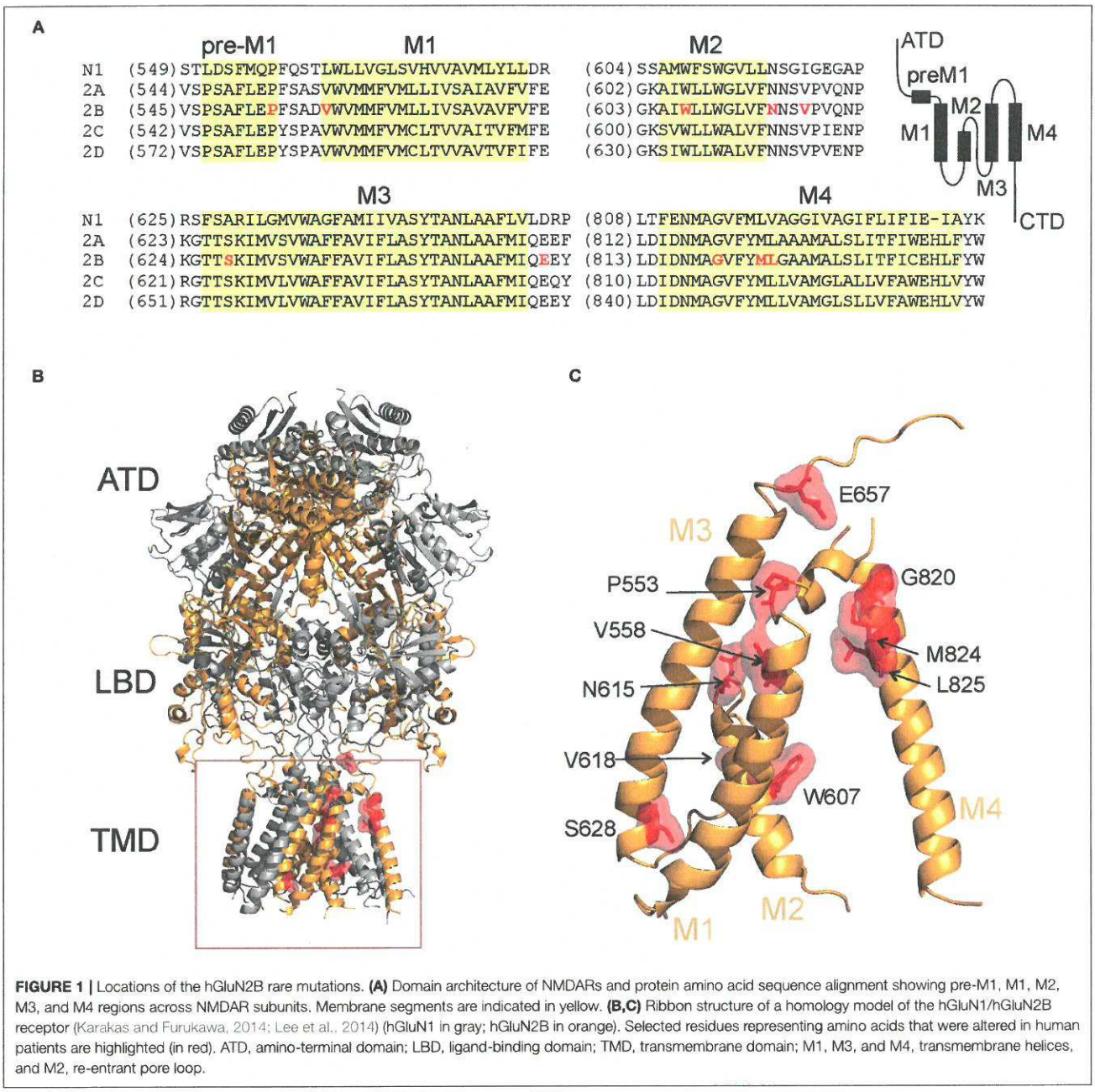

FIGURE 1 | Locations of the hGluN2B rare mutations. **(A)** Domain architecture of NMDARs and protein amino acid sequence alignment showing pre-M1, M1, M2, M3, and M4 regions across NMDAR subunits. Membrane segments are indicated in yellow. **(B,C)** Ribbon structure of a homology model of the hGluN1/hGluN2B receptor (Karakas and Furukawa, 2014; Lee et al., 2014) (hGluN1 in gray; hGluN2B in orange). Selected residues representing amino acids that were altered in human patients are highlighted (in red). ATD, amino-terminal domain; LBD, ligand-binding domain; TMD, transmembrane domain; M1, M3, and M4, transmembrane helices, and M2, re-entrant pore loop.

2000). In addition, surface-to-total expression of the WT and YFP-hGluN1/hGluN2B(W607C; S628F; and G820E) receptors was assessed using immunofluorescence microscopy on HEK293T cells and a quantitative expression assay in COS-7 cells (see Methods). The data obtained using these methods confirmed a significant decrease in the surface expression of YFP-hGluN1/hGluN2B(S628F) receptors compared to the WT and increase in the surface expression of YFP-hGluN1/hGluN2B(G820E) receptors, however, differences in the surface expression of YFP-hGluN1/hGluN2B(W607C) receptors were significant only for data gained by immunofluorescence microscopy on HEK293T cells (Supplementary Figure S3).

Thus, it is possible to explain the insensitivity of hGluN1/hGluN2B(S628F)-transfected cells to glutamate by virtually no surface expression of the receptors. In contrast, insensitivity or reduced sensitivity of cells transfected with hGluN1 and hGluN2B(P553L; W607C; N615I; V618G; E657G; G820E; G820A; or M824R) subunits contrasts with normal or increased surface expression and indicates impaired receptor function.

TABLE 1 | Selected *de novo GRIN2B* variants and their phenotypic characteristics.

GluN2B mut.	Genotype	Phenotype	Age of onset	Source
P553L	c.1658C>T	ID, hypotonia	Early postnatal	de Ligt et al., 2012
V558I	c.1672G>A	ID	-	Hamdan et al., 2014; Lelieveld et al., 2016
W607C	c.1821G>T	ID, DD, dysmorphic features	-	Yavarna et al., 2015
N615I	c.1844A>T	WS, ID	7 weeks	Lemke et al., 2014
V618G	c.1853T>G	ID, WS, Epi-encephalopathy	4 months	Lemke et al., 2014
S628F	c.1883C>T	ID, DD, Epi-encephalopathy	-	Platzer et al., 2017
E657G	c.1970A>G	ID, DD	-	Platzer et al., 2017
G820E	c.2459G>A	ID, microcephaly	Early postnatal	Hamdan et al., 2014
G820A	c.2459G>C	ID, DD, DMD, ES, GVL, ASD	-	Platzer et al., 2017
M824R	c.2471T>G	ID, DD, microcephaly, Rett-like picture, Epi activity on EEG	2 months	Zhu et al., 2015
L825V	c.2473T>G	ASD	-	Awadalla et al., 2010; Swanger et al., 2016

ID, intellectual disability; DD, developmental delay; WS, West Syndrome; DMD, Dyskinetic Movement Disorder; ES, epileptic spasms; GVL, generalized cerebral volume loss; ASD, Autism Spectrum Disorder; Epi, epilepsy and/or seizures, infantile spasms.

Mutations Related to Human Neurological Diseases Decrease Agonist Potency

Seven mutations in the TMD responded to 1 mM glutamate and 30 μM glycine with currents that allowed reliable dose-response analysis of the agonist-induced responses. This analysis indicated that glutamate is 3.2- and 1.7-fold less potent at hGluN1/hGluN2B(W607C; and N615I) receptors and 2.3-fold more potent at hGluN1/hGluN2B(E657G) receptors than at the WT receptors (**Figure 3A**, **Table 2**). Similar analysis of glycine dose-response suggested that glycine is 2.0- and 1.8-fold less potent at hGluN1/hGluN2B(W607C; and E657G) receptors than at the WT receptors (**Figure 3B**, **Table 2**). Altered glutamate potency in hGluN1/hGluN2B(E657G) receptors and altered glycine potency in hGluN1/hGluN2B(W607C; and E657G) receptors was accompanied by a diminished value of the Hill coefficient indicating on altered degree of cooperativity of the agonists binding to the receptor (Weiss, 1997).

Mutations in the TMD Alter Receptor Desensitization and Decrease Channel Open Probability

To evaluate the effects of mutations in the TMD on NMDAR desensitization, the receptors were activated by a saturating concentration of glutamate (1 mM) in the continuous presence of glycine (30 μM). The analysis of the desensitization—a time-dependent decline of responses (see Equation 2 for definition)—indicated that WT receptors desensitized on average by 16.1% (**Figure 4A**). The desensitization was significantly increased to 72.9% in hGluN1/hGluN2B(V558I) receptors (**Figure 4B**) and was not significantly changed in hGluN1/hGluN2B(L825V) receptors (**Figure 4C**); by contrast, hGluN1/hGluN2B(V618G) receptors desensitized only by 4.1% (**Figure 4D**).

The time course of the desensitization onset of responses induced in the WT and hGluN1/hGluN2B(V558I; W607C; N615I; and L825V) receptors was next analyzed and desensitization (k_d) and (k_r) resensitization rate constants were determined (see Equations 2-4). The desensitization observed in the WT receptor responses was characterized by $k_d = 0.24 \pm 0.08\ s^{-1}$ ($n = 10$). The value of k_d was significantly increased in hGluN1/hGluN2B[V558I ($3.55 \pm 0.46\ s^{-1}$; $n = 7$); and W607C ($1.59 \pm 0.54\ s^{-1}$; $n = 4$)] receptor responses (one-way ANOVA, $p < 0.001$; followed by multiple comparisons of the rate constant determined in the mutated receptors vs. the WT; Dunnett's method, $p < 0.050$). The values of the k_d determined in hGluN1/hGluN2B[N615I ($0.48 \pm 0.14\ s^{-1}$; $n = 4$); and L825V ($0.43 \pm 0.16\ s^{-1}$; $n = 6$)] receptor responses was not significantly different from that determined in WT. WT receptor responses were characterized by $k_r = 1.06 \pm 0.17\ s^{-1}$ ($n = 10$). The value of the k_r was significantly increased in hGluN1/hGluN2B[W607C ($4.79 \pm 1.22\ s^{-1}$; $n = 4$); and N615I ($2.61 \pm 0.51\ s^{-1}$; $n = 4$)] receptor responses (one-way ANOVA, $p < 0.001$; followed by multiple comparisons of the rate constant determined in the mutated receptors vs. the WT; Dunnett's method, $p < 0.050$). The values of the k_r determined in hGluN1/hGluN2B[V558I ($1.29 \pm 0.28\ s^{-1}$; $n = 7$); and L825V ($1.47 \pm 0.20\ s^{-1}$; $n = 6$)] receptors was not significantly different from that determined in WT receptors. Low amplitude of the hGluN1/hGluN2B(V618G) receptor responses precluded detailed analysis of the rate constants characterizing receptor desensitization.

To evaluate the effects of mutations in the TMD on P_o, the WT and mutated receptors were activated by a saturating concentration of glutamate (1 mM) and the rate of channel block by 1 μM MK-801 was fitted to the kinetic model and the P_o determined (see Methods and Equation 5). Using this approach, the P_o of the human WT receptors was determined to be $10.5 \pm 1.3\%$ ($n = 10$) (**Figure 4A**). This value is not different from the P_o determined from the analysis of single-channel of activity induced by 1 mM glutamate in cell-attached patches ($P_o = 10.6 \pm 2.9\%$ ($n = 12$); unpaired t-test, $p = 0.977$) (see Supplementary Figure S4) and, in addition, it agrees well with that determined for rat GluN1/GluN2B receptors (Chen et al., 1999).

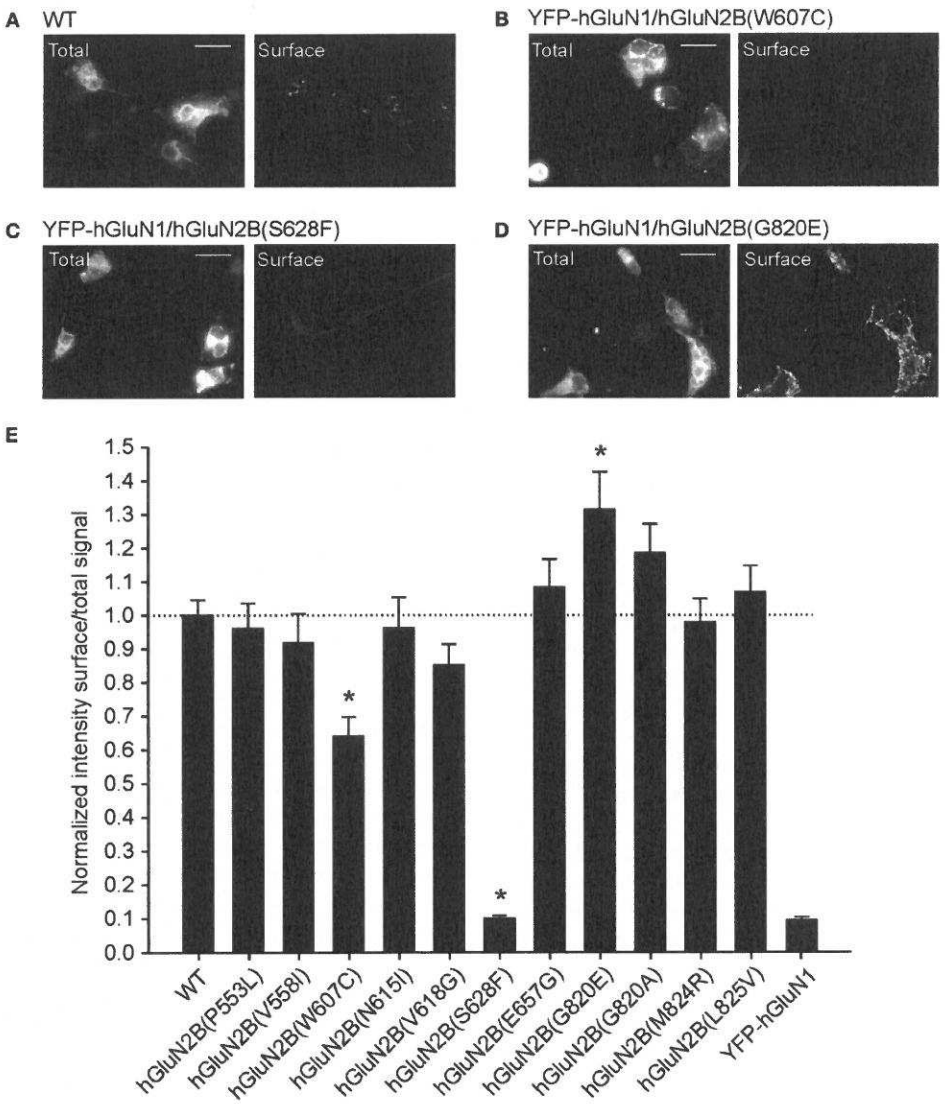

FIGURE 2 | Mutations in the TMD of hGluN2B subunit affect the NMDAR surface expression. **(A–D)** Representative images of the total (left panel) and surface (right panel) pools of YFP-hGluN1 expressed in COS-7 cells. COS-7 cells were transfected with WT **(A)**, YFP-hGluN1/hGluN2B(W607C) **(B)**, YFP-hGluN1/hGluN2B(S628F) **(C)**, and YFP-hGluN1/hGluN2B(G820E) **(D)** receptors. A scale bar in **(A–D)** represents 20 μm. **(E)** An immunofluorescence microscopy was used to determine relative surface-to-total NMDAR levels in COS-7 cells transfected with only YFP-hGluN1 subunit for control (YFP-hGluN1) or both the YFP-hGluN1 and hGluN2B (WT) or mutated hGluN2B subunit. Data show mean ± SEM; $n = 35$ in three experiments. *$p < 0.05$ relative to WT, one-way ANOVA (Multiple comparisons vs. WT-Dunnett's method). For original images see (Supplementary Figures S5–S12).

Superimposed traces indicate that in hGluN1/hGluN2B(V558I; and L825V) receptors, the onset of MK-801 inhibition was decelerated compared to WT receptors (**Figures 4A–C**). The results of the analysis indicated that the P_o decreased from 10.5% in WT receptors to 0.66% in hGluN1/hGluN2B(V558I) and 1.47% in hGluN1/hGluN2B(L825V) receptors. Similar decrease in P_o was observed in hGluN1/hGluN2B(W607C; and V618G) receptors (**Figure 4E**). These data indicate that *de novo* mutations in the TMD alter receptor desensitization and P_o.

Mutations in the Channel Pore Alter Mg^{2+} Inhibition and Single-Channel Amplitude

Structural data indicate that residues hGluN2B(W607; N615; and V618) are part of the NMDAR channel pore. A functionally important feature of NMDARs is the voltage-dependent inhibition by extracellular Mg^{2+}, and several residues located within the ion channel pore have been shown to alter Mg^{2+} sensitivity (Kuner et al., 1996; Kupper et al., 1996; Williams et al., 1998). Fitting the current-voltage relation of WT receptor responses recorded in the presence of 1 mM Mg^{2+} to the

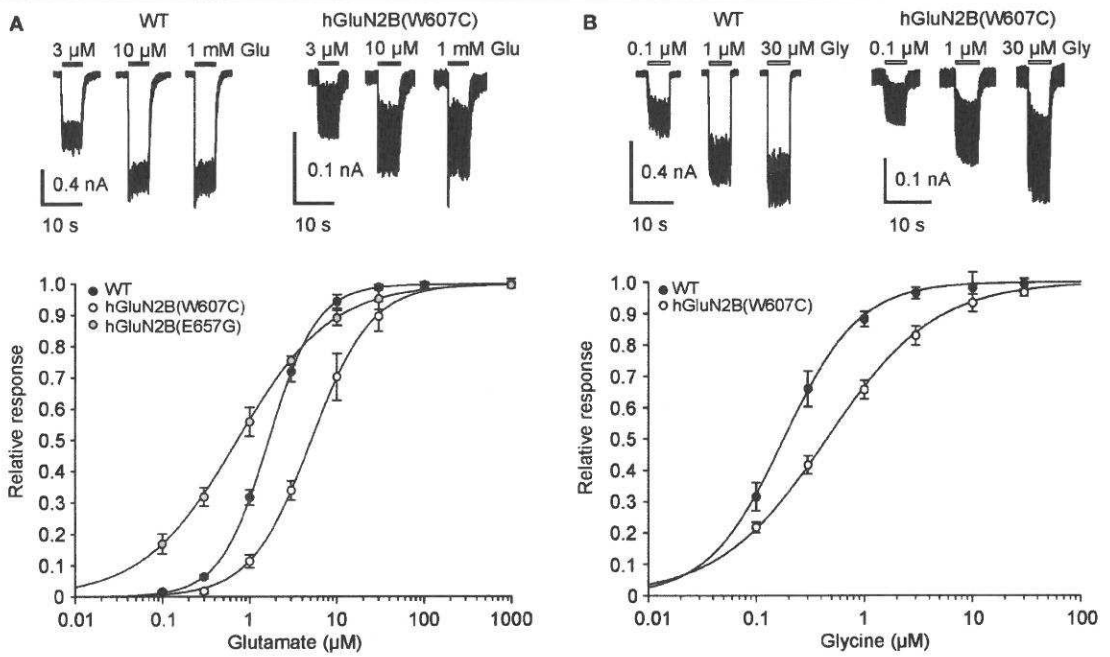

FIGURE 3 | hGluN2B rare variants alter glutamate and glycine potency. **(A)** Representative recordings of responses to 3, 10, and 1,000 μM glutamate applications made in the presence of 30 μM glycine are shown for HEK293T cells expressing WT and hGluN1/hGluN2B(W607C) receptors. Peak concentration-response relationship for glutamate activation of WT, hGluN1/hGluN2B(W607C; and E657G) receptors. **(B)** Representative recordings of responses to 0.1, 1, and 30 μM glycine applications made in the presence of 1 mM glutamate are shown for HEK293T cells expressing WT and hGluN1/hGluN2B(W607C) receptors. Peak concentration-response relationship for glycine activation of WT and hGluN1/hGluN2B(W607C) receptors. Data points in **(A,B)** are averaged values of relative currents form at least five independent measurements. Error bars represent SEM. Values of glutamate and glycine EC_{50}, *h* and *n* are listed in **Table 2**.

TABLE 2 | Summary of the agonist potency data.

Mutation	Glutamate			Glycine		
	EC_{50} (μM)	*h*	*n*	EC_{50} (μM)	*h*	*n*
hGluN2B(WT)	1.6 ± 0.1	1.4 ± 0.1	15	0.22 ± 0.03	1.45 ± 0.11	9
hGluN2B(V558I)	1.6 ± 0.3	1.5 ± 0.2	5	0.22 ± 0.05	1.14 ± 0.05	5
hGluN2B(W607C)	5.1 ± 0.4*	1.3 ± 0.2	5	0.45 ± 0.08*	0.87 ± 0.05*	7
hGluN2B(N615I)	2.7 ± 0.2*	1.2 ± 0.1	5	0.31 ± 0.02	1.41 ± 0.10	5
hGluN2B(V618G)	1.7 ± 0.2	1.2 ± 0.1	5	0.28 ± 0.03	1.43 ± 0.09	5
hGluN2B(E657G)	0.7 ± 0.1*	0.8 ± 0.1*	9	0.39 ± 0.08*	0.97 ± 0.10*	5
hGluN2B(G820A)	1.5 ± 0.3	1.0 ± 0.2	4	0.20 ± 0.09	1.15 ± 0.05	3
hGluN2B(L825V)	1.5 ± 0.1	1.1 ± 0.1	9	0.16 ± 0.01	1.26 ± 0.12	5

The data are expressed as mean ± SEM.
n is the number of cells recorded from.
**$p < 0.05$; statistical tests on potency were performed on $logEC_{50}$ and logHill compared to the corresponding WT; one-way ANOVA, Tukey post-hoc Dunnett's method.*

Boltzmann function (Equations 6-8) revealed that the affinity for Mg^{2+} in the absence of an electric field ($K_{d(0\ mV)}$) was 5.9 ± 2.3 mM and δ = 0.45 ± 0.07 (n = 5) (**Figure 5A**). hGluN1/GluN2B(N615I) receptor responses were only slightly affected by 1 mM Mg^{2+}, and the fit to the Boltzmann function provided unreliable values for both $K_{d(0\ mV)}$ and δ (**Figure 5A**). The responses induced in hGluN1/hGluN2B(W607C; and V618G) receptors were small, precluding detailed analysis of the current-voltage relation. Based on the relative inhibitory effect of 1 mM Mg^{2+} at a holding potential of −60 mV, which decreased from 97 ± 2% (n = 5) in WT to 35 ± 3% (n = 6) in hGluN1/hGluN2B(W607C), we infer that Mg^{2+} binding within these receptor channels is also altered. The responses induced by hGluN1/hGluN2B(V618G) were small, precluding any reliable analysis of the Mg^{2+} effect. These results agree well with reduced Mg^{2+} block observed in mutated receptors (Lemke et al., 2014).

Next, we aimed to characterize the effect of mutations on the ion permeation employing single-channel recording from outside-out patches. **Figure 5B** shows records of channel activity in outside-out patches recorded in response to the application of 1 mM glutamate in the presence of Mg^{2+}-free extracellular solution at a holding potential of −60 mV (−74 mV after junction potential correction). The mean amplitude of the principal single-channel current was decreased from −4.5 ± 0.1 pA (n = 6) in the WT receptors to −2.4 ± 0.1 pA (n = 5) for hGluN1/hGluN2B(W607C) receptor channels ($p < 0.001$, compared to WT), −1.8 ± 0.1 pA (n = 5) for hGluN1/hGluN2B(N615I) receptor channels ($p < 0.001$, compared to WT), and −3.6 ± 0.1 pA (n = 5) for hGluN1/hGluN2B(V618G) receptor channels ($p < 0.001$, compared to WT). These data indicate that mutations in the NMDAR channel pore have opposing effects –an increase in responses due to the reduced Mg^{2+} inhibitory effect and a

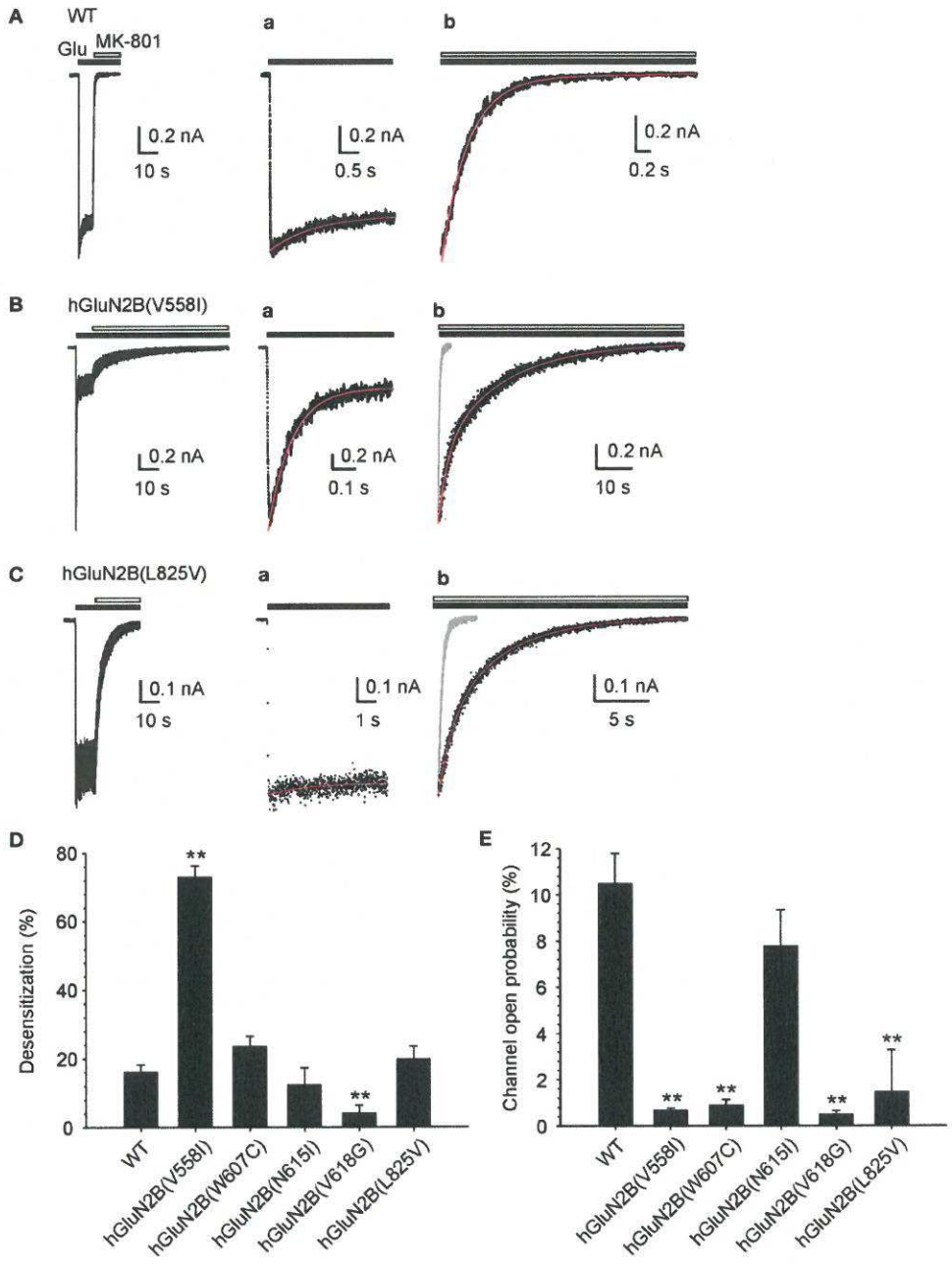

FIGURE 4 | Mutations in the TMD alter receptor desensitization and P_O. **(A-C)** Representative currents induced in WT, hGluN1/hGluN2B(V558I; and L825V) receptors by fast application of 1 mM glutamate (in the continuous presence of 30 μM glycine) and their inhibition by MK-801 (1 μM). **(Aa-Ca)** Show the response to glutamate at an expanded time scale. Desensitization of WT receptors was best described by rate constants $k_d = 0.17\ s^{-1}$ and $k_r = 0.69\ s^{-1}$; desensitization of hGluN1/hGluN2B(V558I) receptors by $k_d = 4.06\ s^{-1}$ and $k_r = 1.12\ s^{-1}$, and desensitization of hGluN1/hGluN2B(L825V) receptors by $k_d = 0.11\ s^{-1}$ and $k_r = 0.83\ s^{-1}$ (indicated by a superimposed red trace). **(Ab-Cb)** Show the onset of MK-801 inhibition on an expanded time scale. The time course of the onset of MK-801 (gray response in Bb and Cb) inhibition was best described by $P_O = 12.2\%$ for WT receptors, $P_O = 0.61\%$ for hGluN1/hGluN2B(V558I) receptors, and $P_O = 1.16\%$ for hGluN1/hGluN2B(L825V) receptors (indicated by a superimposed red trace) (see Methods section for details of the analysis procedure). Graphs show the summary of mean desensitization **(D)** and P_O **(E)** ± SEM (*n*) for WT and mutated receptors. The differences in the mean values of desensitization and P_O determined for the WT and mutated receptors was statistically significant; Kruskal-Wallis one-way ANOVA on Ranks, $p < 0.001$; subsequent Mann-Whitney Rank Sum Test or unpaired *t*-test was used to assess the significance compared to the WT, $^*p = 0.001$–0.05, $^{**}p < 0.001$.

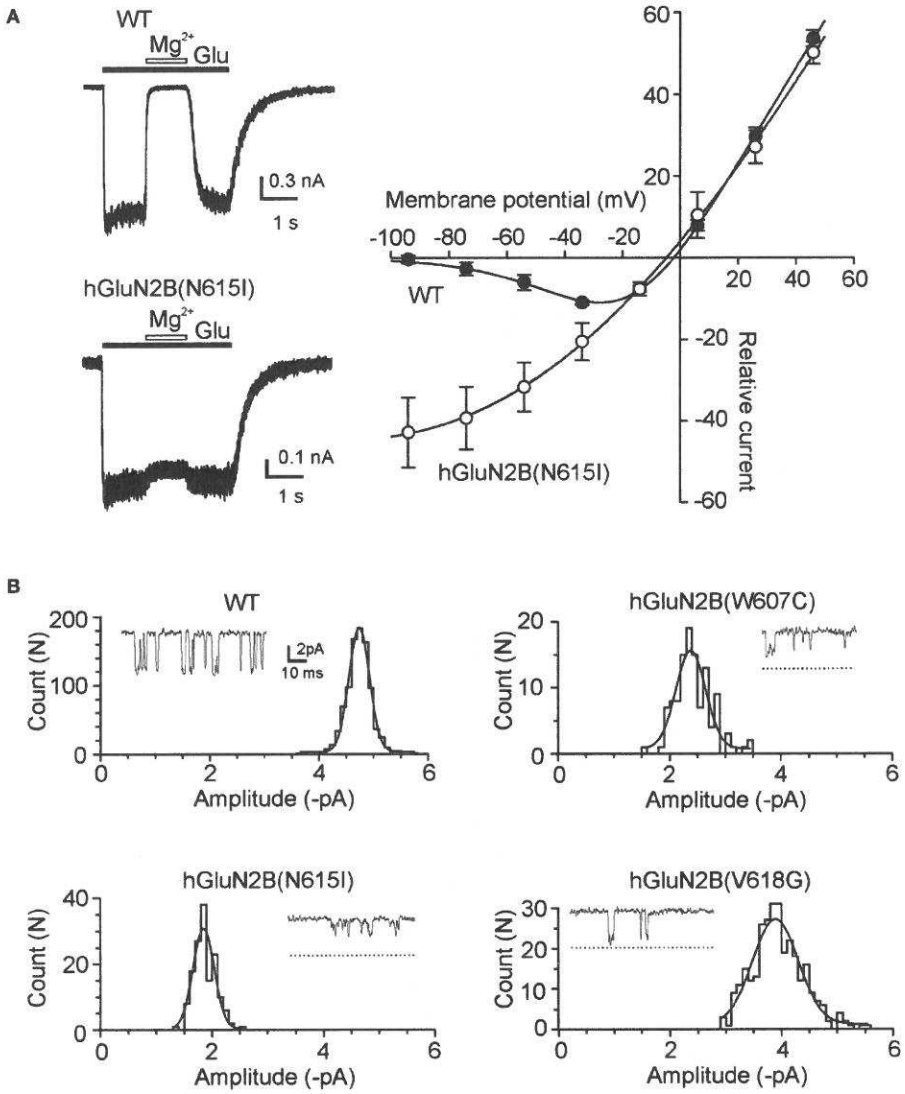

FIGURE 5 | Mutations in the channel pore alter ion permeation. **(A)** Effect of Mg^{2+} on WT and hGluN1/GluN2B(N615I) receptor responses. Whole-cell current responses were induced by 1 mM glutamate in the absence and presence of 1 mM Mg^{2+} at a holding potential of −60 mV. *I-V* relations without Mg^{2+} were fit by a linear equation and normalized to have a slope of 1. Corresponding responses recorded in the presence of Mg^{2+} were normalized and fitted to the Boltzmann equation (Equations 6–8). **(B)** Examples of single-channel openings induced in WT, hGluN1/hGluN2B(W607C; N615I; and V618G) receptors by 1 mM glutamate. Dashed lines show where the current levels identified from the fit to the amplitude distribution for the WT would fall. For individual patches the distribution is shown fitted with a single Gaussian component. Glutamate-induced single-channel currents had mean amplitude: −4.7 pA (WT), −2.4 pA [hGluN1/hGluN2B(W607C)], −1.9 pA [hGluN1/hGluN2B(N615I)], and −3.9 pA [hGluN1/hGluN2B(V618G)].

reduction of responses due to the decrease in the single-channel amplitude; the overall effect will be a function of the membrane potential.

GluN2B(L825V) Mutation Enhances Sensitivity to Endogenous and Synthetic Steroids

Endogenous steroids are potent allosteric modulators of NMDAR activity (Korinek et al., 2011). The sensitivity of the mutant receptors to extracellular PE-S, a steroid that has a positive allosteric and subunit-dependent effect at NMDAR (with preference for GluN2A/B subunits) (Wu et al., 1991; Horak et al., 2006), was evaluated by generating dose-response curves for the potentiation of responses to glutamate. In addition, we analyzed the potentiating effect for AND-hSuc, a more potent synthetic PE-S analog (Krausova et al., 2018). Since the effect of steroids with a potentiating effect at NMDAR is disuse-dependent (Horak et al., 2004), a low concentration of glutamate (1 μM) was used in these experiments. **Figures 6A,B** shows that PE-S and AND-hSuc

potentiate both the WT and mutated receptors, although to a different extent. Analysis revealed that GluN1/GluN2B(L825V) receptors were significantly more potentiated by a nearly saturating concentration of PE-S (100 μM) than responses induced in the WT and hGluN1/hGluN2B(V558I; W607C; V618G; and G820A) receptors (**Figure 6C**; Kruskal-Wallis one-way ANOVA on Ranks, $p < 0.001$; unpaired t-test, $p < 0.001$). Similarly to the effect of PE-S, AND-hSuc (30 μM) potentiated glutamate responses induced in the mutated receptors with a higher potency than in the WT (**Figure 6C**; Kruskal-Wallis one-way ANOVA on Ranks, $p < 0.001$; unpaired t-test, $p < 0.001$). GluN1/GluN2B(L825V) receptors were potentiated robustly (1647%) by AND-hSuc. Receptors containing hGluN1 and hGluN2B(V558I; W607C; V618G; or G820A) subunits were potentiated to an extent not significantly different from that determined for the WT receptors (**Figure 6C**; $p = 0.117$–0.412 for PE-S; $p = 0.448$–0.966 for AND-hSuc). Dose-response analysis of the effect of PE-S and AND-hSuc indicated that the increased steroid potentiation of GluN1/GluN2B(L825V) receptors was attributable to the increase in steroid efficacy rather than potency (**Figures 6D,E**).

The time course of the NMDAR responses following brief glutamate application has been suggested to mimic the time course of the NMDAR component of the EPSCs (Lester et al., 1990). To evaluate the effects of steroids on the deactivation time course, we measured current responses induced by a brief (~5 ms) application of 1 mM glutamate to HEK293T cells expressing WT or hGluN1/hGluN2B(L825V) receptors. In the WT receptors, PE-S (100 μM) significantly increased the amplitude of synaptic-like responses and slowed the deactivation (**Figure 6F**, **Table 3**). The deactivation of hGluN1/hGluN2B(L825V) receptors was not significantly different ($p = 0.696$) from that determined for the WT receptors. This agrees well with the prediction made from the simulation of responses to brief glutamate application to NMDARs that have diminished P_o but unaltered glutamate EC_{50} (**Figure 4E**, **Table 2**). In the hGluN1/hGluN2B(L825V) receptors, PE-S (100 μM) significantly increased the amplitude of synaptic-like responses and slowed the deactivation (**Figure 6G**, **Table 3**).

Next, we estimated the relative charge transfer recorded for synaptic-like responses in the presence of PE-S. The charge transfer was calculated as a product of the response amplitude and deactivation time course, and its value increased 3.3-fold for the WT and 3.8-fold for hGluN1/hGluN2B(L825V) receptors when synaptic-like responses were recorded in the presence of PE-S (100 μM) (**Table 3**). Even though this augmentation of synaptic-like responses is prominent, it is not sufficient to compensate for a 7-fold diminution of the synaptic-like response of hGluN1/hGluN2B(L825V) receptors due to their decreased P_o (**Figure 4E**). The increase in the charge transfer was much more robust for synaptic-like responses recorded in the presence of AND-hSuc (30 μM)-its value increased 161-fold for the WT and 180-fold for hGluN1/hGluN2B(L825V) receptors (**Figures 6F,G**, **Table 3**). Estimates indicate that the augmentation of synaptic-like responses is more than sufficient to compensate for a 7-fold diminution of the synaptic-like response of hGluN1/hGluN2B(L825V) receptors when we take into an account their decreased P_o (**Figure 4E**).

Altogether, these results suggest that (i) PE-S and AND-hSuc have a potentiating effect at human WT receptors; (ii) AND-hSuc is a more potent positive allosteric modulator than PE-S; (iii) even though the potentiating effect of steroids at NMDAR is associated with a disuse-dependent mechanism of action, the effect of both PE-S and AND-hSuc was similar at WT and mutated receptors (hGluN1/hGluN2B(V558I; W607G; and V618G) receptors) that have P_o diminished ~10-fold; (iv) hGluN1/hGluN2B(L825V) receptors were potentiated by both steroids more than WT and other mutated receptors; (v) AND-hSuc-induced increase in the charge transfer of synaptic-like responses can compensate for the mutation-induced diminution of P_o in hGluN1/hGluN2B(L825V) receptors; and (vi) an increase in the positive allosteric effect of both steroids at hGluN1/hGluN2B(L825V) receptors is due to an increase in their efficacy rather than potency.

DISCUSSION

The development of next-generation DNA sequencing has given rise to unique data linking patient variants in *GRIN1* and *GRIN2* genes to neurological and psychiatric disorders. While the list of rare variants expands rapidly, the consequences for receptor biogenesis, its structure, function, and pharmacology have been only partially revealed (Yuan et al., 2014; Swanger et al., 2016; Chen et al., 2017; Ogden et al., 2017; Platzer et al., 2017). In this study, we investigated 11 disease-associated rare variants in the GluN2B TMD and found that dysregulation of NMDARs involves multiple mechanisms - altered surface expression, agonist potency, receptor desensitization, probability of channel opening, single-channel currents, Mg^{2+} sensitivity - and their combination. Through functional assessments, we show that loss-of-function variants can be rectified by a pharmacological approach, using PE-S and its synthetic analog AND-hSuc. Impaired surface expression and/or receptor function have important implications that may help to find links connecting genetic variation to disease as well as to understand the role of NMDAR variants in neurodevelopmental disorders (Mcrae et al., 2017).

Mechanisms of hGluN2B(P553L; and V558I) Dysregulation

Crystal structures of the GluN1/GluN2B receptor show that the LBD, the pre-M1 helix, and the M1 helix are structurally coupled, indicating a role in receptor gating (Lee et al., 2014). Conserved residues GluN2B(P553; and V558) are part of the pre-M1 and M1 helix, respectively (Sobolevsky et al., 2009; Karakas and Furukawa, 2014; **Figure 1A**), and despite their physical proximity, the mutation hGluN2B(P553L) rendered the transfected cells virtually glutamate nonresponsive while hGluN2B(V558I) receptors exhibited similar current responses to 1 mM glutamate to the WT, although with a prominent desensitization and a decreased P_o (Supplementary Figure S2, **Figures 4D,E**). Surface expression

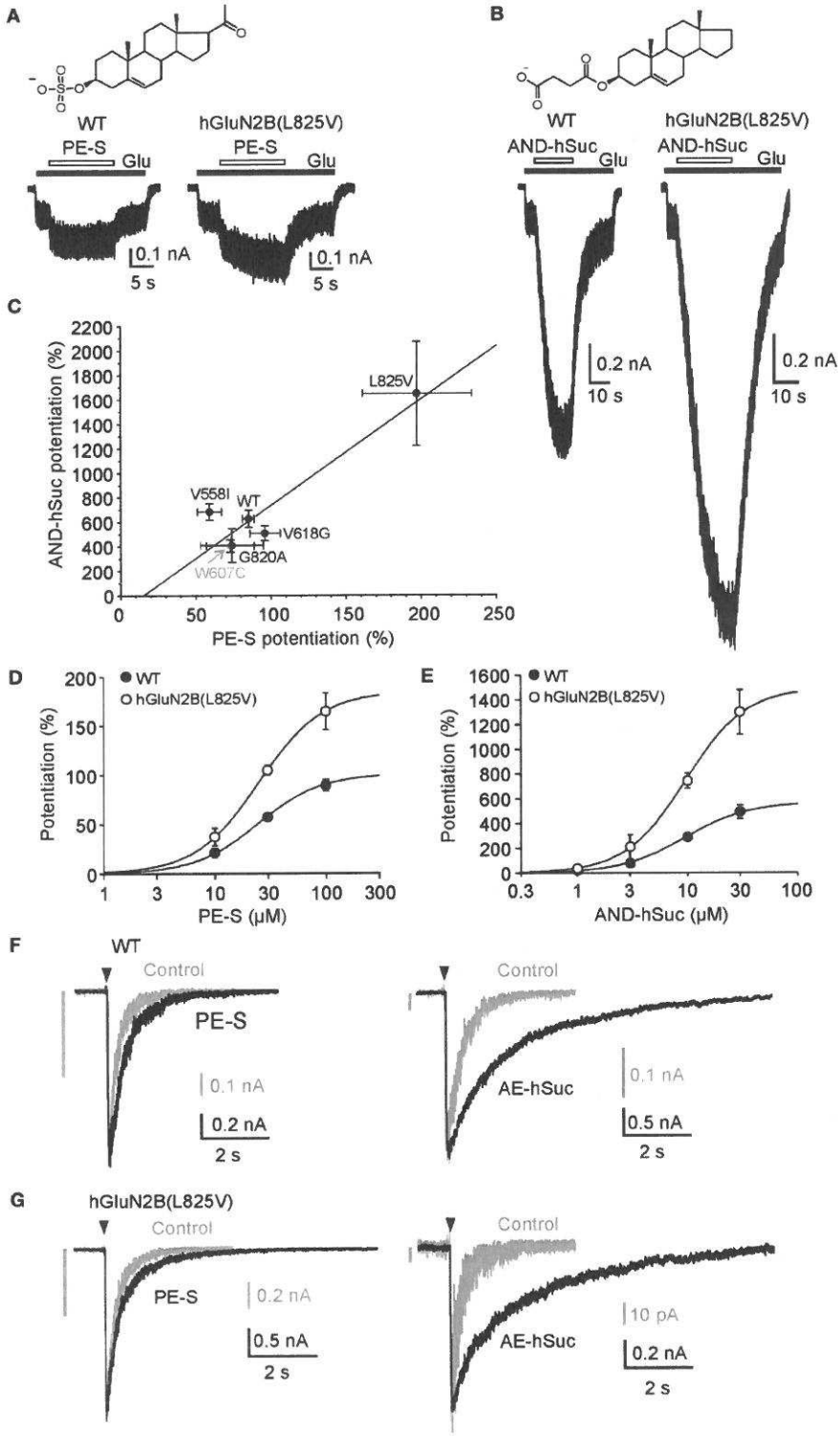

FIGURE 6 | hGluN1/hGluN2B(L825V) has an enhanced sensitivity to steroids. **(A)** Representative responses are shown for WT and hGluN1/hGluN2B(L825V) receptors. PE-S (100 μM) **(A)** and AND-hSuc (30 μM) **(B)** potentiated the WT receptor responses induced by co-application with 1 μM glutamate in the continuous presence of 30 μM glycine to a different extent (by 85% and 575%, respectively). Both steroids potentiated responses induced in hGluN1/hGluN2B(L825V) receptors

(Continued)

FIGURE 6 | ~2-fold more than in WT receptors. Structure of PE-S **(A)** and AND-hSuc **(B)**. **(C)** Graph shows relative PE-S (100 μM) potentiation ± SEM (n = 5–31) plotted vs. that induced by AND-hSuc (30 μM) ± SEM in the WT and in mutated receptors. Data were fit by a linear regression (Correlation coefficient r = 0.928; p = 0.00764). Concentration dependency for PE-S **(D)** and AND-hSuc **(E)** induced potentiation of WT and hGluN1/hGluN2B(L825V) receptors activated by 1 μM glutamate in the continuous presence of 30 μM glycine. Parameters of the fit (see Equation 9) were for the WT receptors: PE-S induced relative maximal potentiation I_{max} = 101 ± 9%; EC_{50} = 24.3 ± 1.8 μM with h = 1.54 ± 0.08 (n = 7); AND-hSuc I_{max} = 570 ± 57%; EC_{50} = 9.5 ± 1.0 μM; h = 1.50 ± 0.16 (n = 6). In hGluN1/hGluN2B(L825V) receptors: PE-S induced I_{max} =185 ± 50% (p = 0.030 compared to WT); EC_{50} = 24.8 ± 1.2 μM (p = 0.842 compared to WT) with h = 1.52 ± 0.12 (n = 5); AND-hSuc I_{max} = 1492 ± 514% (p = 0.030 compared to WT); EC_{50} = 9.6 ± 2.3 μM (p = 0.961 compared to WT) with h = 1.58 ± 0.36 (n = 6). **(F,G)** Normalized representative current responses of WT and hGluN1/hGluN2B(L825V) receptors induced by brief (5 ms) application of 1 mM glutamate made in the ECS (Control, gray) and in the presence of PE-S (100 μM) or AND-hSuc (30 μM) following steroid pre-application for (>30 s). The vertical gray bar indicates the amplitude of the control response at the same amplitude scale as that recorded in the presence of steroid. See **Table 3** for values and statistics on the steroid effect.

TABLE 3 | Summary of the pharmacological properties for synaptic-like responses.

Receptor		Control	PE-S (100 μM)	Control	AND-hSuc (30 μM)
WT	Potentiation (%)	–	98.7 ± 11.5 (5)	–	924.5 ± 172.7 (5)
	τ (ms)	307 ± 14 (5) †	499 ± 20 (5)‡*	370 ± 35 (5)†	5,961 ± 542 (5)†*
	Deceleration	–	1.63 ± 0.06 (5)	–	16.36 ± 1.44 (5)†
	Charge transfer	–	3.26 ± 0.30 (5)	–	161.4 ± 20.3 (5)
hGluN2B(L825V)	Potentiation (%)	–	140.8 ± 10.8 (5)	–	2,323 ± 121 (5)
	τ (ms)	323 ± 9 (5)†	507 ± 28 (5)‡*	335 ± 29 (5)†	2,467 ± 168 (5)†*
	Deceleration	–	1.57 ± 0.05 (5)	–	7.19 ± 0.59 (5)†
	Charge transfer	–	3.79 ± 0.25 (5)	–	179.7 ± 9.1 (5)

The data are expressed as mean ± SEM (n) is the number of cells recorded from.
**$p < 0.001$ compared to WT; paired t-test.*
† τ determined from the single exponential fit.
‡ τ_w determined from the double exponential fit.
Deceleration is defined as $\tau_{steroid}/\tau_{control}$.
Charge transfer is defined as $\tau \times (potentiation/100) + 1$).

of YFP-hGluN1/hGluN2B(P553L) receptors was not altered (**Figure 2E**; however, see Ogden et al., 2017), who show a moderate reduction (by 33%) indicating that minimal current responses to 1 mM glutamate in hGluN1/hGluN2B(P553L) receptors are not due to the lack of surface expression but rather a functional alteration in the receptor. We may hypothesize that the loss of function in hGluN1/hGluN2B(P553L) receptors may be attributed to receptor desensitization since rat GluN1/GluN2A(P552R) receptors, homologous in position to GluN2B(P553), desensitize profoundly (by 98.5%). It is less likely that it is due to altered agonist potency and P_o since rat GluN1/GluN2A(P552R) and rat GluN1/GluN2B(P553R) receptors have the EC_{50} value for both glutamate and glycine decreased in combination with an increased P_o (Ogden et al., 2017). Augmented desensitization of hGluN1/hGluN2B(V558I) receptors agrees well with results of previous experiments with chimeric receptors containing desensitizing GluN2A and non-desensitizing GluN2C subunit, as well as single-point mutations, which have identified the pre-M1 and M1 region as critical for rapid glycine- and Ca^{2+}-independent desensitization of NMDARs (Krupp et al., 1998; Villarroel et al., 1998; Thomas et al., 2006). In addition, this region has been shown to influence P_o of the NMDAR channels (Ogden et al., 2017).

We have employed computational methods to infer the structural consequences of *de novo* missense mutations based on the liganded state with the channel just prior to opening (Vyklicky et al., 2015) as deduced from the available crystal structures of the heterotetrameric GluN1/GluN2B receptor (Furukawa et al., 2005; Karakas and Furukawa, 2014; Lee et al., 2014). In the pre-open liganded state, the pre-M1 helix controls the spacing between M1 and M4 helices. It is also involved in further transmitting the mechanical signal from ligand-induced LBD reorientation through the pore-forming M3 helix to the M1 and M4 helices (**Figure 7A**). Specifically, the hGluN2B(P553) residue interacts weakly with L650 and F653 of the M3 helix. MD simulation further suggests that the hGluN2B(P553L) mutation leads to a formation of a nearly continuous M1 helix as a result of removing the helix-terminating proline residue (**Figure 7B**). The hGluN2B(V558) is mediating an interaction with surrounding hydrophobic residues of M3 helix in the liganded state. The MD simulation suggests that the hGluN2B(V558I) mutation induces stronger interaction of these residues, leading to reorientation of the pre-M1 helix from its horizontal position (**Figure 7C**). As a result, the M1/M4 interaction is weakened.

Mechanisms of hGluN2B(W607C; N615I; and V618G) Dysregulation

Cysteine accessibility to sulfhydryl reagents indicates that conserved residues hGluN2B(W607; N615; and V618) are exposed to the lumen of the NMDAR ion channel (Kuner et al., 1996). Our results show that mutations of these residues underlie multiple effects: hGluN1/hGluN2B(W607C)

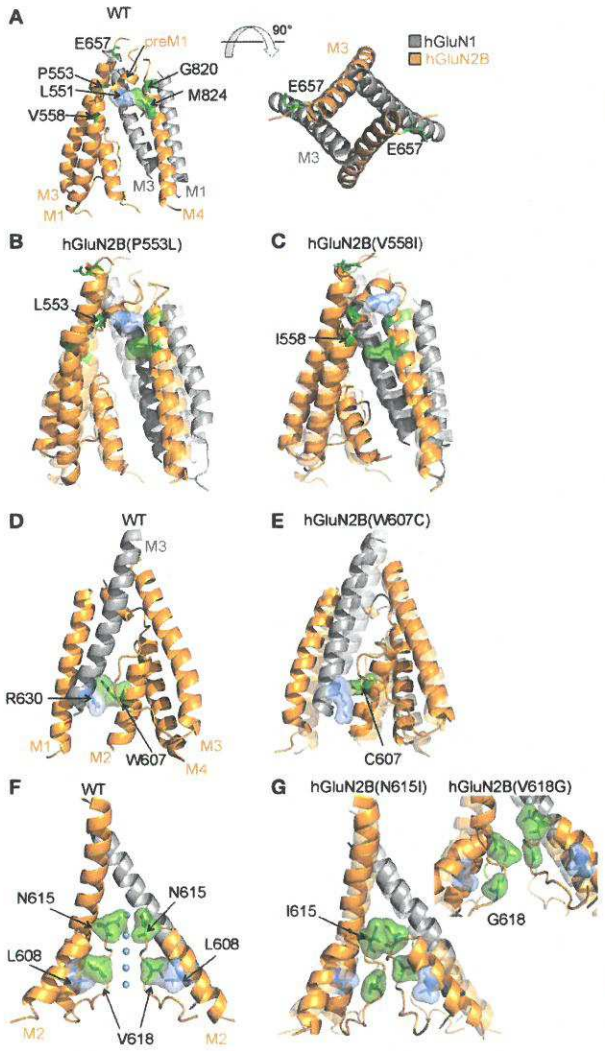

FIGURE 7 | Structural consequences of hGluN2B(P553L; V558I; W607C; N615I; and V618G) mutations. **(A)** Cartoon representation of the homology model of the membrane domain of the WT receptor built from the rat GluN1/GluN2B crystallographic data (Karakas and Furukawa, 2014; Lee et al., 2014) (GluN1 in gray; GluN2B in orange). MD simulation (of the WT receptor) indicates a van der Waals contact between hGluN2B(L551; and M824) that is important for the arrangement of the M1, pre-M1, and M3 helices. On the right, the membrane domains (M3 helices) of the NMDAR channel are viewed from the extracellular side. **(B)** Shows results of MD simulation of the hGluN1/hGluN2B(P553L) (deep colors) and WT receptor (light colors). Comparison of both superimposed models indicates that in hGluN1/hGluN2B(P553L) receptors the helical structure of the pre-M1 is prolonged and as a result contact between hGluN2B(L551; and M824) is disrupted and M1 and M4 helices repositioned. **(C)** Shows results of MD simulation of the hGluN1/hGluN2B(V558I) (deep colors) and WT receptor (light colors). The models indicate that in hGluN1/hGluN2B(V558I) receptors the helical structure of the M1 is prolonged and as a result contact between hGluN2B(L551; and M824) is disrupted and M1 and M4 helices repositioned. **(D,E)** Models of the WT and hGluN1/hGluN2B(W607C) receptors as deduced from the MD simulation. In the WT a van der Waals contact between hGluN2B(R630; and W607) is replaced by a weak contact between hGluN2B(R630) and smaller cysteine in hGluN2B(W607C). This change results

(Continued)

FIGURE 7 | in altered position of the M3 and M2 helices of the hGluN2B subunits. **(F,G)** Shows models of the WT, hGluN1/hGluN2B(N615I; and V618G) channel permeation pathway. The position of ions in the channel of the WT receptor was built from the crystallographic data of the structurally related K+ channel, pdb id 1k4c (Zhou et al., 2001). MD simulation of the WT indicates importance of a van der Waals contact between hGluN2B(L608) and hGluN2B(V618) that allow optimal orientation and precise positioning of the hGluN2B M2 loop in the channel permeation pathway. Permeant ions ($Na^+/K^+/Ca^{2+}$; indicated by blue spheres) interact with polar side chains of hGluN2B(N615) residues and backbone carbonyl groups of hGluN2B(V618). Simulation of the hGluN1/hGluN2B(N615I) receptor indicates that bulky nonpolar isoleucine residue lost the ability to coordinate the ions and occlude the permeation pathway as a result of van der Waals interaction. In addition contact of hGluN2B(L608) and hGluN2B(V618) is disrupted and as a consequence the M2 loop is destabilized with frequent transitions in between diverse conformations of the backbone. Similar destabilization effect is seen in hGluN1/hGluN2B(V618G) receptors.

receptors have a normal or moderately decreased surface expression, a decreased agonist potency, and a decreased P_o; whereas hGluN1/hGluN2B(V618G) have only a decreased P_o (**Figures 2–4**). Similarly to hGluN1/hGluN2B(W607C; and V618G) receptors, hGluN1/hGluN2B(N615I) receptors exhibit reduced responses to 1 mM glutamate (by 72%, see Supplementary Figure S2), although without an obvious change in trafficking and/or the functional parameters studied.

A characteristic feature of the hGluN1/hGluN2B(N615I) receptors was an accelerated rate of recovery from MK-801 inhibition (see Supplementary Figure S1), indicating structural differences in the ion channel pathway between WT and mutated receptors. There is compelling evidence that asparagine residues [GluN1(N616), GluN2A(N614), GluN2B(N615)] and adjacent residues including tryptophan [GluN2A(W606) or GluN2B(W607)] control permeability and block by Mg^{2+} (Williams et al., 1998) and, in addition, GluN2B(N615) controls single-channel conductance (for review see Dingledine et al., 1999). We therefore performed additional experiments to analyze Mg^{2+} block and single-channel currents. In agreement with recent data of Mullier et al. (2017), our analysis showed that Mg^{2+} sensitivity was decreased in hGluN1/hGluN2B(N615I; and W607C) receptors. Since the structural determinants of external Mg^{2+} block are similar to those governing Ca^{2+} permeability through NMDA receptor channels, it is possible that hGluN1/hGluN2B(W607C; N615I; and V618G) receptors may also have altered Ca^{2+} permeability. However, this was not possible to assess reliably due to very small current responses (Supplementary Figure S2). Similarly to Mg^{2+} block, the mean amplitude of the single-channel current was decreased for hGluN1/hGluN2B(W607C; N615I; and V618G) receptor channels.

To infer structural changes induced by mutations in the M2 segment and re-entrant loop, we used our previous model of the TMD with the vestibule open (Vyklicky et al., 2015). The ion filter as well as the lower part of M1, M3, and M4 helices are not changed significantly between the model liganded pre-open and the open state. The used model of the WT NMDAR channel is compatible with previous estimates of the minimum cross-section of the channel permeation pathway

in the conducting states: 6.0 Å (Vyklicky et al., 1988), 5.5 Å (Villarroel et al., 1995), and ~4.5 × 5.7 Å (Zarei and Dani, 1995), and within the limits proposed for the channel diameter at the level of the activated extracellular vestibule, which was estimated to be 7.3 Å (Villarroel et al., 1995) and 11 Å (Sobolevskii and Khodorov, 2002). The W607 residue is involved in a stacking interaction with hGluN1(R630) residue in the M1 helix, which contributes to a proper arrangement of the M2 helices with respect to their surroundings (**Figure 7D**). MD of mutated model structures indicates that the W607C mutation interferes with this interaction and the relative orientation of the M2 helix (**Figure 7E**). The V618 residue interacting with the L608 contributes to the correct orientation of backbone carbonyl groups within the ion filter (**Figure 7F**). Structural effects of V618G mutation suggest a loss of this orientation, possibly resulting in lower selectivity and efficiency of ion transport (**Figure 7G**). The polar side chain of the N615 residue, homologous to Q586 of AMPAR, serves as the first layer coordinating the ion to be transported. The hGluN2B(N615I) mutation will lead to a change in channel selectivity and ion permeation through the channel (**Figure 7G**).

Mechanisms of hGluN2B(S628F) Dysregulation

Reduced responses to 1 mM glutamate in HEK293T cells transfected with hGluN1/hGluN2B(S628F) receptors (Supplementary Figure S2) correlate with their reduced surface expression (**Figure 2E**, Supplementary Figure S3). hGluN2B(S628) is located at the intracellular segment of the M3 helix and is conserved within the GluN2 family (**Figure 1**). We have shown earlier that amino acid residues within the M3 helix of GluN2B subunit (W635; S645; Y646; and T647) contribute to the regulation of the surface expression of NMDARs and alter the functional properties of NMDARs (Kaniakova et al., 2012). The quality-control at intracellular points is only poorly understood, and it is a matter of speculation whether the defect in surface expression described here for hGluN1/hGluN2B(S628F) receptors involves a mechanism similar to that of other amino acid mutations in the M3 helix or other TMD regions.

Our MD simulation suggests that in the hGluN1/hGluN2B(S628F) receptors, the mutation of a polar and small serine for a larger nonpolar phenylalanine leads to steric hindrance, with the bottom part of the M1 helix altering the quaternary structure of the TMD. This may be the reason why they are offloaded from their trafficking to the cell surface (**Figures 8A,B**).

Mechanisms of hGluN2B(E657G) Dysregulation

Reduced responses to 1 mM glutamate in HEK293T cells transfected with hGluN1/hGluN2B(E657G) receptors with normal surface expression imply that the mutation introduced a severe functional defect (Supplementary Figure S2, **Figure 2E**). Glutamate residue hGluN2B(E657) is conserved within the GluN2, GluA, and GluK family and is part of the linker that connects the LBD and M3 helices. Rearrangement of M3 helices

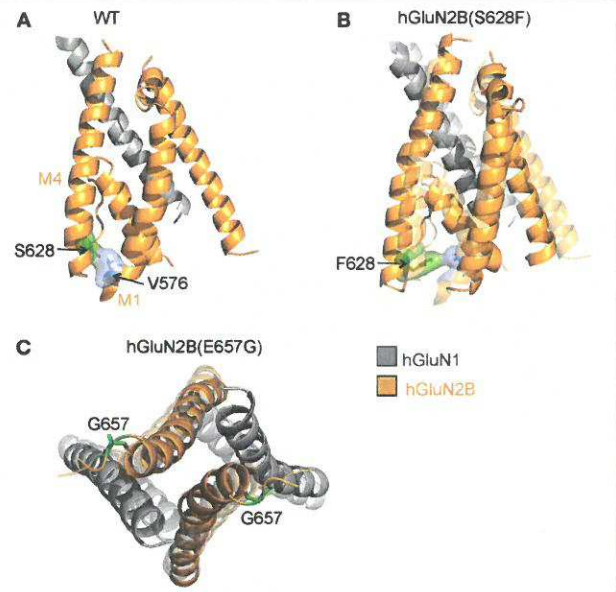

FIGURE 8 | Structural consequences of hGluN2B(S628F; and E657G) mutations. **(A)** Cartoon representation of the homology model of the membrane domain of the WT receptor built from the rat GluN1/GluN2B crystallographic data (Karakas and Furukawa, 2014; Lee et al., 2014) (GluN1 in gray; GluN2B in orange). MD simulation of the WT receptor indicates a series of inter-helical zipper-like contacts spanning along the M1 and M4 helices. The contact between hGluN2B(S628) and hGluN2B(V576) is highlighted. **(B)** According to the MD simulation the hGluN2B(S628F) substitution leads to larger separation of M1 and M4 helices. Contrary to an expected stronger van der Waals interaction with the hGluN2B(V576) across helices the steric effect of larger hydrophobic phenylalanine residue leads to rearrangement of residues along the M4 helix and formation of a chain of van der Waals stabilized M4 residues. **(C)** The MD simulation of hGluN2B(E657G) mutation suggests closing of the ion channel due to a loss of specific interactions along the TMD-LBD hGluN2B linker.

in the activated conformation of the receptor makes the central cavity of the channel accessible to ions, therefore implying a crucial role of the M3-S2 linkers in channel opening (Sobolevsky et al., 2004). Mutations in this region lead to profound alterations of the receptor channel function characterized by diminished P_o and altered transduction of agonist activation to channel opening (Kazi et al., 2014). Missing experimental electron density data in available crystal structures (Karakas and Furukawa, 2014; Lee et al., 2014) does not allow the localization of residues in the linker regions and related structural information is mostly missing, we therefore decided to explore linker structures computationally. Our data indicate that the overall effect of glycine substitution hGluN2B(E657G) on NMDAR gating can be explained by an interaction of specific residues at a site located in the proximity of the M3 helices (**Figures 7A, 8C**).

Mechanisms of hGluN2B(G820E; G820A; M824R; and L825V) Dysregulation

Reduced responses to 1 mM glutamate observed in HEK293T cells transfected with genes encoding for hGluN1 and hGluN2B(G820A) subunits and a complete loss of responses in

hGluN1/hGluN2B(G820E; and M824R) receptors are not due to altered surface expression since this was normal or even increased (**Figure 2E**). Small currents in hGluN1/hGluN2B(G820A) receptors precluded detailed functional examination. In contrast, responses to 1 mM glutamate in cells transfected with genes encoding for hGluN1 and hGluN2B(L825V) subunits were not significantly different from those observed in the WT although they had reduced P_o by 86% compared to the WT receptors.

Structurally conserved residues hGluN2B(G820, M824, and L825) (**Figure 1**) are located in mutual proximity in the M4 helix. Several lines of evidence indicate that M1 and M4 helices are located at the periphery of the TMD and seem to have a modulatory role in channel opening and closing, which is primarily mediated by M3 helices that form the central cavity of the channel in the activated receptor (Villarroel et al., 1998; Sobolevsky et al., 2004; Ogden and Traynelis, 2013; Karakas and Furukawa, 2014).The hGluN2B(L825) residue interacts with the F639 from the M1 helix of hGluN1 in the liganded state (**Figure 9A**). The hGluN2B(L825V) mutation leads to a weaker interaction with the hGluN1(F639), although structural effects are inconclusive (**Figure 9B**). MD revealed that hGluN2B(G820) serves as the last residue in the M4 helix, thus allowing the necessary extension of the preceding linker in response to the LBD reorientation. The hGluN2B(G820E; and G820A) mutations remain in the helical context and their side chains interact with the pre-M1 helix, shifting it from its horizontal position and changing the relative positions of M1 and M4 helices (**Figures 9C,D**). In the liganded state, the hGluN2B(M824) residue is involved in an interaction with hGluN2B(L551) of the pre-M1 helix (**Figure 7A**). As a consequence of the hGluN2B(M824R) mutation, the pre-M1 interaction is not formed (**Figure 9E**); this leads to an altered relative position of M1 and M4 helices, which in turn results in inefficient propagation of the mechanical signal from the LBD.

Pharmacology of Mutated Receptors

Therapeutic strategies for the development of new effective drugs for rectifying loss-of-function variants associated with diminution of the receptor P_o may encompass PE-S and its derivatives, since these compounds have a positive allosteric effect that is specifically mediated by the increase in the receptor P_o (Horak et al., 2004; Korinek et al., 2011). Both an endogenously occurring neurosteroid PE-S (Wu et al., 1991;

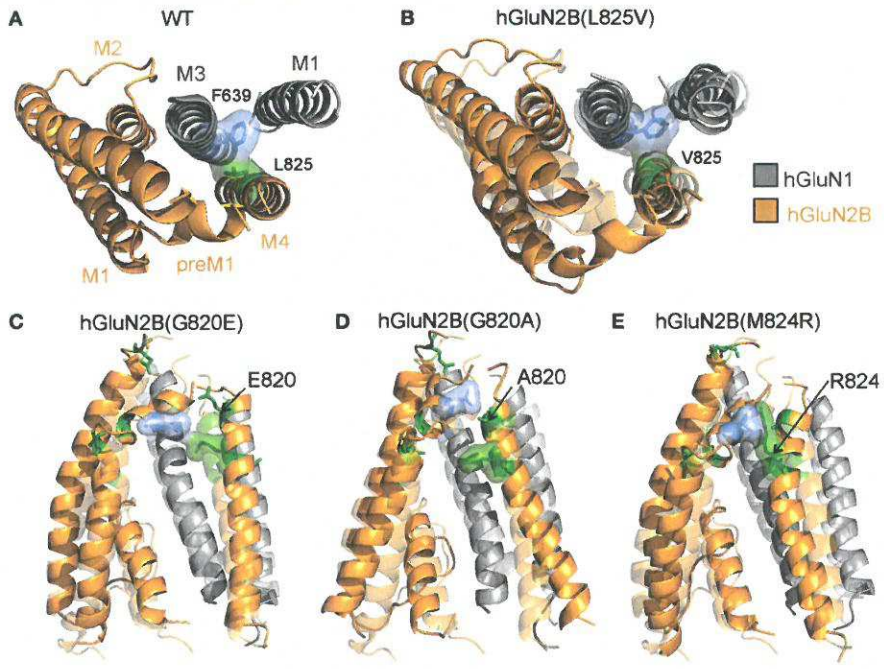

FIGURE 9 | Structural consequences of hGluN2B(L825V; G820E; G820A; and M824R) mutations. **(A)** Cartoon representation of the homology model of the membrane domain of the WT receptor built from the rat GluN1/GluN2B crystallographic data (Karakas and Furukawa, 2014; Lee et al., 2014) (GluN1 in gray; GluN2B in orange). MD simulation of the WT receptor identified a van der Waals contact between hGluN1(F639) and hGluN2B(L825) involved in interaction of hGluN1 M3 helix with the hGluN2B M4 helix**. (B)** The hGluN2B(L825V) substitution for a smaller aliphatic residue leads to weaker van der Waals interaction with the hGluN1(F639) resulting in a slight separation of the interacting helices. However, the structural effects are inconclusive. **(C,D)** MD revealed that hGluN2B(G820) serves as the last residue in the M4 helix thus allowing the necessary extension of the preceding linker in response to the LBD reorientation. The hGluN2B(G820A; and G820E) mutations remain in the helical context and the introduced side chains interact with residues from the pre-M1 helix. This changes the pre-M1 horizontal position as well as relative positions of M1 and M4 helices. **(E)** The hGluN2B(M824) residue is involved in an interaction with hGluN2B(L551) of the pre-M1 helix in the liganded state. The hGluN2B(M824R) mutation prevents the pre-M1 interaction and leads to altered relative position of M1 and M4 helices and consequently to inefficient propagation of the mechanical signal from the LBD.

Bowlby, 1993) and its more potent synthetic analog AND-hSuc (Krausova et al., 2018) were approximately as effective at WT as at the hGluN1/hGluN2B(V558I; W607C; V618G; and G820A) receptors. Interestingly, both steroids potentiated the amplitude of tonic and synaptic-like responses more profoundly when studied at hGluN1/hGluN2B(L825V) receptors, indicating their prospective use in personalized therapies. It is likely that the augmented potentiating effect for PE-S is not specifically associated with residues at the TMD, since similar increases have been recently shown for receptors mutated in the LBD of the GluN2A subunit (V685G; and D731N) (Swanger et al., 2016).

Functional defects described here in the NMDAR apply for cases in which both alleles in a patient were mutated at exactly the same site. This is expected to be rare, in contrast to heterozygous individuals, who are much more likely to carry only one mutated allele. In this case, the expected genotypic ratio predicts that each neuron will contain 25% of WT receptors, 50% of receptors composed of one hGluN2B subunit mutated and one non-mutated, and 25% of receptors comprised of both hGluN2B subunits mutated.

To build a conception of the degree of the NMDAR defect, we may use as an example the mutation-induced decrease in the receptor P_o (P_o = 10% for the WT and P_o = 1% for receptors with both hGluN2B subunits mutated). Based on the Mendelian laws of inheritance and the law of dominance, we may predict that the overall activity of NMDARs will be diminished, depending on whether the mutation is recessive, independent, or dominant, to 77.5, 55, and 32.5%, respectively, of the activity in the healthy subjects. These calculations indicate that for a full pharmacological rectification of the NMDAR defect, a potentiating effect of 22.5, 45, and 67.5% would be required. Since most neurons express more than one type of GluN2/GluN3 subunits (Monyer et al., 1994), the expected rectifying potentiation effect may be even smaller. However, further studies are required to understand how the degree of NMDAR hypofunction is linked to various clinical symptoms.

AUTHOR CONTRIBUTIONS

VV and LV designed the experiments; VV, BKr, BKy, ML, TS, and MK performed electrophysiological experiments; BKr, SD, and MH performed trafficking experiments; VV, BKr, and LV analyzed the data; JC performed molecular modeling; HC and EK synthetized the steroids; LV wrote the paper.

FUNDING

This work was supported by the Czech Science Foundation: 17-02300S (LV), 16-03913Y (TS); Technology Agency of the Czech Republic: TE01020028 (LV); from Ministry of Health of the Czech Republic: NV15-29370A (LV); ERDF/ESF project PharmaBrain (No. CZ.02.1.01/0.0/0.0/16_025/0007444); Grant Agency of Charles University (GAUK): 880216 (ML), 468217 (SD); Research Project of the AS CR RVO: 67985823; MSM200111601 and BIOCEV–Biotechnology and Biomedicine Centre of Academy of Sciences and Charles University in Vestec, project supported from European Regional Development Fund.

ACKNOWLEDGMENTS

We thank M. Kuntosova for excellent technical assistance, Nikola Bednarova for preparation of mutant receptors, and Kristyna Skrenkova for preparation of YFP-hGluN1 construct.

SUPPLEMENTARY MATERIAL

The Supplementary Material for this article can be found online at: https://www.frontiersin.org/articles/10.3389/fnmol.2018.00110/full#supplementary-material

REFERENCES

Abdrachmanova, G., Teisinger, J., and Vyklicky, L. Jr. (2002). Axotomy-induced changes in the properties of NMDA receptor channels in rat spinal cord motoneurons. *J. Physiol.* 538(Pt 1), 53–63. doi: 10.1113/jphysiol.2001.012794

Adams, D. R., Yuan, H., Holyoak, T., Arajs, K. H., Hakimi, P., Markello, T. C., et al. (2014). Three rare diseases in one Sib pair: RAI1, PCK1, GRIN2B mutations associated with Smith-Magenis Syndrome, cytosolic PEPCK deficiency and NMDA receptor glutamate insensitivity. *Mol. Genet. Metab.* 113, 161–170. doi: 10.1016/j.ymgme.2014.04.001

Akazawa, C., Shigemoto, R., Bessho, Y., Nakanishi, S., and Mizuno, N. (1994). Differential expression of five N-methyl-D-aspartate receptor subunit mRNAs in the cerebellum of developing and adult rats. *J. Comp. Neurol.* 347, 150–160. doi: 10.1002/cne.903470112

Awadalla, P., Gauthier, J., Myers, R. A., Casals, F., Hamdan, F. F., Griffing, A. R., et al. (2010). Direct measure of the de novo mutation rate in autism and schizophrenia cohorts. *Am. J. Hum. Genet.* 87, 316–324. doi: 10.1016/j.ajhg.2010.07.019

Bowlby, M. R. (1993). Pregnenolone sulfate potentiation of N-methyl-D-aspartate receptor channels in hippocampal neurons. *Mol. Pharmacol.* 43, 813–819.

Brooks, B. R., Brooks, C. L. III, Mackerell, A. D. Jr., Nilsson, L., Petrella, R. J., Roux, B., et al. (2009). CHARMM: the biomolecular simulation program. *J. Comput. Chem.* 30, 1545–1614. doi: 10.1002/jcc.21287

Burnashev, N., and Szepetowski, P. (2015). NMDA receptor subunit mutations in neurodevelopmental disorders. *Curr. Opin. Pharmacol.* 20, 73–82. doi: 10.1016/j.coph.2014.11.008

Cais, O., Sedlacek, M., Horak, M., Dittert, I., and Vyklicky, L. Jr. (2008). Temperature dependence of NR1/NR2B NMDA receptor channels. *Neuroscience* 151, 428–438. doi: 10.1016/j.neuroscience.2007.11.002

Chen, N., Luo, T., and Raymond, L. A. (1999). Subtype-dependence of NMDA receptor channel open probability. *J. Neurosci.* 19, 6844–6854.

Chen, W., Shieh, C., Swanger, S. A., Tankovic, A., Au, M., McGuire, M., et al. (2017). GRIN1 mutation associated with intellectual disability alters NMDA receptor trafficking and function. *J. Hum. Genet.* 62, 589–597. doi: 10.1038/jhg.2017.19

Choi, D. W. (1987). Ionic dependence of glutamate neurotoxicity. *J. Neurosci.* 7, 369–379.

Cohen, S., and Greenberg, M. E. (2008). Communication between the synapse and the nucleus in neuronal development, plasticity, and disease. *Annu. Rev. Cell Dev. Biol.* 24, 183–209. doi: 10.1146/annurev.cellbio.24.110707.175235

Colquhoun, D., and Sakmann, B. (1985). Fast events in single-channel currents activated by acetylcholine and its analogues at the frog muscle end-plate. *J. Physiol. Lond.* 369, 501–557. doi: 10.1113/jphysiol.1985.sp015912

de Ligt, J., Willemsen, M. H., van Bon, B. W., Kleefstra, T., Yntema, H. G., Kroes, T., et al. (2012). Diagnostic exome sequencing in persons with severe intellectual disability. *N. Engl. J. Med.* 367, 1921–1929. doi: 10.1056/NEJMoa1206524

Dingledine, R., Borges, K., Bowie, D., and Traynelis, S. F. (1999). The glutamate receptor ion channels. *Pharmacol. Rev.* 51, 7–61.

Furukawa, H., Singh, S. K., Mancusso, R., and Gouaux, E. (2005). Subunit arrangement and function in NMDA receptors. *Nature* 438, 185–192. doi: 10.1038/nature04089

Hall, B. J., Ripley, B., and Ghosh, A. (2007). NR2B signaling regulates the development of synaptic AMPA receptor current. *J. Neurosci.* 27, 13446–13456. doi: 10.1523/JNEUROSCI.3793-07.2007

Hamdan, F. F., Srour, M., Capo-Chichi, J. M., Daoud, H., Nassif, C., Patry, L., et al. (2014). De novo mutations in moderate or severe intellectual disability. *PLoS Genet.* 10:e1004772. doi: 10.1371/journal.pgen.1004772

Hedegaard, M., Hansen, K. B., Andersen, K. T., Brauner-Osborne, H., and Traynelis, S. F. (2012). Molecular pharmacology of human NMDA receptors. *Neurochem. Int.* 61, 601–609. doi: 10.1016/j.neuint.2011.11.016

Horak, M., Chang, K., and Wenthold, R. J. (2008). Masking of the endoplasmic reticulum retention signals during assembly of the NMDA receptor. *J. Neurosci.* 28, 3500–3509. doi: 10.1523/JNEUROSCI.5239-07.2008

Horak, M., Vlcek, K., Chodounska, H., and Vyklicky, L. Jr. (2006). Subtype-dependence of N-methyl-d-aspartate receptor modulation by pregnenolone sulfate. *Neuroscience* 137, 93–102. doi: 10.1016/j.neuroscience.2005.08.058

Horak, M., Vlcek, K., Petrovic, M., Chodounska, H., and Vyklicky, L. Jr. (2004). Molecular mechanism of pregnenolone sulfate action at NR1/NR2B receptors. *J. Neurosci.* 24, 10318–10325. doi: 10.1523/JNEUROSCI.2099-04.2004

Hu, C., Chen, W., Myers, S. J., Yuan, H., and Traynelis, S. F. (2016). Human GRIN2B variants in neurodevelopmental disorders. *J. Pharmacol. Sci.* 132, 115–121. doi: 10.1016/j.jphs.2016.10.002

Huettner, J. E., and Bean, B. P. (1988). Block of N-methyl-D-aspartate-activated current by the anticonvulsant MK-801: selective binding to open channels. *Proc. Natl. Acad. Sci. U.S.A.* 85, 1307–1311. doi: 10.1073/pnas.85.4.1307

Huganir, R. L., and Nicoll, R. A. (2013). AMPARs and synaptic plasticity: the last 25 years. *Neuron* 80, 704–717. doi: 10.1016/j.neuron.2013.10.025

Jahr, C. E. (1992). High probability opening of NMDA receptor channels by L-glutamate. *Science* 255, 470–472.

Jo, S., Kim, T., Iyer, V. G., and Im, W. (2008). CHARMM-GUI: a web-based graphical user interface for CHARMM. *J. Comput. Chem.* 29, 1859–1865. doi: 10.1002/jcc.20945

Kaniakova, M., Krausova, B., Vyklicky, V., Korinek, M., Lichnerova, K., Vyklicky, L., et al. (2012). Key amino acid residues within the third membrane domains of NR1 and NR2 subunits contribute to the regulation of the surface delivery of N-methyl-D-aspartate receptors. *J. Biol. Chem.* 287, 26423–26434. doi: 10.1074/jbc.M112.339085

Karakas, E., and Furukawa, H. (2014). Crystal structure of a heterotetrameric NMDA receptor ion channel. *Science* 344, 992–997. doi: 10.1126/science.1251915

Kazi, R., Dai, J., Sweeney, C., Zhou, H. X., and Wollmuth, L. P. (2014). Mechanical coupling maintains the fidelity of NMDA receptor-mediated currents. *Nat. Neurosci.* 17, 914–922. doi: 10.1038/nn.3724

Korinek, M., Kapras, V., Vyklicky, V., Adamusova, E., Borovska, J., Vales, K., et al. (2011). Neurosteroid modulation of N-methyl-D-aspartate receptors: molecular mechanism and behavioral effects. *Steroids* 76, 1409–1418. doi: 10.1016/j.steroids.2011.09.002

Krausova, B., Slavikova, B., Nekardova, M., Hubalkova, P., Vyklicky, V., Chodounska, H., et al. (2018). Positive modulators of N-Methyl-D-aspartate receptor: structure-activity relationship study on steroidal 3-hemiesters. *J. Med. Chem.*

Krupp, J. J., Vissel, B., Heinemann, S. F., and Westbrook, G. L. (1998). N-terminal domains in the NR2 subunit control desensitization of NMDA receptors. *Neuron* 20, 317–327. doi: 10.1016/S0896-6273(00)80459-6

Kuner, T., Wollmuth, L. P., Karlin, A., Seeburg, P. H., and Sakmann, B. (1996). Structure of the NMDA receptor channel M2 segment inferred from the accessibility of substituted cysteines. *Neuron* 17, 343–352. doi: 10.1016/S0896-6273(00)80165-8

Kupper, J., Ascher, P., and Neyton, J. (1996). Probing the pore region of recombinant N-methyl-D-aspartate channels using external and internal magnesium block. *Proc. Natl. Acad. Sci. U.S.A.* 93, 8648–8653. doi: 10.1073/pnas.93.16.8648

Kutsuwada, T., Sakimura, K., Manabe, T., Takayama, C., Katakura, N., Kushiya, E., et al. (1996). Impairment of suckling response, trigeminal neuronal pattern formation, and hippocampal LTD in NMDA receptor epsilon 2 subunit mutant mice. *Neuron* 16, 333–344. doi: 10.1016/S0896-6273(00)80051-3

Lazaridis, T. (2003). Effective energy function for proteins in lipid membranes. *Proteins* 52, 176–192. doi: 10.1002/prot.10410

Lee, C. H., Lü, W., Michel, J. C., Goehring, A., Du, J., Song, X., et al. (2014). NMDA receptor structures reveal subunit arrangement and pore architecture. *Nature* 511, 191–197. doi: 10.1038/nature13548

Lek, M., Karczewski, K. J., Minikel, E. V., Samocha, K. E., Banks, E., Fennell, T., et al. (2016). Analysis of protein-coding genetic variation in 60,706 humans. *Nature* 536, 285–291. doi: 10.1038/nature19057

Lelieveld, S. H., Reijnders, M. R., Pfundt, R., Yntema, H. G., Kamsteeg, E. J., de Vries, P., et al. (2016). Meta-analysis of 2,104 trios provides support for 10 new genes for intellectual disability. *Nat. Neurosci.* 19, 1194–1196. doi: 10.1038/nn.4352

Lemke, J. R., Hendrickx, R., Geider, K., Laube, B., Schwake, M., Harvey, R. J., et al. (2014). GRIN2B mutations in West syndrome and intellectual disability with focal epilepsy. *Ann. Neurol.* 75, 147–154. doi: 10.1002/ana.24073

Lester, R. A., Clements, J. D., Westbrook, G. L., and Jahr, C. E. (1990). Channel kinetics determine the time course of NMDA receptor-mediated synaptic currents. *Nature* 346, 565–567.

Lichnerova, K., Kaniakova, M., Skrenkova, K., Vyklicky, L., and Horak, M. (2014). Distinct regions within the GluN2C subunit regulate the surface delivery of NMDA receptors. *Front. Cell. Neurosci.* 8:375. doi: 10.3389/fncel.2014.00375

Lynch, M. A. (2004). Long-term potentiation and memory. *Physiol. Rev.* 84, 87–136. doi: 10.1152/physrev.00014.2003

Mcrae, J. F., Clayton, S., Fitzgerald, T. W., Kaplanis, J., Prigmore, E., Rajan, D., et al. (2017). Prevalence and architecture of de novo mutations in developmental disorders. *Nature* 542, 433–438. doi: 10.1038/nature21062

Mendes, P. (1993). GEPASI: a software package for modelling the dynamics, steady states and control of biochemical and other systems. *Comput. Appl. Biosci.* 9, 563–571. doi: 10.1093/bioinformatics/9.5.563

Mendes, P. (1997). Biochemistry by numbers: simulation of biochemical pathways with Gepasi 3. *Trends Biochem. Sci.* 22, 361–363. doi: 10.1016/S0968-0004(97)01103-1

Mendes, P., and Kell, D. (1998). Non-linear optimization of biochemical pathways: applications to metabolic engineering and parameter estimation. *Bioinformatics* 14, 869–883. doi: 10.1093/bioinformatics/14.10.869

Monyer, H., Burnashev, N., Laurie, D. J., Sakmann, B., and Seeburg, P. H. (1994). Developmental and regional expression in the rat brain and functional properties of four NMDA receptors. *Neuron* 12, 529–540. doi: 10.1016/0896-6273(94)90210-0

Mullier, B., Wolff, C., Sands, Z. A., Ghisdal, P., Muglia, P., Kaminski, R. M., et al. (2017). GRIN2B gain of function mutations are sensitive to radiprodil, a negative allosteric modulator of GluN2B-containing NMDA receptors. *Neuropharmacology* 123, 322–331. doi: 10.1016/j.neuropharm.2017.05.017

Ogden, K. K., Chen, W., Swanger, S. A., McDaniel, M. J., Fan, L. Z., Hu, C., et al. (2017). Molecular mechanism of disease-associated mutations in the Pre-M1 Helix of NMDA receptors and potential rescue pharmacology. *PLoS Genet.* 13:e1006536. doi: 10.1371/journal.pgen.1006536

Ogden, K. K., and Traynelis, S. F. (2013). Contribution of the M1 transmembrane helix and pre-M1 region to positive allosteric modulation and gating of N-methyl-D-aspartate receptors. *Mol. Pharmacol.* 83, 1045–1056. doi: 10.1124/mol.113.085209

Okabe, S., Miwa, A., and Okado, H. (1999). Alternative splicing of the C-terminal domain regulates cell surface expression of the NMDA receptor NR1 subunit. *J. Neurosci.* 19, 7781–7792.

Olney, J. W. (1969). Brain lesions, obesity, and other disturbances in mice treated with monosodium glutamate. *Science* 164, 719–721.

Parsons, M. P., and Raymond, L. A. (2014). Extrasynaptic NMDA receptor involvement in central nervous system disorders. *Neuron* 82, 279–293. doi: 10.1016/j.neuron.2014.03.030

Platzer, K., Yuan, H., Schütz, H., Winschel, A., Chen, W., Hu, C., et al. (2017). GRIN2B encephalopathy: novel findings on phenotype, variant clustering, functional consequences and treatment aspects. *J. Med. Genet.* 54, 460–470. doi: 10.1136/jmedgenet-2016-104509

Rosenmund, C., Feltz, A., and Westbrook, G. L. (1995). Synaptic NMDA receptor channels have a low open probability. *J. Neurosci.* 15, 2788–2795.

Sali, A., and Blundell, T. L. (1993). Comparative protein modelling by satisfaction of spatial restraints. *J. Mol. Biol.* 234, 779–815. doi: 10.1006/jmbi.1993.1626

Sobolevskii, A. I., and Khodorov, B. I. (2002). Blocker studies of the functional architecture of the NMDA receptor channel. *Neurosci. Behav. Physiol.* 32, 157–171. doi: 10.1023/A:1013927409034

Sobolevsky, A. I., Rosconi, M. P., and Gouaux, E. (2009). X-ray structure, symmetry and mechanism of an AMPA-subtype glutamate receptor. *Nature* 462, 745–756. doi: 10.1038/nature08624

Sobolevsky, A. I., Yelshansky, M. V., and Wollmuth, L. P. (2004). The outer pore of the glutamate receptor channel has 2-fold rotational symmetry. *Neuron* 41, 367–378. doi: 10.1016/S0896-6273(04)00008-X

Soto, D., Altafaj, X., Sindreu, C., and Bayes, A. (2014). Glutamate receptor mutations in psychiatric and neurodevelopmental disorders. *Commun. Integr. Biol.* 7:e27887. doi: 10.4161/cib.27887

Standley, S., Roche, K. W., McCallum, J., Sans, N., and Wenthold, R. J. (2000). PDZ domain suppression of an ER retention signal in NMDA receptor NR1 splice variants. *Neuron* 28, 887–898. doi: 10.1016/S0896-6273(00)00161-6

Swanger, S. A., Chen, W., Wells, G., Burger, P. B., Tankovic, A., Bhattacharya, S., et al. (2016). Mechanistic Insight into NMDA Receptor Dysregulation by Rare Variants in the GluN2A and GluN2B Agonist Binding Domains. *Am. J. Hum. Genet.* 99, 1261–1280. doi: 10.1016/j.ajhg.2016.10.002

Tarabeux, J., Kebir, O., Gauthier, J., Hamdan, F. F., Xiong, L., Piton, A., et al. (2011). Rare mutations in N-methyl-D-aspartate glutamate receptors in autism spectrum disorders and schizophrenia. *Transl. Psychiatr.* 1:e55. doi: 10.1038/tp.2011.52

Thomas, C. G., Krupp, J. J., Bagley, E. E., Bauzon, R., Heinemann, S. F., Vissel, B., et al. (2006). Probing N-methyl-D-aspartate receptor desensitization with the substituted-cysteine accessibility method. *Mol. Pharmacol.* 69, 1296–1303. doi: 10.1124/mol.105.017350

Traynelis, S. F., Wollmuth, L. P., McBain, C. J., Menniti, F. S., Vance, K. M., Ogden, K. K., et al. (2010). Glutamate receptor ion channels: structure, regulation, and function. *Pharmacol. Rev.* 62, 405–496. doi: 10.1124/pr.109.002451

Turecek, R., Vlcek, K., Petrovic, M., Horak, M., Vlachova, V., and Vyklicky, L. Jr. (2004). Intracellular spermine decreases open probability ofN-methyl-d-aspartate receptor channels. *Neuroscience* 125, 879–887. doi: 10.1016/j.neuroscience.2004.03.003

Villarroel, A., Burnashev, N., and Sakmann, B. (1995). Dimensions of the narrow portion of a recombinant NMDA receptor channel. *Biophys. J.* 68, 866–875. doi: 10.1016/S0006-3495(95)80263-8

Villarroel, A., Regalado, M. P., and Lerma, J. (1998). Glycine-independent NMDA receptor desensitization: localization of structural determinants. *Neuron* 20, 329–339. doi: 10.1016/S0896-6273(00)80460-2

Vyklicky, L. Jr., Krusek, J., and Edwards, C. (1988). Differences in the pore sizes of the N-methyl-D-aspartate and kainate cation channels. *Neurosci. Lett.* 89, 313–318. doi: 10.1016/0304-3940(88)90545-9

Vyklicky, V., Korinek, M., Balik, A., Smejkalova, T., Krausova, B., and Vyklicky, L. (2016) "Analysis of whole-cell NMDA receptor currents," in *Ionotropic Glutamate Receptor Technologies*. Neuromethods, Vol. 106, G. Popescu (New York, NY: Humana Press), 205–219.

Vyklicky, V., Krausova, B., Cerny, J., Balik, A., Zapotocky, M., Novotny, M., et al. (2015). Block of NMDA receptor channels by endogenous neurosteroids: implications for the agonist induced conformational states of the channel vestibule. *Sci. Rep.* 5:10935. doi: 10.1038/srep10935

Webb, B., and Sali, A. (2014). Comparative Protein Structure Modeling Using MODELLER. *Curr. Protoc. Bioinformatics* 47, Chapter 5: Unit-5.6 1–32. doi: 10.1002/0471250953.bi0506s47

Weiss, J. N. (1997). The Hill equation revisited: uses and misuses. *FASEB J.* 11, 835–841. doi: 10.1096/fasebj.11.11.9285481

Williams, K., Pahk, A. J., Kashiwagi, K., Masuko, T., Nguyen, N. D., and Igarashi, K. (1998). The selectivity filter of the N-methyl-D-aspartate receptor: a tryptophan residue controls block and permeation of Mg^{2+}. *Mol. Pharmacol.* 53, 933–941.

Wu, F. S., Gibbs, T. T., and Farb, D. H. (1991). Pregnenolone sulfate: a positive allosteric modulator at the N-methyl-D- aspartate receptor. *Mol. Pharmacol.* 40, 333–336.

Yavarna, T., Al-Dewik, N., Al-Mureikhi, M., Ali, R., Al-Mesaifri, F., Mahmoud, L., et al. (2015). High diagnostic yield of clinical exome sequencing in Middle Eastern patients with Mendelian disorders. *Hum. Genet.* 134, 967–980. doi: 10.1007/s00439-015-1575-0

Yuan, H., Hansen, K. B., Zhang, J., Pierson, T. M., Markello, T. C., Fajardo, K. V., et al. (2014). Functional analysis of a de novo GRIN2A missense mutation associated with early-onset epileptic encephalopathy. *Nat. Commun.* 5:3251. doi: 10.1038/ncomms4251

Zarei, M. M., and Dani, J. A. (1995). Structural basis for explaining open-channel blockade of the NMDA receptor. *J. Neurosci.* 15, 1446–1454.

Zhou, Y., Morais-Cabral, J. H., Kaufman, A., and MacKinnon, R. (2001). Chemistry of ion coordination and hydration revealed by a K+ channel-Fab complex at 2.0 A resolution. *Nature* 414, 43–48. doi: 10.1038/35102009

Zhu, X., Petrovski, S., Xie, P., Ruzzo, E. K., Lu, Y. F., McSweeney, K. M., et al. (2015). Whole-exome sequencing in undiagnosed genetic diseases: interpreting 119 trios. *Genet. Med.* 17, 774–781. doi: 10.1038/gim.2014.191

Conflict of Interest Statement: The authors declare that the research was conducted in the absence of any commercial or financial relationships that could be construed as a potential conflict of interest.

Journal of Medicinal Chemistry

Article

pubs.acs.org/jmc

Neurosteroid-like Inhibitors of *N*-Methyl-D-aspartate Receptor: Substituted 2-Sulfates and 2-Hemisuccinates of Perhydrophenanthrene

Barbora Slavikova,[†] Hana Chodounska,[†] Michaela Nekardova,[†,§,∥] Vojtech Vyklicky,[‡] Marek Ladislav,[‡] Pavla Hubalkova,[‡] Barbora Krausova,[‡] Ladislav Vyklicky,[‡] and Eva Kudova*[,†]

[†]Institute of Organic Chemistry and Biochemistry, Academy of Sciences of the Czech Republic, v.v.i., Flemingovo nam. 2, Dejvice, Prague 6, 16610, Czech Republic

[‡]Institute of Physiology CAS, Videnska 1083, 142 20 Prague 4, Czech Republic

[§]Faculty of Mathematics and Physics, Charles University in Prague, Ke Karlovu 3, Prague 2, 121 16, Czech Republic

Supporting Information

ABSTRACT: *N*-Methyl-D-aspartate receptors (NMDARs) display a critical role in various diseases of the central nervous system. The activity of NMDARs can be modulated by neurosteroids. Herein, we report a structure−activity relationship study for perhydrophenanthrene analogues possessing a framework that mimics the steroidal ring system. This study comprises the design, synthesis, and assessment of the biological activity of a library of perhydrophenanthrene 2-sulfates and 2-hemisuccinates (**1**−**10**). Their ability to modulate NMDAR-induced currents was tested on recombinant GluN1/GluN2B receptors. Our results demonstrate that such structural optimization leads to compounds that are inhibitors of NMDARs. Notably, compound **9** (IC_{50} = 15.6 μM) was assessed as a more potent inhibitor of NMDAR-induced currents than the known endogenous neurosteroid, pregnanolone sulfate (IC_{50} = 24.6 μM).

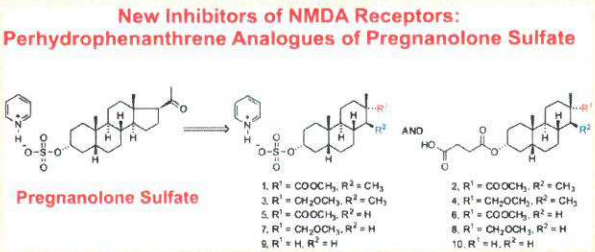

INTRODUCTION

N-Methyl-D-aspartate receptors (NMDARs) are glutamate-gated, calcium-permeable ion channels involved in excitatory synaptic transmission and synaptic plasticity.[1] The design of new NMDAR modulators could lead to the development of pharmaceutically attractive, druglike compounds, as a broad variety central nervous system diseases (neurodegeneration, ischemia, traumatic brain injury, etc.)[2−4] have been associated with glutamate induced excitotoxicity under pathological conditions, a specific form of neuronal cell death caused by overactivation of NMDARs.

Neurosteroids have both positive and negative effects on NMDARs, and such modulatory effects play a role in many physiological processes. Our previous studies of neurosteroid effect on NMDAR modulation demonstrated that these molecules do have neuroprotective effect in animal models of various indications.[5−7] In addition, we have shown that particular structural modifications afford neurosteroids that have a higher preference for tonically activated NMDARs than for NMDARs activated during synaptic transmission.[8] Finally, we have identified the molecular basis of the use-dependent and voltage-independent inhibitory effect of neurosteroids on NMDAR responses.[9] The site of action is located at the extracellular vestibule of the receptor's ion channel pore and is accessible after receptor activation.

As a part of our continuing interest in the structure−activity relationship (SAR) study of neurosteroid modulators of NMDARs, we recently reported[10] a new, nonpolar structural modification at positions C-17 and C-20 of the steroidal skeleton D-ring (methyl, ethyl, 17-methylene, 20-ethylene, etc.). Compounds with such modifications were shown to be potent modulators of NMDAR-induced currents (e.g., 5β-androstane-3α-yl 3-sulfate, Figure 1b, IC_{50} = 1.2 μM). Moreover, these compounds were established as more potent inhibitors of NMDAR-induced currents than the known, endogenous NMDAR inhibitor, pregnanolone sulfate[11] (20-oxo-5β-pregnan-3α-yl sulfate, IC_{50} = 24.6 μM; Figure 1).

In order to extend our previous study[10] that demonstrated the expandable role of C-17 acetyl moiety, we wanted to evaluate the critical role of the steroidal D-ring (Figure 1). Therefore, we have synthesized a series of fully saturated phenanthrenes (Figure 2) that have not been previously reported. The two major steroidal structural features necessary for maintaining inhibitory biological activity on NMDARs are retention of the 5β-stereochemistry and axial 3α-configuration.[11] In addition, the stereochemistry at steroidal positions C-8 and C-9 was maintained. As such, these new perhydrophenanthrene analogues (**1**−**10**) closely mimic steroidal ABC ring arrangement.

The inhibitory effect of neurosteroids on NMDARs is also associated with the presence of a positively or negatively charged

Received: January 16, 2016
Published: April 11, 2016

DOI: 10.1021/acs.jmedchem.6b00079
J. Med. Chem. 2016, 59, 4724−4739

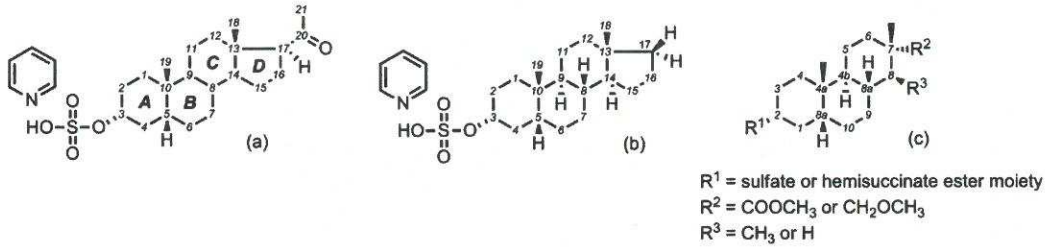

Figure 1. Structures of (a) pregnanolone sulfate, (b) 5β-androstane-3α-yl 3-sulfate, and (c) perhydrophenanthrene 2-sulfate or 2-hemisuccinate with their ring numbering system.

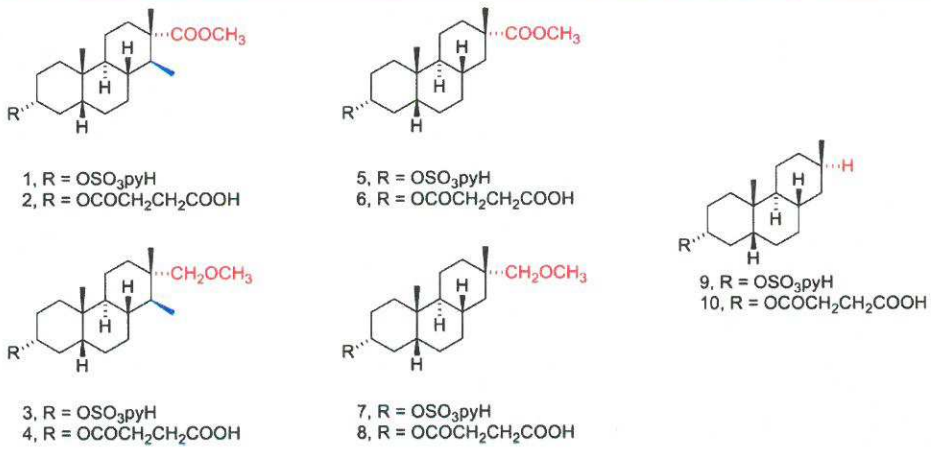

Figure 2. Overview of 2-sulfates (**1**, **3**, **5**, **7**, **9**) and 2-hemisuccinates (**2**, **4**, **6**, **8**, **10**) of perhydrophenanthrenes.

Scheme 1. Synthesis of Compounds 11−15[a]

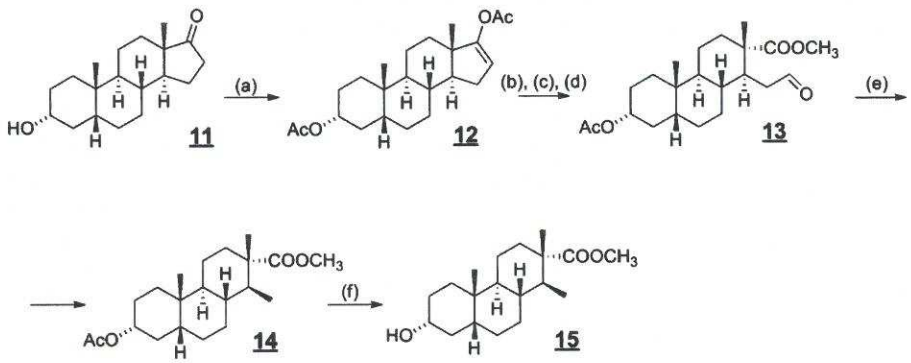

[a]Reagents and conditions: (a) $CH_3CO_2C(CH_3)=CH_2$, H_2SO_4; (b) O_3, CH_3COOH, DCM, −70 °C; (c) Me_2S, CH_3COOH, H_2O, rt; (d) CH_2N_2, Et_2O; (e) $[(C_6H_5)_3P]_3RhCl$, PhCN, 160 °C; (f) KOH, MeOH, H_2O.

substituent at the C-3 position.[11,12] Hence, the sulfate moiety was selected as the primary choice. With the intention to evaluate these new perhydrophenanthrene analogues as druglike candidates, we drew inspiration from the published data for pregnanolone C-3 hemisuccinate ester, a compound with neuroprotective activity both in vitro and in vivo models of neurodegeneration.[13,14] Thus, the hemisuccinate moiety was chosen to extend this SAR study.

The skeleton modifications were achieved by two types of degradation reactions of the steroidal D-ring: (i) enol-acetate formation at steroidal C-17 followed by ozonolysis (Scheme 1) and (ii) degradation of the steroidal D-ring via a perhydrophenathreneindoxyl derivative (Scheme 5).[15] These particular approaches allowed us to maintain/degrade the methyl substituent at position C-8 of the perhydrophenanthrene skeleton (compounds **1**−**4** vs compounds **5**−**10**) and moreover led to intermediates that allowed us to prepare compounds with differing oxidative states at C-7 (methyl esters **1**, **2**, **5**, **6** and methyl ethers **3**, **4**, **7**, **8**). These methyl ester and methyl ether moieties were anticipated to affect the biological activity. Finally, we combined the previously described approaches, degrading both substituents at C-7 and C-8 to prepare the unsubstituted, steroidal ABC ring-mimics **9** and **10**.

The biological activity of these new perhydrophenanthrene derivatives on NMDARs was evaluated on human embryonic kidney 293 (HEK293) cells transfected with plasmids encoding

DOI: 10.1021/acs.jmedchem.6b00079
J. Med. Chem. 2016, 59, 4724−4739

GluN1-1a/GluN2B/GFP genes. In addition, we have evaluated the action of compound **9** on recombinant GluN1/GluN2A-D, native NMDA, AMPA/kainate, and GABA receptors (GABARs) expressed in hippocampal neurons.

RESULTS AND DISCUSSION

Chemistry. The transformation of the steroidal skeleton into the perhydrophenanthrene was achieved by a series of degradation reactions (Scheme 1). First, the 17-keto group of the starting material (commercially available), 3α-hydroxy-5β-androstan-17-one (**11**), was converted to the enol acetate **12** while protecting the 3α-hydroxy group as an acetate ester (72%).[16] Second, the steroidal D-ring was opened by ozonolysis, followed by treatment with dimethyl sulfide in acetic acid, affording compound **13** in 88% yield. Finally, the Wilkinson decarbonylation led to compound **14** (69%), which was then hydrolyzed with potassium hydroxide in methanol into 7-hydroxy derivative **15** (94%).

Treatment of compound **15** with sulfur trioxide pyridine complex in $CHCl_3$ afforded 2-sulfate derivative **1** (35% yield, Scheme 2). 2-Hemisuccinate ester **2** (51%) was prepared by the reaction of compound **15** with succinic anhydride in the presence of DMAP and pyridine.

The methyl ester moiety of compound **14** (Scheme 3) was reduced by reflux with lithium aluminum hydride. Simultaneously, the acetate ester moiety was reduced to the hydroxyl group, affording compound **16** (73%). Then, the 2-hydroxy group of compound **16** was selectively oxidized to the ketone by sodium hypochlorite in acetic acid (**17**, 71%). The 2-oxo group was protected as a cyclic ketal (**18**, 85%), and the 7-hydroxymethyl moiety was converted into the methyl ether using NaH/methyl iodide. To avoid potential instability issues, the cyclic ketal moiety was directly deprotected, affording compound **20** (83%, 2 steps). Finally, sodium borohydride reduction in methanol at 0 °C gave 2-hydroxy derivative **21** in 80% yield.

Treatment of compound **21** with sulfur trioxide pyridine complex in $CHCl_3$ afforded 2-sulfate derivative **3** (33% yield). 2-Hemisuccinate ester **4** (83%) was prepared by the reaction of compound **21** with succinic anhydride in the presence of DMAP and pyridine (Scheme 4).

For the synthesis of compound **26** (Scheme 5), we used a previously reported methodology[15] utilizing the treatment of the steroidal 17-oxo group with *o*-nitrobenzaldehyde in a methanolic solution of potassium hydroxide. Starting from 3β-hydroxy-5β-androstan-17-one (commercially available, **22**), we have prepared steroidal indoxyl **23** (84%). Then, the 2-carboxylic moiety was protected as the methyl ester by ethereal diazomethane solution, giving compound **24** in 98% yield, and subsequently the 7-hydroxy group was protected as acetate ester (**25**, 89%). The synthetic strategy used to prepare compound **15** was also utilized to prepare compound **30** (Scheme 5). Thus, ozonolysis of compound **25** followed by treatment with dimethyl sulfide in acetic acid gave compound **26** in 80% yield. Then, Wilkinson decarbonylation led to compound **27** (71%) and the acetate protecting group was hydrolyzed with potassium hydroxide in methanol, affording 7-hydroxy derivative **28** (83%). The proper stereochemistry of the 7-hydroxy group was achieved by Jones oxidation (**29**, 84%) and selective reduction using lithium tri-*tert*-butoxyaluminum hydride, giving compound **30** in 71% yield.

Treatment of compound **30** with sulfur trioxide pyridine complex in $CHCl_3$ afforded 2-sulfate derivative **5** (47% yield). 2-Hemisuccinate ester **6** (52%) was prepared by the reaction of compound **30** with succinic anhydride in the presence of DMAP and pyridine (Scheme 5).

Scheme 2. Synthesis of Compounds 1 and 2[a]

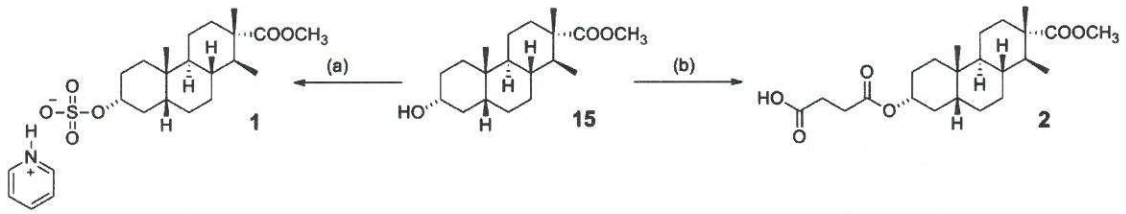

[a]Reagents and conditions: (a) py·SO_3 complex, $CHCl_3$, pyridine, rt; (b) succinic anhydride, DMAP, pyridine, 120 °C.

Scheme 3. Synthesis of compounds 14–21[a]

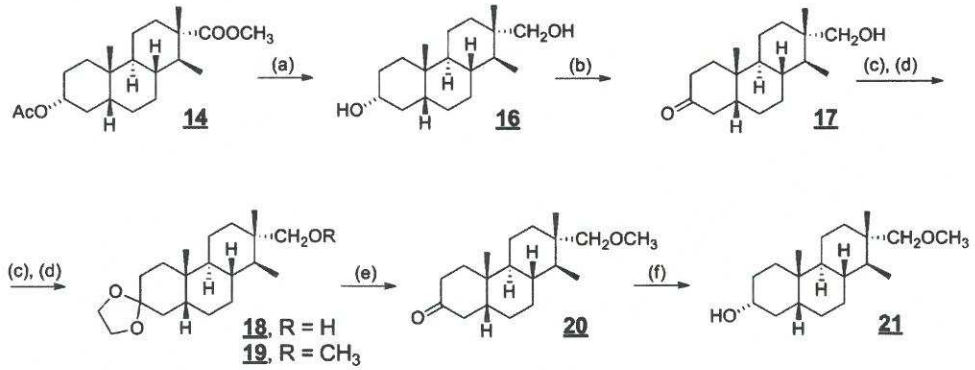

[a]Reagents and conditions: (a) (a) $LiAlH_4$, THF, reflux; (b) NaOCl, CH_3COOH, *i*-PrOH, rt; (c) $CH(OC_2H_5)_3$, ethylene glycol, TsOH·H_2O, benzene; (d) MeI, NaH, THF, 90 °C; (e) HCl, H_2O, acetone; (f) $NaBH_4$, MeOH, 0 °C.

DOI: 10.1021/acs.jmedchem.6b00079
J. Med. Chem. 2016, 59, 4724–4739

Scheme 4. Synthesis of Compounds 3 and 4[a]

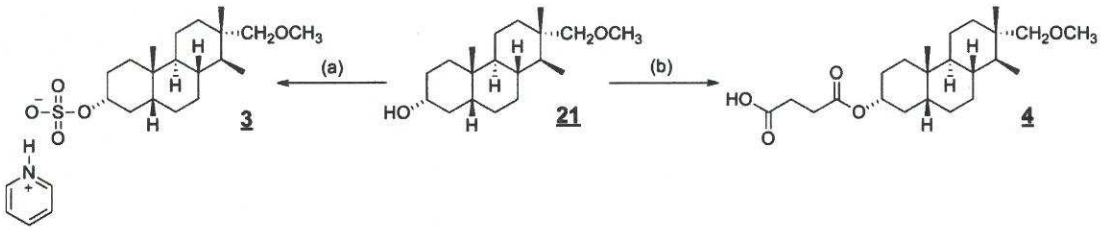

[a]Reagents and conditions: (a) py·SO_3 complex, $CHCl_3$, pyridine, rt; (b) succinic anhydride, DMAP, pyridine, 120 °C.

Scheme 5. Synthesis of Compounds 5 and 6[a]

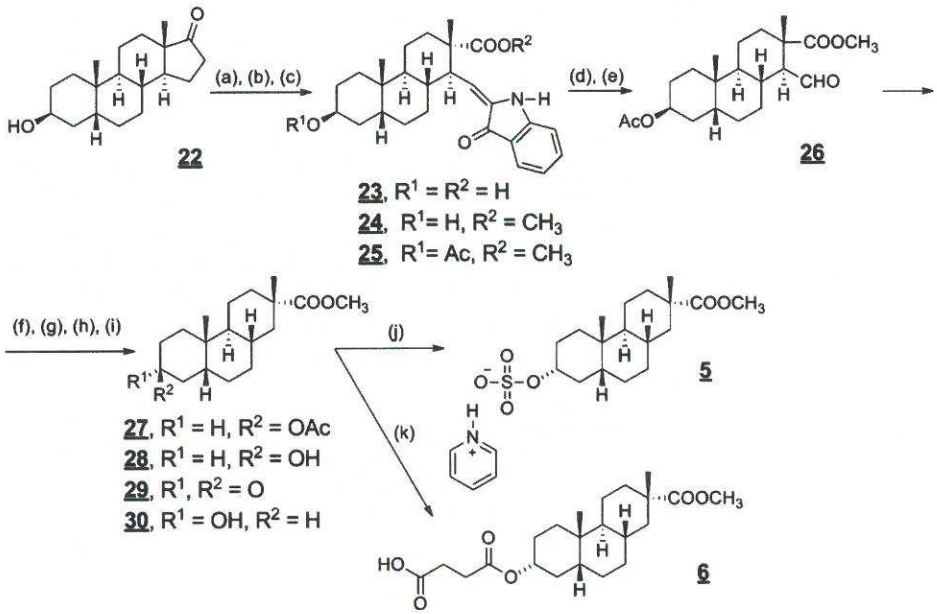

[a]Reagents and conditions: (a) *o*-nitrobenzaldehyde, KOH, MeOH, rt; (b) CH_2N_2, ether, 0 °C; (c) Ac_2O, DMAP, pyridine, rt; (d) O_3, AcOH, DCM, −70 °C; (e) Me_2S, AcOH, rt; (f) $[(C_6H_5)_3P]_3RhCl$, PhCN, 160 °C; (g) KOH, MeOH, H_2O; (h) Jones, acetone, rt; (i) $Li(O^tBu)_3AlH$, THF, −40 °C; (j) py·SO_3 complex, $CHCl_3$, pyridine, rt; (k) succinic anhydride, DMAP, pyridine, 120 °C.

The synthetic sequence used for the synthesis of compounds **14**−**21** was also used for the synthesis of compound **36** (Scheme 6): Compound **27** was treated with lithium aluminum hydride under reflux to afford compound **31** (92%). Then, the hydroxy group of compound **31** was selectively oxidized into the ketone by sodium hypochlorite in acetic acid (**32**, 60%), followed by cyclic ketal formation (**18**, 82%). The 7-hydroxymethyl moiety was converted into the methyl ether using NaH/methyl iodide (**34**, 92%), and the cyclic ketal moiety was deprotected by an aqueous solution of hydrochloric acid in acetone, affording compound **35** in (96%). Finally, sodium borohydride reduction in methanol at 0 °C gave 2-hydroxy derivative **36** in 70% yield. Treatment of compound **36** with sulfur trioxide pyridine complex in $CHCl_3$ afforded 2-sulfate derivative **7** (68% yield). 2-Hemisuccinate ester **8** (50%) was prepared by the reaction of compound **36** with succinic anhydride in the presence of DMAP and pyridine (Scheme 6).

Decarbonylation of the substituent at position C-2 to give compound **39a** (Scheme 7) was achieved via a 4-step reaction, utilizing Wilkinson decarbonylation. Both hydroxyl groups of compound **31** were oxidized by pyridinium chlorochromate using sodium acetate as a buffer, affording compound **37** in 89% yield. Wilkinson decarbonylation of compound **37** gave an inseparable mixture **38** of the desired 2-ketone and two isomeric olefins. Therefore, the crude mixture was next reduced by lithium tri-*tert*-butoxyaluminum hydride and then treated with sodium acetate buffered peracetic acid affording a mixture of epoxides **39b** and **39c** and desired compound **39a**, which was easily isolated by column chromatography (36%, 3 steps). Note that the Wilkinson decarbonylation proceeds in a stereospecific manner and stereochemistry of the β-methyl group at C-2 and C-7 of compounds **37** and **39** is retained without any epimerization. Such stereospecific decarbonylation using Wilkinson's catalyst has been already described in the literature.[17,18]

Analogously, we attempted to afford decarbonylation of compound **16** bearing 7-aldehyde moiety at position C-7. All attempts to proceed with Wilkinson decarbonylation (increased temperature, extended period of reaction time) failed, and only starting material was recovered. We assume that this was caused by steric hindrance of the C-7 and C-8 methyl groups. For the synthesis of C-8 methyl analogue of compound **39a**, the recently published methodology of total synthesis of steroidal skeleton[19] could be used.

DOI: 10.1021/acs.jmedchem.6b00079
J. Med. Chem. 2016, 59, 4724−4739

Scheme 6. Synthesis of Compounds 7 and 8[a]

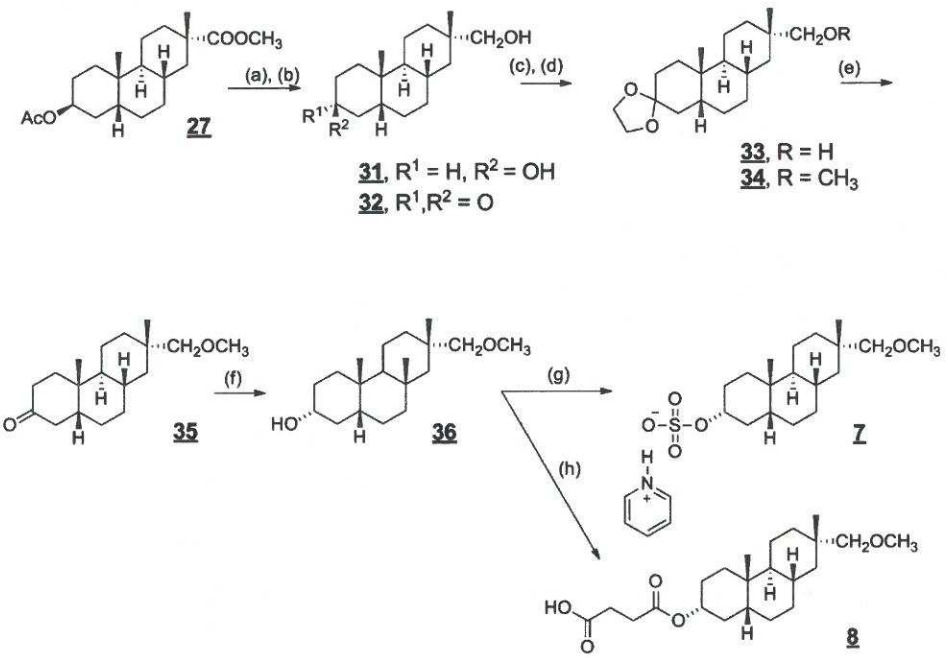

[a]Reagents and conditions: (a) $LiAlH_4$, THF, reflux; (b) NaOCl, CH_3COOH, *i*-PrOH, rt; (c) $CH(OC_2H_5)_3$, ethylene glycol, $TsOH{\cdot}H_2O$, benzene; (d) MeI, NaH, THF, 90 °C; (e) HCl, H_2O, acetone; (f) $NaBH_4$, EtOH, 0 °C; (g) $py{\cdot}SO_3$ complex, $CHCl_3$, pyridine, rt; (h) succinic anhydride, DMAP, pyridine, 120 °C.

Scheme 7. Synthesis of Compound 39a[a]

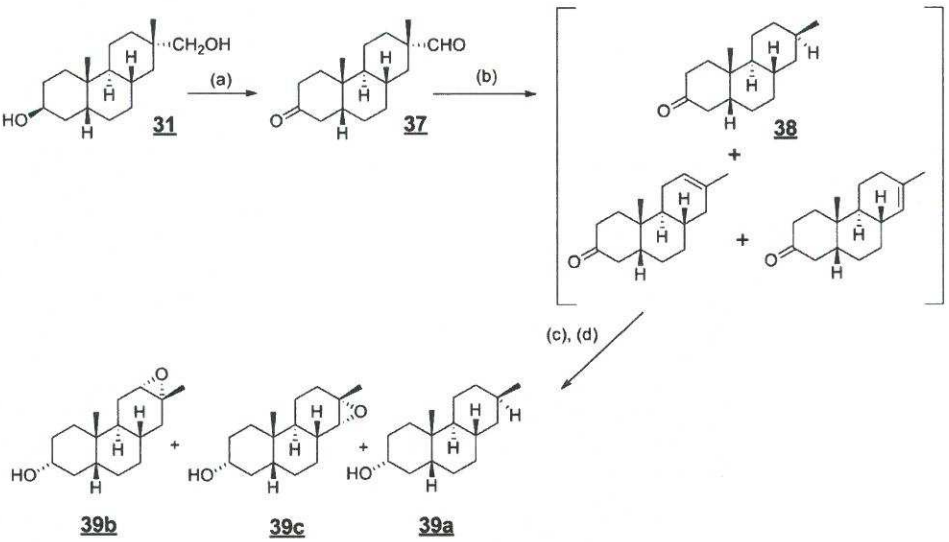

[a]Reagents and conditions: (a) CH_3COONa, PCC, DCM, rt; (b) $[(C_6H_5)_3P]_3RhCl$, PhCN, 160 °C; (c) $Li(O^tBu)_3AlH$, THF, −40 °C; (d) CH_3COONa, H_2O, CH_3COOOH, DCM, rt.

Finally, compound **39a** was treated with sulfur trioxide pyridine complex in $CHCl_3$, affording 2-sulfate derivative **9** (36% yield). 2-Hemisuccinate ester **10** (43%) was prepared by the reaction of compound **39a** with succinic anhydride in the presence of DMAP and pyridine (Scheme 8).

Biological Activity. To investigate the activity of pregnanolone sulfate and its analogues on NMDARs, cDNA encoding for the rat GluN1-1a and GluN2A-D subunits was co-transfected into HEK293 cells. Cells expressing GluN1-1a/GluN2B receptors were used to select the promising candidate for further detailed receptor selectivity analysis. As the amphipathic character of compounds **1**−**10** is similar to our previously published D-modified steroids,[10] we have used an identical approach for the assessment of the obtained data and calculation of the IC_{50}

DOI: 10.1021/acs.jmedchem.6b00079
J. Med. Chem. 2016, 59, 4724−4739

Scheme 8. Synthesis of Compounds 9 and 10[a]

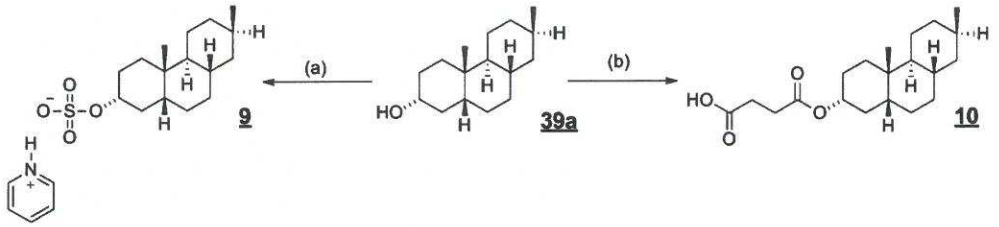

[a]Reagents and conditions: (a) py·SO_3 complex, $CHCl_3$, pyridine, rt; (b) succinic anhydride, DMAP, pyridine, 120 °C.

Table 1. Effect of Compounds 1–10 (Figure 2) on Current Responses of GluN1/GluN2B Receptors in HEK293 Cells to Glutamate

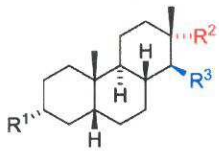

compd	R^1	R^2	R^3	IC_{50} (μM) (h = 1.2), (n)	concn (μM)
pregnanolone sulfate (Figure 1a)[a]	OSO_3pyH	$CH(COCH_3)(CH_2)_2$ ($R^2 = R^3$)	$CH(COCH_3)(CH_2)_2$ ($R^2 = R^3$)	24.6 ± 5.3 (n = 5)	100
5β-androstane-3α-yl sulfate (Figure 1b)[b]	OSO_3pyH	$CH_2CH_2CH_2$ ($R^2 = R^3$)	$CH_2CH_2CH_2$ ($R^2 = R^3$)	1.2 ± 0.2 (n = 11)	3
1	OSO_3pyH	$COOCH_3$	CH_3	74.6 ± 20.3 (n = 5)	50
2	$OCO(CH_2)_2COOH$	$COOCH_3$	CH_3	63.4 ± 5.5 (n = 3)	10
3	OSO_3pyH	CH_2OCH_3	CH_3	33.0 ± 6.3 (n = 5)	50
4	$OCO(CH_2)_2COOH$	CH_2OCH_3	CH_3	29.2 ± 0.7 (n = 3)	10
5	OSO_3pyH	$COOCH_3$	H	224.0 ± 28.0 (n = 4)	50
6	$OCO(CH_2)_2COOH$	$COOCH_3$	H	87.6 ± 47.0 (n = 4)	10
7	OSO_3pyH	CH_2OCH_3	H	77.0 ± 10.0 (n = 6)	50
8	$OCO(CH_2)_2COOH$	CH_2OCH_3	H	33.3 ± 10.9 (n = 7)	10
9	OSO_3pyH	H	H	15.6 ± 3.0 (n = 4)	10
10	$OCO(CH_2)_2COOH$	H	H	23.2 ± 6.4 (n = 5)	10

[a]See refs 12 and 20. [b]See ref 10.

values. In brief, the IC_{50} for the newly synthesized perhydrophenanthrene analogues was determined from a single dose of the compound using the following formula:

$$IC_{50} = [\text{compound}] \sqrt[h]{\frac{1 - I_1}{I_1}}$$

where I_1 is the relative degree of inhibition, [compound] is the perhydrophenanthrene analogue concentration used, and h stands for the Hill coefficient (fixed at 1.2). The IC_{50} value was determined for a minimum of two perhydrophenanthrene analogue doses, differing 3-fold in the concentration range. If the difference in the IC_{50} values was <10%, then the mean IC_{50} was calculated from the concentration most proximal to that inducing 50% inhibition. If the difference in the IC_{50} values determined for two doses was >10%, then the dose–response analysis was determined at lower concentrations to reach the formal criterion. In accordance with previous results, IC_{50} calculations were made assuming 100% inhibition at saturating concentration.[12,20] Table 1 summarizes the IC_{50} determined for perhydrophenanthrene analogues.

Ability of Perhydrophenanthrene Derivatives (1–10) To Modulate NMDAR Currents. Comparison of the IC_{50} values of simplified compounds **9** and **10** (IC_{50} = 15.6 ± 3.0 and 23.2 ± 6.4 μM, respectively), which bear only the ABC-ring motif of steroidal skeleton, to that of pregnanolone sulfate (Figure 1a, IC_{50} = 24.6 ± 5.3 μM) clearly indicates that this simplified framework is sufficient for maintaining inhibitory activity. However, the IC_{50} value of 5β-androstane-3α-yl sulfate (Figure 1b, IC_{50} = 1.2 ± 0.2 μM),[10] with an unsubstituted five-membered D-ring, gave a ~10-fold decrease in IC_{50} value relative to perhydrophenanthrene 2-sulfate (Figure 1c, i.e. compound **9**). Therefore, we can conclude that while complete degradation of the D-ring is an "allowed" modification, doing so may lead to a decrease in lipophilicity of the skeleton, which may affect the IC_{50} value in an undesirable manner.

Effect of the Methyl Ester vs Methyl Ether Moiety of Compounds 1–10 on Modulation of NMDARs. The obtained data (Table 1, Figure 2) show that compounds with a methyl ester moiety at position C-8 have comparatively higher IC_{50} values than their methyl ether analogues: **1** vs **3** (IC_{50} of 74.6 ± 20.3 and 33.0 ± 6.3 μM) and **2** vs **4** (IC_{50} of 63.4 ± 5.5 and 29.2 ± 0.7 μM), with methyl ethers **3** and **4** both showing a favorable ~2.2-fold decrease in the IC_{50} value. Accordingly, the comparison of **5** vs **7** (IC_{50} of 224.0 ± 28.0 and 77.0 ± 10.0 μM) and **6** vs **8** (IC_{50} of 87.6 ± 47.0 and 33.3 ± 10.9 μM) also shows a ~2.9-fold and ~2.6-fold decrease in the IC_{50} value, favoring methyl ether **7** and **8**, respectively.

Effect of the Sulfate vs Hemisuccinate Moiety of Compounds 1–10 on Modulation of NMDARs. In order to compare the effects of the sulfate and hemisuccinate moiety on the IC_{50} value, the compounds were divided into two groups.

DOI: 10.1021/acs.jmedchem.6b00079
J. Med. Chem. 2016, 59, 4724–4739

Those bearing the sulfate moiety, **1**, **3**, **5**, **7**, and **9**, and those bearing the hemisuccinate moiety, **2**, **4**, **6**, **8**, and **10** (Figure 2). Interestingly, while the comparison of sulfated vs hemisuccinate compounds with an oxygen substituent at position C-7 found all hemiester compounds to have lower IC_{50} values (**1** vs **2**, **3** vs **4**, **5** vs **6**, and **7** vs **8**), the opposite trend was seen for unsubstituted compounds **9** and **10** (IC_{50} of 15.6 ± 3.0 and 23.2 ± 6.4 μM), wherein the sulfated analogue has a ~50% lower IC_{50} value.

We have concluded that the structural degradation of the D-ring (methyl ester vs methyl ether) has provided new structural motifs that could be useful modifiers for various C-2 substituted analogues with miscellaneous hemiester moieties while maintaining the inhibitory activity. However, it is worth mentioning that the particular modulatory action of such derivatives may be further significantly affected by other aspects such as solubility, permeability, Lipinski rule of five, etc.

Effect of Compound 9 on Native and Recombinant NMDA Ionotropic Receptors. As compound **9** (Figure 2) was evaluated as the most potent modulator of a focused library of perhydrophenanthrene analogues (**1**–**10**), it was chosen for further biological evaluation. To investigate the subunit selectivity of compound **9** on the NMDARs, cDNAs encoding for the GluN1 and GluN2A-D subunits were co-transfected into HEK293 cells. Comparing the IC_{50} values of compound **9** at GluN1/GluN2A-D receptors revealed a significant difference between the IC_{50} value for GluN2B and those of the remaining GluN2A,C,D subunit containing receptors (ANOVA; $P \leq 0.007$). Notably, the comparison did not show any significant differences between the IC_{50} values for any combination of GluN2A,C,D. This indicates that the action of the perhydrophenanthrene analogue is weakly subunit dependent, as the GluN2B subunit is less sensitive to the perhydrophenanthrene analogue than other GluN2A,C,D subunit containing receptors (Figure 3 and Table 2). Similarly, no significant differences were found between native NMDARs expressed in cultured hippocampal neurons and recombinant GluN1/GluN2A-B receptors likely to be expressed in these cells.[21] In contrast to NMDAR response induced by 100 μM NMDA, the response of the α-amino-3-hydroxy-5-methyl-4-isoxazolepropionic acid receptor (AMPAR) induced by 100 μM AMPA, recorded in the presence of 10 μM cyclothiazide to block the receptor desensitization,[22] was significantly less sensitive to compound **9**. We have shown in our previous study[10] that the IC_{50} values of highly potent neurosteroid 17β-methyl-5β-androstan-3α-yl 3-sulfate are not significantly different for NMDAR and GABAR currents. On the contrary, the responses induced by 5 μM GABA were inhibited by compound **9** with IC_{50} values significantly different from that determined for NMDAR responses (Figure 4 and Table 3). This indicates that the steroidal D-ring plays a significant role for NMDAR/GABAR selectivity and gives a perspective for a further design of receptor selective neurosteroid based drugs. Despite this dual target effect, we have shown that neurosteroid derivatives with inhibitory effects on both NMDAR and GABAR show neuroprotective effects without psychomimetic symptoms.[5−8] We hypothesize that the inhibition of GABAR may help to minimize the undesired psychomimetic side effects; however the exact role of the inhibitory action on GABAR is unclear.

Computational Estimate of Thermodynamic Properties of Compounds 1−10. In the computational study, we have investigated the lipophilic qualities of the studied inhibitors in the context of their inhibitory effect, since the lipophilicity belongs to the basic characteristics of the neurosteroids, which influences their interactions with NMDAR.[10] The relevant physicochemical properties[23] of compounds **1**–**10** were estimated by quantum mechanics computational methods and

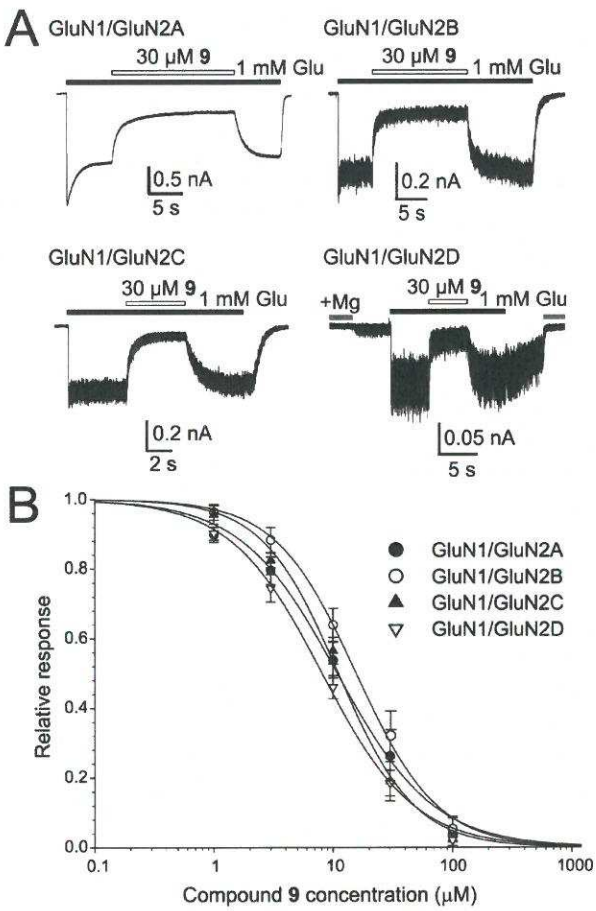

Figure 3. Effect of compound **9** on GluN1/GluN2A-D receptors. (A) Example of trace obtained from HEK293 cells transfected with cDNAs encoding GluN1/GluN2A (GluN2A), GluN1/GluN2B (GluN2B), GluN1/GluN2C (GluN2C), and GluN1/GluN2D (GluN2D) receptors. Compound **9** (30 μM) was applied simultaneously with 1 mM glutamate (duration of glutamate and perhydrophenanthrene analogue application is indicated by filled and open bars, respectively). The gray bar indicates application of ECS containing 1 mM Mg^{2+}. (B) Concentration−response curves for the effect of compound **9** at GluN1/GluN2A-D receptors. Data points are averaged values of normalized responses from minimum four HEK293 cells. Error bars represent SD. The relative glutamate induced responses (I) recorded in the presence of the perhydrophenanthrene analogue (1−100 μM) and determined in individual cells were fit to the following logistic equation: $I = 1/(1 + ([\text{perhydrophenanthrene analogue}]/IC_{50})^h)$, where IC_{50} is the concentration of compound **9** that produces a 50% inhibition of agonist-evoked current, [perhydrophenanthrene analogue] is the compound **9** concentration, and h is the apparent Hill coefficient.

Table 2. Effect of Compound 9 on Responses Induced in GluN1/GluN2A-D Receptors in HEK293 Cells to Glutamate

	IC_{50} ± SD (μM)	h ± SD	n
GluN1/GluN2A	10.9 ± 0.9	1.1 ± 0.1	6
GluN1/GluN2B	15.6 ± 0.8	1.3 ± 0.1	5
GluN1/GluN2C	11.1 ± 0.8	1.4 ± 0.1	4
GluN1/GluN2D	8.1 ± 0.5	1.1 ± 0.1	4

DOI: 10.1021/acs.jmedchem.6b00079
J. Med. Chem. 2016, 59, 4724−4739

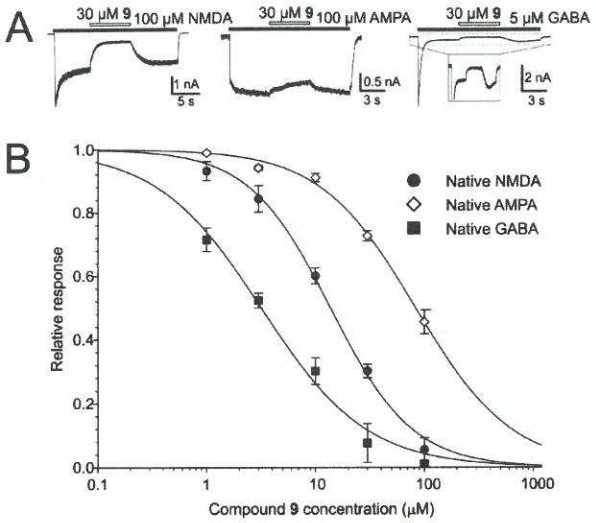

Figure 4. Effect of compound **9** on native AMPA/kainate, NMDA, and GABA receptors. (A) Example of trace obtained from cultured hippocampal neurons. Compound **9** (30 μM) was applied simultaneously with AMPA (100 μM), NMDA (100 μM), and GABA (5 μM) (duration of agonist and perhydrophenanthrene analogue application is indicated by filled and open bars, respectively). (B) Concentration–response curves for the compound **9** effect at AMPA, NMDA, and GABA receptors. Data points are averaged values of normalized responses from minimum of five cultured hippocampal neurons. Error bars represent SD. The relative agonist induced responses (I) recorded in the presence of the compound **9** (1–100 μM) and determined in individual cells were fit to the following logistic equation: $I = 1/(1 + ([\text{perhydrophenanthrene analogue}]/IC_{50})^h)$, where IC_{50} is the concentration of perhydrophenanthrene analogue that produces a 50% inhibition of agonist-evoked current, [perhydrophenanthrene analogue] is the perhydrophenanthrene analogue concentration, and h is the apparent Hill coefficient.

Table 3. Effect of Compound 9 on NMDA, AMPA, and GABA Receptor Responses in Hippocampal Neurons[a]

	$IC_{50} \pm$ SD (μM)	$h \pm$ SD	n
NMDAR	13.7 ± 0.9	1.2 ± 0.1	5
AMPAR	83.0 ± 5.2	1.0 ± 0.1	6
GABAR	3.1 ± 0.3	0.9 ± 0.1	6

[a]Hill coefficient was fixed at 1.2.

by physicochemical properties predictor. The computational results are summarized in Table 4.

The interactions of neurosteroid/neurosteroid-like compounds with NMDAR constitute the complicated process. First, the micelles occurring in the extracellular liquid fuse with the membrane; thereafter the single-molecules leave the membrane and finally enter the channel vestibule, which is the hydrophobic site of action.[9] The solvation free energy (ΔG_{solv}) estimates the behavior of the single-molecules in water and in n-octanol which represents the membrane environment. The negative values of ΔG_{solv} signify the free energy gained, and the positive values signify free energy required during the transfer from the first phase to the second phase occurs. The $\Delta G_{solv}^{octanol/water}$ values indicate that the charged molecules prefer water while the neutral ones n-octanol. These results suggest that the transfer between n-octanol and water is possible and it can be accompanied by the transition between the neutral and the ionized state.

The lipophilic character of compounds **1**–**10** was estimated by the log P and log D coefficients. The log P is defined as the logarithm of the ratio of neutral solute concentrations in n-octanol and water. On the other hand, the log D is the logarithm of the ratio of the sum of the concentrations of the neutral and the ionized form of the solute in each of the two phases and thus is depending on pH. As compounds **1**–**10** can be both ionized and neutral, the description of the lipophilicity by the log D is more appropriate.[24] The correlation between the calculated data and the experimental ΔG_{exp} data shows the two different groups of the compounds that evince the similar behavior only for ΔG_{solv} during the transfer from n-octanol to water (for the details, see the R^2 values in Table 4 and graphs in Supporting Information). The correlation for the sulfated analogues (**1**, **3**, **5**, **7**, **9**; R^2 = 0.80/0.77 (neutral/charged form) for $\Delta G_{solv}^{octanol/water}$; R^2 = 0.81/0.71 for log P/log D) is a little lower than for the hemisuccinate analogues (**2**, **4**, **6**, **8**, **10**; R^2 = 0.97/0.96 (neutral/charged form) for $\Delta G_{solv}^{octanol/water}$; R^2 = 0.93/0.28 for log P/log D). The correlation between log D values of the hemisuccinates and the ΔG_{exp} values has not found. This indicates that the real ratio of the neutral and ionized form of the solute of the hemisuccinates is different from calculated which is most likely caused by the different character of their functional hemisuccinate group in the aqueous and n-octanol environment (e.g., pK_a) as compared with sulfate moiety. The hemisuccinate analogues with slightly better inhibitory effect than the sulfated ones (except for the compound **10**) also evince the log D values lower and log P values higher than the sulfates. The sulfate and hemisuccinate analogues bearing ether of ester moiety on the skeleton have a similar inhibitory effect except for the significantly different values of the compound **5** (sulfate) and compound **10** (hemisuccinate). We hypothesize such phenomenon can be explained by conformation/deformation energy of the molecule during its motion inside NMDAR to the site of the action.[9] The hemisuccinate derivative is considerably more flexible, as it has more rotational C–C bonds and therefore more conformers. On the other hand, the sulfate moiety is rather rigid. The deformation energy is expressed as the difference of the single point energies between the global minimum (extended form) and the local minimum (compact conformer) in aqueous phase. The deformation energy is 5.08 kcal/mol for compound **5** and 13.47 kcal/mol for compound **6**. The results suggest that compound **6** inclines to compose the compact form through the intramolecular interaction of the aliphatic chain with the carbon skeleton and the ester moiety (Figure 5A). Although this intramolecular interaction has an adverse energy effect, it facilitates the passage of the molecule to the site of the inhibitory action.[9] On the contrary, the conformation of the compound **5** remains nearly extended (Figure 5B). Therefore, the conformers can have different ΔG_{solv} as well. The methyl ether of methyl ester substituents can also contribute to the conformation change of the particular molecule; e.g., compound **4** tends to form the compact conformer, probably just as all hemisuccinate analogues, but the methyl group at C-8 fastens the ether moiety at C-7. Therefore, the conformer is less clenched (Figure 5C) and the deformation energy is 11.82 kcal/mol.

A comparison of pregnanolone sulfate (IC_{50} = 24.6 μM, log P = 2.93, and log D = 1.67)[10] with compounds **9** (IC_{50} = 15.6 μM, log P = 3.11, and log D = 1.55) and **10** (IC_{50} = 23.2 μM, log P = 5.10, and log D = 1.04) shows better inhibitory effect of both compounds with log D vales lower and log P values higher than pregnanolone sulfate. Also, 5β-androstan-3α-yl sulfate (IC_{50} = 1.2 μM, log P = 4.07, and log D = 2.11)[10] evinces

DOI: 10.1021/acs.jmedchem.6b00079
J. Med. Chem. 2016, 59, 4724–4739

Table 4. Summary of the Computational Values of the Physicochemical Properties of Neuroactive Steroids[a]

compd	IC_{50} [μmol/L]	ΔG_{exp} [kcal/mol]	ΔG_{solv} [kcal/mol], transfer from vacuum to water: neutral	vacuum to water: charged	*n*-octanol to water: neutral	*n*-octanol to water: charged	log *P*	log *D*
1	74.6	−5.7	−20.70	−75.89	0.98	−6.58	2.10	1.47
2	63.4	−5.8	−23.96	−84.84	2.35	−6.03	4.08	0.97
3	33.0	−6.1	−16.21	−71.51	2.46	−5.02	3.07	1.49
4	29.2	−6.2	−19.55	−80.19	3.89	−4.40	5.25	0.99
5	224.0	−5.0	−20.77	−75.69	0.68	−6.84	1.71	1.18
6	87.6	−6.1	−23.99	−84.64	2.13	−6.26	3.92	0.68
7	77.0	−5.6	−17.18	−72.67	1.94	−5.55	2.74	1.21
8	33.3	−6.1	−20.58	−81.33	3.34	−5.02	4.98	0.70
9	15.6	−6.6	−14.15	−69.60	2.61	−4.95	3.11	1.55
10	23.2	−6.3	−17.46	−78.33	4.03	−4.33	5.10	1.04
correlation for sulfate derivatives (**1**, **3**, **5**, **7**, **9**)			0.78	0.78	0.80	0.77	0.81	0.71
correlation for hemiester derivatives (**2**, **4**, **6**, **8**, **10**)			0.93	0.93	0.97	0.96	0.93	0.28
correlation for compounds **1**−**10**			0.36	0.05	0.63	0.77	0.36	0.03

[a]The negative values of ΔG_{solv} signify the free energy gained and the positive values signify free energy required during the transfer from the first phase to the second phase. The correlation between ΔG_{exp} and ΔG_{solv}, log *P*, and log *D* is expressed as coefficient of determination (R^2).

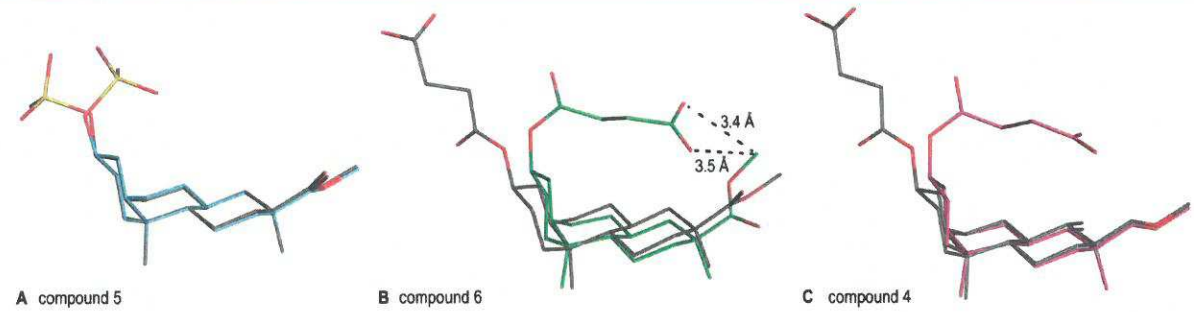

Figure 5. Conformers of compounds **4**−**6**. (A) Global (gray) and local minimum (blue) of compound **5**. (B) Global (gray) and local minimum (green) of compound **6**. (C) Global (gray) and local minimum (magenta) of compound **4**.

significantly better inhibitory activity than compounds **9** and **10**, while its log *D* value is significantly higher than in the cases of compounds **9** and **10** and it has lower log *P* value than compound **10**. Compound **9** (sulfate) shows the best inhibitory activity from series of compounds **1**−**10**, and it has the highest log *D* among the studied compounds and the highest log *P* among the sulfated analogues (Table 4). Compound **10** (hemisuccinate), which is the second best studied inhibitor, has the highest log *D* among the hemisuccinate analogues but lower log D value than the sulfated analogues; its log *P* is the second best among all compounds (Table 4). Our results denote the importance of the lipophilicity and the solvation free energy for the action of the steroids at the NMDAR, which is in an agreement with our previous results for sulfated steroids modified on the D-ring.[10] The results also indicate that the decrease of the lipophilicity related to the structural modification need not lead to the decrease of the inhibitory activity. In addition, the results point out the weighty effect of the conformation change of the steroids. Therefrom, we conclude that the results more likely suggest a different character of the inhibitory action of both inhibitory groups.

CONCLUSIONS

In this study, we have examined new compounds (**1**−**10**), with fully saturated phenanthrene skeletons that mimic the steroidal ABC ring system in order to evaluate their ability to modulate NMDAR-induced current. We have shown that the steroidal D-ring can be fully or partially degraded with a variety of polar substituents while maintaining inhibitory activity. We have also shown that the potency of these new inhibitors is comparable with the endogenous ligand, pregnanolone sulfate. In addition, we have shown that the degradation of the steroidal D-ring did not lead to NMDAR subtype selectivity and that there is a higher potency to inhibit NMDAR responses than AMPAR responses. Moreover, the IC_{50} values determined for GABAR responses were different from that determined for NMDAR responses for compound **9** that was evaluated as the most potent modulator of a focused library of perhydrophenanthrene analogues. This indicates that the steroidal D-ring plays a significant role for NMDAR/GABAR selectivity and gives a perspective for a further design of receptor selective neurosteroid-like based drugs. This new structural motif offers new prospects for the further modification and optimization of the pharmacological and pharmacokinetic properties of these neuroactive compounds. Finally, the computational analysis has defined the structure−function relationship of the steroid-like compounds in connection with their lipophilicity, solvation free energy, and conformation change which have a significant effect on the their inhibition of NMDAR responses.

EXPERIMENTAL SECTION

Chemistry. General. Melting points were determined on a micro-melting point apparatus Hund/Wetzlar (Germany) and are uncorrected.

DOI: 10.1021/acs.jmedchem.6b00079
J. Med. Chem. 2016, 59, 4724−4739

Optical rotations were measured in chloroform using an Autopol IV (Rudolf Research Analytical, Flanders, USA). $[\alpha]_D$ values are given in deg (10^{-1} deg cm^2 g^{-1}). IR spectra were recorded on a Bruker IFS 55 spectrometer (wavenumbers in cm^{-1}). Proton and carbon NMR spectra were measured on a FT NMR spectrometer Bruker AVANCE-400 (400 MHz, 101 MHz) in $CDCl_3$ with tetramethylsilane as the internal standard. Chemical shifts are given in ppm (δ scale). Coupling constants (J) and width of multiplets (W) are given in Hz. High resolution MS spectra were performed with a Q-Tof microspectrometer (Waters). Thin layer chromatography (TLC) was performed on silica gel (ICN Biochemicals). Preparative TLC (prep-TLC) was carried out on 200 mm × 200 mm plates coated with a 0.4 mm thick layer of the same material. For column chromatography neutral silica gel 60 μm (Merck) was used. Analytical samples were dried over phosphorus pentoxide at 50 °C/100 Pa. Anhydrous THF was prepared by distillation with benzophenone/Na immediately prior to use. Jones reagent has been prepared from chromium trioxide (67 g, 0.67 mmol) and a solution of sulfuric acid (58 mL of H_2SO_4 in 100 mL of water), and the mixture was diluted to 250 mL with water. The purity of the final compounds was assessed by a combination of NMR and on the basis of analysis LC–HR-MS, and the results were greater than 95%.

Computational Section. Preparation of Structures. The compounds were obtained by modeling the inhibitor as taken from the crystal structure (PDB code 3CAV[25]) using PyMOL program[26] and were relaxed by the RI-DFT/B-LYP/SVP method with the Turbomole program.[27] The empirical dispersion correction (D)[28] and COSMO continuum solvation model[29] were applied on the gradient optimization. The most stable local minima of the compounds were obtained by the quenched molecular dynamics simulation method with PM6-D3H4X.[30] The resulting geometries were minimized by the RI-DFT-D/B-LYP/SVP//COSMO method, and their single-point energies were calculated at the RI-DFT-D3/B-LYP/TZVPP//COSMO level.[31]

Computational Methods. The solvation free energy (ΔG_{solv}) of the perhydrophenanthrene analogues was calculated in the SMD continuum solvation model (the transfer from vacuum to water and from n-octanol to water)[32] at the HF/6-31G* level with the Gaussian program.[33] In this method, the single-point energies were computed at the identical molecular geometry both for the transfer from vacuum to water and from n-octanol to water. The partition coefficient (log P) was estimated on the basis of the change of the molecular conformation related to the transfer between n-octanol and water. The compounds were optimized at the M06-2X/6-31G* level in the SMD in the aqueous and n-octanol environments with the Gaussian program and log P was expressed as the difference between the total energies in water and in n-octanol[34] because this energy includes the internal energy of the molecule. The distribution coefficients (log D) of water/n-octanol phase were predicted at pH = 7.4, which is the physiological pH of blood serum, by the MarvinSketch program.[35] The estimated values of ΔG_{solv}, log P, and log D were compared with the experimental free energies (ΔG_{exp}) expressed from the IC_{50} values via the equation $\Delta G_{exp} = RT \ln(IC_{50})$. The linear regression was used for the description of the relationship between ΔG_{exp} and ΔG_{solv}, log P, and log D. The coefficient of determination (R^2), which is the square of the Pearson correlation coefficient between experimental and predicted data values, expresses how well the regression line approximates the real data points. It acquires values 0–1, where 0 means impossibility and 1 means a certainty.

Biological Activity. Electrophysiological experiments were performed on HEK293 cells transfected with plasmids encoding GluN1-1a/GluN2A-D/GFP genes and cultured hippocampal neurons as described previously.[17,36,37] Agonist-induced responses were voltage-clamped at a holding potential of −60 mV. Whole-cell voltage-clamp recordings were made with a patch-clamp amplifier (Axopatch 200B; Axon Instruments. Inc., Foster City, CA) after a serial resistance (<10 MΩ) and capacitance compensation of 80–90%. For the application of test and control solutions, a microprocessor controlled multibarrel fast-perfusion system was used, with a time constant of solution exchange around cells of ~10 ms. Agonist-induced responses were low-pass-filtered at 2 kHz, digitally sampled at 5 kHz, and analyzed with pClamp software, version 9.2 (Molecular Devices). Patch pipettes (3–5 MΩ) pulled from borosilicate glass were filled with Cs^+-based intracellular solution (ICS) containing the following (in mM): 120 gluconic acid, 15 CsCl, 10 BAPTA, 10 HEPES, 3 $MgCl_2$, 1 $CaCl_2$, and 2 ATP-Mg salt (pH-adjusted to 7.2 with CsOH). The extracellular solution (ECS) contained the following (in mM): 160 NaCl, 2.5 KCl, 10 HEPES, 10 glucose, 0.2 EDTA, 0.7 $CaCl_2$ (pH-adjusted to 7.3 with NaOH). NMDAR responses were induced by 1 mM glutamate (in recombinant receptors) and 100 μM NMDA (native receptors). The ECS used for native receptors had the same composition as the ECS used for recombinant receptors. For native NMDAR recordings ECS contained additionally 10 μM CNQX, 10 μM bicuculline, and 0.5 μM TTX. AMPA receptors currents were induced by 100 μM AMPA and the ECS contained additionally 50 μM D-AP5, 10 μM bicuculline, 0.5 μM TTX, and 10 μM cyclothiazide. GABA receptor responses were induced by 5 μM GABA, and the ECS contained additionally 50 μM D-AP5, 10 μM CNQX, and 0.5 μM TTX. Steroid/perhydrophenanthrene analogue solutions were prepared fresh as a stock solution of either 5 or 20 mM in dimethyl sulfoxide (DMSO) before each experiment (1% DMSO final concentration). The same concentration of DMSO was added in all extracellular solutions. Experiments were performed at room temperature (21–25 °C).

Experimental Data for Compounds 1–39a. General Procedure I: Sulfonation. A mixture of the hydroxy derivative (0.15 mmol) and sulfur trioxide pyridine complex (0.31 mmol) was dried in vacuo (25 °C, 100 Pa) for 30 min. Then, freshly dried chloroform (5 mL/50 mg) and dry pyridine (1 drop) were added and the reaction mixture was stirred at room temperature under inert atmosphere. The progress of the reaction was checked by TLC. Then, the reaction mixture was allowed to stand at −5 °C for 2 h, and the solid was filtered off through a plug of cotton wool in a glass Pasteur pipet. The filtrate was evaporated and dried (25 °C, 100 Pa) for 1 h to afford a mix of sulfate and sulfur trioxide pyridine complex. The crude material was dissolved in a minimal amount of freshly dried chloroform, allowed to stand at −5 °C for 2 h, and the solid was filtered off through a plug of cotton wool in a glass Pasteur pipet. The filtrate was evaporated and dried (25 °C, 100 Pa) for 1 h to afford the corresponding sulfate.

General Procedure II: Synthesis of Hemisuccinate Ester. A mixture of hydroxy derivative (100 mg, 0.32 mmol) and succinic anhydride (7 equiv) was dried overnight at 50 °C. Dry pyridine (4 mL/100 mg of starting material) and 4-(dimethylamino)pyridine (2.4 equiv) were added. The mixture was heated at 120 °C for 4 h. Then, it was poured into water and extracted with chloroform. Combined organic extracts were washed with brine and dried.

General Procedure III: Wilkinson's Decarbonylation. A mixture of carbonyl derivative (3.65 mmol) and tris(triphenylphosphine)-rhodium(I) chloride (1.1 equiv) in benzonitrile (25 mL/1.3 g of starting material) was heated under inert atmosphere at 160 °C for 20 h. The reaction mixture was cooled to room temperature and filtered to remove yellow solid. The filtrate was evaporated under reduced pressure. In addition, the yellow solid was washed with dichloromethane, and the washings were added to the first solid residue. The resulting mixture was filtered again to remove additional yellow solid which formed subsequently. The filtrate was again evaporated under reduced pressure.

General Procedure IV: Hydrolysis with Potassium Hydroxide. A solution of acetoxy derivative in methanol (5 mL/100 mg of starting material) was stirred overnight at room temperature with a solution of potassium hydroxide (4 equiv) in minimum amount of water. The reaction mixture was poured into water, the product was extracted with ethyl acetate, and combined organic extracts were washed with 5% aqueous solution of HCl, saturated aqueous solution of sodium bicarbonate, dried over Na_2SO_4, and evaporated under reduced pressure.

General Procedure V: LAH Reduction. A mixture of methyl ester derivative and $LiAlH_4$ (3 equiv) in THF (30 mL/1 g of starting material) was refluxed under atmosphere for 2 h. The excess of reagent was carefully quenched with aqueous solution of sodium sulfate, and inorganic material was filtered off, washing with ethyl acetate. The filtrate was washed with 5% aqueous solution of HCl, water, saturated aqueous solution of sodium bicarbonate, dried over Na_2SO_4, and evaporated.

General Procedure VI: Sodium Hypochlorite Oxidation. An aqueous solution of sodium hypochlorite (4.5%, 7.7 mL) was added into a solution of alcohol (2.09 mmol) in acetic acid (18 mL). After stirring at

DOI: 10.1021/acs.jmedchem.6b00079
J. Med. Chem. 2016, 59, 4724–4739

rt for 1 h, isopropanol (11 mL) was added and the mixture was stirred for another 30 min. Then, it was diluted with water and extracted with dichloromethane. The combined organic extracts were washed with brine, dried over Na_2SO_4 and the solvents evaporated.

General Procedure VII: Cyclic Ketal Formation. Ketone (550 mg, 1.98 mmol), triethyl orthoformate (7 equiv), and ethylene glycol (19 equiv) were dissolved in benzene (10 mL/550 mg of starting material), and $TsOH·H_2O$ (0.1 equiv) was added with stirring at rt. The reaction mixture was allowed to stand at 50 °C for 17 h, then cooled to rt, diluted with brine, and extracted with ethyl acetate. The combined organic extracts were washed with brine, dried over $MgSO_4$ and the solvents evaporated.

General Procedure VIII: Williamson Ether Synthesis. Cyclic ketal was dissolved in dry THF (30 mL/430 mg of starting material), and sodium hydride (60% dispersion in mineral oil, 10 equiv) was added. The mixture was stirred in an argon atmosphere at 90 °C for 1 h, then methyl iodide (8.5 equiv) was added and the mixture was stirred in an argon atmosphere at 90 °C for 5 h. After cooling, the product was extracted with ethyl acetate, combined organic extracts were washed with brine, dried over $MgSO_4$, and the solvents were evaporated under reduced pressure.

General Procedure IX: Sodium Borohydride Reduction. Ketone was dissolved in methanol (20 mL/400 mg of starting material), cooled to 0 °C (bath temperature), and sodium borohydride (1.1 equiv) was added. The mixture was stirred for 1 h at 0 °C, then warmed slowly to room temperature. The reaction was quenched with 5% aqueous HCl, the organic layer separated, and the aqueous fraction was extracted with ethyl acetate. The combined extracts were washed with saturated aqueous solution of sodium bicarbonate, dried with $MgSO_4$, and evaporated.

(2*R*,4a*S*,4b*S*,7*S*,8*S*,8a*S*,10a*R*)-7-(Methoxycarbonyl)-4a,7,8-trimethyltetradecahydrophenanthren-2-ylpyridinium Sulfate (1). Compound **1** was prepared according to general procedure I (sulfonation). Starting from compound **15** (104 mg, 0.34 mmol), compound **1** (55 mg, 35%) was obtained as a white solid: mp 168–169 °C (chloroform); $[\alpha]_D^{20}$ +10.9 (*c* 0.403, $CHCl_3$). ^1H NMR (400 MHz, CD_3OD): δ 0.71 (3H, d, *J* = 6.6, H_8-Me), 0.88 (3H, s, H_{4a}-18), 1.05 (3H, s, H_7-Me), 3.67 (3H, s, OCH_3), 4.47 (1H, tt, J_1 = 10.9, J_2 = 5.0, H-2), 8.02 (2H, m, H-2′ and H-4′, pyridinium), 8.49 (1H, t, *J* = 7.8, H-3′, pyridinium), 8.96–9.02 (2H, m, H-1′ and H-5′, pyridinium). ^{13}C NMR (101 MHz, CD_3OD): δ 179.30, 145.89 (C-1′, C-5′), 142.41, 127.33(C-2′, C-4′), 79.53, 51.85, 47.75, 42.37, 41.77, 39.62, 37.72, 37.09, 35.10, 34.73, 33.27, 27.91, 27.07, 25.55, 23.32, 20.06, 15.36, 14.64. IR spectrum ($CHCl_3$): 3140, 3100, 1490 (pyH); 1264, 1183, 1175, 1044, 954 (SO_3); 1720 (C=O); 1245, 1192 (C–O). MS: ESI *m*/*z* 387.2 (100%, M − pyH). HR-MS (ESI) *m*/*z*: for $C_{19}H_{31}O_6S$ [M − pyH] calcd, 387.18468; found, 387.18443.

4-(((2*R*,4a*S*,4b*S*,7*S*,8*S*,8a*S*,10a*R*)-7-(Methoxycarbonyl)-4a,7,8-trimethyltetradecahydrophenanthren-2-yl)oxy)-4-oxobutanoic Acid (2). Compound **2** was prepared according to general procedure II (synthesis of hemisuccinate ester). Starting from compound **15** (100 mg, 0.32 mmol), compound **2** (68 mg, 51%) was obtained as a white solid by column chromatography (10% acetone in petroleum ether): mp 145–147 °C (acetone/*n*-heptane); $[\alpha]_D^{20}$ +21.5 (*c* 0.21, $CHCl_3$). ^1H NMR (400 MHz, CD_3OD): δ 0.73 (3H, d, J, 6.7, H_8-Me), 0.90 (3H, s, H_{4a}-Me), 1.06 (3H, s, H_7-Me), 2.72–2.55 (4H, m, $OCCH_2CH_2CO$), 3.67 (3H, s, OCH_3), 4.70–4.81 (1H, m, H-2). ^{13}C NMR (101 MHz, CD_3OD): δ 179.30, 171.91, 74.93, 51.88, 47.77, 42.33, 41.58, 39.67, 37.74, 37.03, 34.87, 34.83, 32.11, 29.83, 29.47, 29.03, 27.06, 26.70, 25.51, 23.34, 20.09, 15.34, 14.63. IR spectrum ($CHCl_3$): 1724, 1718 (C=O); 1243, 1166 (COC); 3020, 1361 (CH_3); 2950 (CH_2). MS: ESI *m*/*z* 431.2 (100%, M + Na). HR-MS (ESI) *m*/*z*: for $C_{23}H_{36}O_6Na$ [M + Na] calcd, 431.2404; found, 431.2403.

(2*R*,4a*S*,4b*S*,7*S*,8*S*,8a*S*,10a*R*)-7-(Methoxymethyl)-4a,7,8-trimethyltetradecahydrophenanthren-2-ylpyridinium Sulfate (3). Compound **3** was prepared according general procedure I (sulfonation). Starting from compound **21** (78 mg, 0.26 mmol), compound **3** (40 mg, 33%) was obtained as a white solid: mp 159–161 °C (chloroform); $[\alpha]_D^{20}$ +4.0 (*c* 0.30, $CHCl_3$ + MeOH, 1.849:0.341). ^1H NMR (400 MHz, $CDCl_3$): δ 0.68 (3H, s, H_{4a}-Me), 0.75 (3H, d, *J* = 6.1, H_8-Me), 0.86 (3H, s, H_7-Me), 3.06 (2H, dd, J_1 = 112.6, J_2 = 9.1, CH_2O), 3.31 (3H, s, OCH_3), 4.46 (1H, tt, J_1 = 10.9, J_2 = 4.9, H-2), 8.01 (2H, m, H-2′ and H-4′, pyridinium), 8.49 (1H, t, *J* = 8.6, H-3′, pyridinium), 8.92–9.05 (2H, m, H-1′ and H-5′, pyridinium). ^{13}C NMR (101 MHz, $CDCl_3$): δ 145.84 (C-1′, C-5′), 142.41 (C-3′), 127.30 (C-2′, C-4′), 82.13, 79.89, 59.43, 41.84, 41.00, 39.82, 38.04, 37.70, 36.50, 35.10, 34.84, 33.25, 27.91, 27.31, 26.01, 23.43, 20.50, 15.95, 12.66. IR spectrum ($CHCl_3$): 2976, 2933 (CH_2OCH_3); 1263, 1255, 1183, 1044, 954 (SO_3). MS: ESI *m*/*z* 373.2 (100%, M − pyH). HR-MS (ESI) *m*/*z*: for $C_{19}H_{33}O_5S$ [M − pyH] calcd, 373.20542; found, 301.20542.

4-(((2*R*,4a*S*,4b*S*,7*S*,8*S*,8a*S*,10a*R*)-7-(Methoxymethyl)-4a,7,8-trimethyltetradecahydrophenanthren-2-yl)oxy)-4-oxobutanoic Acid (4). Compound **4** was prepared according to general procedure II (synthesis of hemisuccinate ester). Starting from compound **21** (70 mg, 0.24 mmol), compound **4** (78 mg, 83%) was obtained as a white solid by column chromatography (20% acetone in petroleum ether): mp 126–128 °C (acetone/*n*-heptane); $[\alpha]_D^{20}$ +6.5 (*c* 0.27, $CHCl_3$). ^1H NMR (400 MHz, $CDCl_3$): δ 0.68 (3H, s, H_{4a}-Me), 0.77 (3H, d, *J* = 6.1, H_8-Me), 0.88 (3H, s, H_7-Me), 2.51–2.76 (4H, m, $OCCH_2CH_2CO$), 3.08 (2H, dd, J_1 = 126.8, J_2 = 9.0, CH_2O), 3.33 (3H, s, OCH_3), 4.75 (1H, tt, J_1 = 11.3, J_2 = 4.8, H-2). ^{13}C NMR (101 MHz, $CDCl_3$) δ 177.20, 171.85, 81.97, 75.13, 59.44, 41.63, 40.80, 39.85, 38.03, 37.71, 36.45, 34.97, 34.85, 32.06, 29.45, 29.05, 27.29, 26.67, 25.97, 23.45, 20.55, 16.00, 12.63. IR spectrum ($CHCl_3$): 2935 (CH_2OCH_3); 1717 (C=O, COOH); 1100 (COC). MS: ESI *m*/*z* 393.3 (100%, M − 1). HR-MS (ESI) *m*/*z*: for $C_{23}H_{37}O_5$ [M − 1] calcd, 393.26465; found, 393.26433. For $C_{23}H_{38}O_5$ (394.3) calcd: 70.02%, C; 9.71% H. Found: 69.76%, C; 9.68%, H.

(2*R*,4a*S*,4b*S*,7*S*,8a*S*,10a*R*)-7-(Methoxycarbonyl)-4a,7-dimethyltetradecahydrophenanthren-2-yl Sulfate Pyridinium Salt (5). Compound **5** was prepared according general procedure I (sulfonation). Starting from compound **30** (100 mg, 0.34 mmol), compound **5** (72 mg, 47%) was obtained as a white solid: mp 115–118 °C (acetone/*n*-heptane); $[\alpha]_D^{20}$ +24.1 (*c* 0.23, $CHCl_3$). ^1H NMR (400 MHz, $CDCl_3$): δ 0.89 (3H, s, H_{4a}-Me), 1.17 (3H, s, H_7-Me), 3.65 (3H, s, OCH_3), 4.45 (1H, tt, J_1 = 11.0, J_2 = 5.0, H-2), 8.01 (2H, m, H-2′ and H-4′, pyridinium), 8.48 (1H, tt, J_1 = 7.9, J_2 = 1.5, H-3′, pyridinium), 8.99 (2H, dd, J_1 = 6.5, J_2 = 1.4, H-1′ and H-5′, pyridinium). ^{13}C NMR (101 MHz, $CDCl_3$): δ 179.39, 145.90 (C-1′, C-5′), 142.46 (C-3′), 127.33 (C-2′, C-4′), 79.55, 64.51, 51.87, 42.40, 42.33, 39.91, 34.83, 34.55, 34.48, 33.38, 31.84, 29.02, 28.01, 27.05, 23.38, 20.57, 20.29. IR spectrum ($CHCl_3$): 3140, 3099, 1490 (pyH); 1254, 1049, 957 (SO_3); 1435, 1380 (methyl); 1720 (C=O); 1245, 1192, 1013 (C–O). MS: ESI *m*/*z* 373.2 (100%, M − pyH). HR-MS (ESI) *m*/*z*: for $C_{18}H_{29}O_6S$ [M − pyH] calcd, 373.1690; found, 373.1688.

4-(((2*R*,4a*S*,4b*S*,7*S*,8a*S*,10a*R*)-7-(Methoxycarbonyl)-4a,7-dimethyltetradecahydrophenanthren-2-yl)oxy)-4-oxobutanoic Acid (6). Compound **6** was prepared according general procedure II (synthesis of hemisuccinate ester). Starting from compound **30** (60 mg, 0.20 mmol), compound **6** (42 mg, 52%) was obtained as a white solid by column chromatography (15% acetone in petroleum ether): mp 110–111 °C (acetone/*n*-heptane); $[\alpha]_D^{20}$ +23.3 (*c* 0.29, $CHCl_3$). ^1H NMR (400 MHz, $CDCl_3$): δ 0.91 (3H, s, H_{4a}-Me), 1.19 (3H, s, H_7-Me), 2.72–2.56 (4H, m, H-2′ and H-4′, succinate), 3.66 (3H, s, OCH_3), 4.755 (1H, tt, J_1 = 11.3, J_2 = 4.7, H-2). ^{13}C NMR (101 MHz, $CDCl_3$): δ 179.37, 176.38, 171.86, 75.02, 51.91, 42.42, 42.39, 42.15, 39.97, 34.70, 34.58, 34.48, 32.24, 31.89, 29.46, 29.02, 28.92, 27.06, 26.83, 23.42, 20.58, 20.36. IR spectrum ($CHCl_3$): 1718 (C=O); 2937 (OCH_3); 1242, 1126, 1102 (C–O). MS: ESI *m*/*z* 393.3 (100%, M − 1), 394.3 (25%, M). HR-MS (ESI) *m*/*z*: for $C_{22}H_{33}O_6$ [M − 1] calcd, 393.2283; found, 393.2283.

(2*R*,4a*S*,4b*S*,7*S*,8a*S*,10a*R*)-7-(Methoxymethyl)-4a,7-dimethyltetradecahydrophenanthren-2-ylpyridinium Sulfate (7). Compound **7** was prepared according general procedure I (sulfonation). Starting from compound **36** (98 mg, 0.35 mmol), compound **7** (105 mg, 68%) was obtained as a white solid: mp 132–134 °C (acetone/*n*-heptane); $[\alpha]_D^{20}$ +22.0 (*c* 0.26, $CHCl_3$). ^1H NMR (400 MHz, $CDCl_3$): δ 0.87 (3H, s, H_{4a}-Me), 0.88 (3H, s, H_7-Me), 2.99 (2H, s, CH_2O), 3.32 (3H, s, OCH_3), 4.46 (1H, tt, J_1 = 11.1, J_2 = 4.8, H-2), 8.00 (2H, m, H-2′ and H-4′, pyridinium), 8.47 (1H, tt, J_1 = 7.9, J_2 = 1.7, H-3′,

DOI: 10.1021/acs.jmedchem.6b00079
J. Med. Chem. 2016, 59, 4724–4739

pyridinium), 8.92–9.06 (2H, m, H-1′ and H-5′, pyridinium). ^{13}C NMR (101 MHz, $CDCl_3$): δ 145.78 (C-1′, C-5′), 142.52 (C-3′), 127.27 (C-2′, C-4′), 85.23, 79.75, 59.53, 43.20, 42.47, 40.43, 35.22, 34.94, 34.91, 34.63, 33.39, 32.01, 29.34, 28.01, 27.17, 23.47, 20.79, 20.51. IR spectrum ($CHCl_3$): 3140, 3099, 1490, 1024 (pyH); 1262, 1254, 1173, 1047 (SO_3); 1388, 1381 (methyl); 1109, 1101 (COC). MS: ESI *m/z* 359.3 (100%, M − pyH). HR-MS (ESI) *m/z*: for $C_{18}H_{31}O_5S$ [M − pyH] calcd, 359.1898; found, 359.1895.

4-(((2*R*,4a*S*,4b*S*,7*S*,8a*S*,10a*R*)-7-(Methoxymethyl)-4a,7-dimethyltetradecahydrophenanthren-2-yl)oxy)-4-oxobutanoic Acid (8). Compound **8** was prepared according general procedure II (synthesis of hemisuccinate ester). Starting from compound **36** (60 mg, 0.21 mmol), compound **8** (41 mg, 50%) was obtained as a white solid by column chromatography (10% acetone in petroleum ether): mp 107–109 °C (acetone/*n*-heptane); $[\alpha]_D^{20}$ +38.8 (*c* 0.26, $CHCl_3$). ^{1}H NMR (400 MHz, $CDCl_3$): δ 0.88 (3H, s, H_{4a}-Me), 0.90 (3H, s, H_7-Me), 2.53–2.72 (4H, m, $OCCH_2CH_2CO$), 3.01 (2H, s, CH_2OH), 3.34 (3H, s, OCH_3), 4.69–4.81 (1H, m, H-2). ^{13}C NMR (101 MHz, $CDCl_3$): δ 177.12, 171.83, 85.10, 75.17, 59.55, 43.06, 42.26, 40.44, 35.24, 34.78 (2x), 34.68, 32.24, 32.04, 29.45, 29.33, 29.04, 27.17, 26.81, 23.50, 20.85, 20.55. IR spectrum ($CHCl_3$): 1726, 1717 (C=O); 1385 (methyl); 1169, 1101 (COC). MS: ESI *m/z* 403.2 (100%, M + Na). HR-MS (ESI) *m/z*: for $C_{22}H_{36}O_5Na$ [M + Na] calcd, 403.2455; found, 403.2455.

(2*R*,4a*S*,4b*S*,7*R*,8a*S*,10a*R*)-4a,7-Dimethyltetradecahydrophenanthren-2-ylpyridinium Sulfate (9). Compound **9** was prepared according general procedure I (sulfonation). Starting from compound **39a** (108 mg, 0.46 mmol), compound **9** (66 mg, 36%) was obtained as a white solid: mp 147–149 °C (chloroform); $[\alpha]_D^{20}$ +25.3 (*c* 0.25, $CHCl_3$). ^{1}H NMR (400 MHz, $CDCl_3$): δ 0.88 (3H, s, H_7-Me), 0.92 (3H, d, *J* = 7.2, H_{4a}-Me), 4.46 (1H, tt, J_1 = 11.3, J_2 = 4.8, H-2), 8.00 (2H, m, H-2′ and H-4′, pyridinium), 8.47 (1H, t, *J* = 8.6, H-3′, pyridinium), 8.95–9.01 (2H, m, H-1′ and H-5′, pyridinium). ^{13}C NMR (101 MHz, $CDCl_3$): δ 145.78 (C-1′, C-5′), 142.51 (C-3′), 127.26 (C-2′, C-4′), 79.87, 42.52, 41.06, 40.74, 34.81, 34.70, 33.45, 32.72, 30.89, 29.40, 28.05, 27.81, 27.20, 23.54, 19.33, 18.30. IR spectrum ($CHCl_3$): 3140, 3099, 1490, 826 (pyH); 1263, 1255, 1173, 1047, 953 (SO_3); 1380 (methyl). MS: ESI *m/z* 315.3 (100%, M − pyH). HR-MS (ESI) *m/z*: for $C_{16}H_{27}O_4S$ [M − pyH] calcd, 315.1636; found, 315.1634.

4-(((2*R*,4a*S*,4b*S*,7*R*,8a*S*,10a*R*)-4a,7-Dimethyltetradecahydrophenanthren-2-yl)oxy)-4-oxobutanoic Acid (10). Compound **10** was prepared according general procedure II (synthesis of hemisuccinate ester). Starting from compound **39a** (65 mg, 0.27 mmol), compound **10** (40 mg, 43%) was obtained as a white solid by column chromatography (10% acetone in petroleum ether): mp 119–121 °C (acetone/*n*-heptane); $[\alpha]_D^{20}$ +43.9 (*c* 0.27, $CHCl_3$). ^{1}H NMR (400 MHz, $CDCl_3$): δ 0.90 (3H, s, H_7-Me), 0.94 (3H, d, *J* = 7.2, H_{4a}-Me), 2.74–2.54 (4H, m, H-2′ and H-4′), 4.75 (1H, tt, J_1 = 11.4, J_2 = 4.7, H-2). ^{13}C NMR (101 MHz, $CDCl_3$): δ 171.26, 171.83, 75.29, 42.32, 40.99, 40.78, 34.84, 34.53, 32.67, 32.33, 30.92, 29.45, 29.40, 29.06, 27.80, 27.20, 26.89, 23.58, 19.36, 18.31. IR spectrum ($CHCl_3$): 1727, 1716 (C=O); 1280 (C–O, dimer); 1232, 1176 (COC). MS: ESI *m/z* 335.4 (100%, M − H), 336.4 (22%, M). HR-MS (ESI) *m/z*: for $C_{20}H_{31}O_4$ [M − H] calcd, 335.2228; found, 335.2228.

(3*R*,5*R*,8*R*,9*S*,10*S*,13*S*,14*S*)-10,13-Dimethyl-2,3,4,5,6,7,8,9,10,11,12,13,14,15-tetradecahydro-1*H*-cyclopenta[*a*]phenanthrene-3,17-diyl Diacetate (12). A solution of 3α-hydroxy-5β-androstan-17-one **11** (18 g, 62 mmol), isopropenyl acetate (110 mL), and 2% H_2SO_4 in isopropenyl acetate (6.5 mL) was boiled for 2 h with slow fractionation of 30 mL. Further isopropenyl acetate (110 mL) and 2% H_2SO_4 in isopropenyl acetate (6.5 mL) were added. Again, the reaction mixture was boiled for 2 h with slow fractionation of 110 mL. Then, the solution was allowed to attain room temperature and poured into a mixture of petroleum ether (780 mL) and benzene (780 mL). The mixture was filtered over the column of aluminum oxide, washing with petroleum ether/benzene (1:1), and solvents were evaporated. The product was purified by column chromatography (2% ethyl acetate in petroleum ether/benzene (1:1)), affording compound **12** (16.7 g, 72%): ^{1}H NMR (400 MHz, CD_3OD): δ 0.87 (3H, s, H-18), 0.95 (3H, s, H-19), 2.03 (3H, s, OAc), 2.15 (3H, s, OAc), 4.65–4.78 (1H, m, H-3), 5.45 (1H, s, H-16).

(1*S*,2*S*,4a*S*,4b*S*,7*R*,8a*R*,10a*R*)-Methyl 7-Acetoxy-2,4b-dimethyl-1-(2-oxoethyl)tetradecahydrophenanthrene-2-carboxylate (13). A stirred solution of enol acetate **12** (5.0 g, 13.35 mmol) in dichloromethane and glacial acetic acid (13 mL) at −70 °C was ozonized until the blue color persisted. Dimethyl sulfide (2 mL, 27.37 mmol) in small portions, glacial acetic acid (130 mL), and water (28 mL) were added, and the solution was stirred for 18 h at room temperature. The product was extracted with dichloromethane (3 × 40 mL), the combined organic extracts were washed with water, dried over $MgSO_4$, and the solvents were evaporated. The residue was dissolved in ether, cooled to 0 °C, and esterified with ethereal solution of diazomethane. Chromatography on a column of silica gel (10% ethyl acetate in petroleum ether) gave 4.45 g (88%) of compound **13**: mp 151–153 °C (acetone/*n*-heptane); $[\alpha]_D^{20}$ −9.6 (*c* 0.24, CH_3OH). ^{1}H NMR (400 MHz, CD_3OD): δ 0.89 (3H, s, H_2-Me), 1.11 (3H, s, H_{4b}-Me), 2.02 (3H, s, OAc), 3.65 (3H, s, OCH_3), 4.66–4.76 (1H, m, H-7), 9.67 (1H, s, CHO). ^{13}C NMR (101 MHz, CD_3OD): δ 201.97, 178.37, 170.76, 74.08, 52.12, 47.59, 46.71, 41.69, 41.46, 39.83, 37.80, 36.78, 34.88, 34.77, 32.10, 26.96, 26.72, 26.31, 23.33, 21.55, 19.83, 15.56. IR spectrum ($CHCl_3$): 1721 (C=O); 2828 (CHO); 1385, 1364, 1435 (CH_3); 1253 (COO). MS: ESI *m/z* 401.3 (100%, M + Na). HR-MS (ESI) *m/z*: for $C_{22}H_{34}O_5Na$ [M + Na] calcd, 401.2299; found, 401.2297.

(1*S*,2*S*,4a*S*,4b*S*,7*R*,8a*R*,10a*S*)-Methyl-7-acetoxy-1,2,4b-trimethyltetradecahydrophenanthrene 2-Carboxylate (14). Compound **14** was prepared according to general procedure III (Wilkinson's decarbonylation). Starting from compound **13** (1.33 g, 3.65 mmol), compound **14** (1.33 g, 69%) was obtained by column chromatography (3% acetone in petroleum ether): mp 55–57 °C (aqueous ethanol); $[\alpha]_D^{20}$ 19.3 (*c* 0.31, CH_3OH). ^{1}H NMR (400 MHz, CD_3OD): δ 0.72 (3H, d, *J* = 6.7, H_1-Me), 0.89 (3H, s, H_2-Me), 1.06 (3H, s, H_{4b}-Me), 2.03 (3H, s, OAc), 3.66 (3H, s, OCH_3), 4.66–4.76 (1H, m, H-7). ^{13}C NMR (101 MHz, CD_3OD): δ 179.21, 170.77, 74.35, 51.85, 47.76, 42.36, 41.56, 39.66, 37.74, 37.05, 34.86 (2xC), 32.19, 27.07, 26.75, 25.52, 23.36, 21.58, 20.09, 15.34, 14.64. IR spectrum ($CHCl_3$): 1721 (C=O); 1467, 1386, 1024 (acetate); 1364, 1160 ($COOCH_3$). MS: ESI *m/z* 373.2 (100%, M + Na). HR-MS (ESI) *m/z*: for $C_{21}H_{34}O_4Na$ [M + Na] calcd, 373.2349; found, 373.2348.

(1*S*,2*S*,4a*S*,4b*S*,7*R*,8a*R*,10a*S*)-Methyl 7-Hydroxy-1,2,4b-trimethyltetradecahydrophenanthrene-2-carboxylate (15). Compound **15** was prepared according to general procedure IV (hydrolysis with potassium hydroxide). Starting from compound **14** (100 mg, 0.29 mmol), compound **15** (83 mg, 94%) was obtained: mp 144–146 °C (ethyl acetate/*n*-heptane); $[\alpha]_D^{20}$ +6.2 (*c* 0.33, $CHCl_3$). ^{1}H NMR (400 MHz, CD_3OD): δ 0.73 (3H, d, *J* = 6.7, H_1-Me), 0.89 (3H, s, H_2-Me), 1.06 (3H, s, H_{4b}-Me), 3.67 (3H, s, OCH_3), 3.58–3.68 (1H, m, H-7). ^{13}C NMR (101 MHz, CD_3OD): δ 179.26, 71.92, 51.87, 47.78, 42.32, 41.78, 39.69, 37.81, 37.06, 36.43, 35.18, 34.86, 30.73, 27.25, 25.62, 23.41, 20.10, 15.38, 14.66. IR spectrum ($CHCl_3$): 3020, 2942 (CH_3); 1720 (C=O); 3609, 1054, 1033 (OH); 1243 (COC). MS: ESI *m/z* 331.3 (100%, M + Na). HR-MS (ESI) *m/z*: for $C_{19}H_{32}O_3Na$ [M + Na] calcd, 331.2244; found, 331.2243.

(2*R*,4a*S*,4b*S*,7*S*,8*S*,8a*S*,10a*R*)-7-(Hydroxymethyl)-4a,7,8-trimethyltetradecahydrophenanthren-2-ol (16). Compound **16** was prepared according to general procedure V (LAH reduction). Starting from compound **14** (1.00 g, 2.86 mmol), compound **16** (585 mg g, 73%) was obtained: mp 141–143.5 °C (acetone/*n*-heptane); $[\alpha]_D^{20}$ −3.4 (*c* 0.33, $CHCl_3$). ^{1}H NMR (400 MHz, CD_3OD): δ 0.69 (3H, s, H_7-Me), 0.78 (3H, d, *J* = 6.3, H_8-Me), 0.89 (3H, s, H_{4a}-19), 2.03 (3H, s, OAc), 3.35 (2H, dd, J_1 = 92.2, J_2 = 10.9), 3.56–3.66 (1H, m, H-2). ^{13}C NMR (100 MHz, CD_3OD): δ 72.01, 71.74, 41.80, 40.57, 39.96, 38.21, 38.15, 36.46, 35.80, 35.17, 34.98, 30.79, 27.46, 26.13, 23.53, 20.49, 15.69, 12.61. IR ($CHCl_3$): 3628, 3616 (OH); 1035 (C-OH); 1380 (CH_3); 2935, 2866 (CH_2). MS: ESI *m/z*: 303.3 (100%, M + Na). HR-MS (ESI) *m/z*: for $C_{18}H_{32}O_2Na$ [M + Na] calcd; 303.2295, found, 303.2295.

(4a*S*,4b*S*,7*S*,8*S*,8a*S*,10a*R*)-7-(Hydroxymethyl)-4a,7,8-trimethyldodecahydrophenanthren-2(3*H*)-one (17). Compound **17** was prepared according to general procedure VI (sodium hypochlorite

DOI: 10.1021/acs.jmedchem.6b00079
J. Med. Chem. 2016, 59, 4724–4739

oxidation). Starting from compound **16** (585 mg, 2.09 mmol), compound **17** (412 mg, 71%) was obtained by column chromatography (4−10% acetone in petroleum ether) as an oily product: $[\alpha]_D^{20}$ −2.7 (*c* 0.29, $CHCl_3$). ^1H NMR (400 MHz, $CDCl_3$): δ 0.73 (3H, s, H_{4a}-Me), 0.82 (3H, d, J = 6.3, H_8-Me), 0.99 (3H, s, H_7-Me), 3.38 (2H, dd, J_1 = 101.4, J_2 = 10.9, CH_2OH). ^{13}C NMR (101 MHz, $CDCl_3$): δ 213.44, 71.47, 44.04, 42.38, 40.44, 40.22, 38.18, 37.87, 37.40, 36.89, 35.68, 35.34, 26.93, 25.51, 22.83, 20.80, 15.72, 12.56. IR spectrum ($CHCl_3$): 3630 (OH); 1032 (CCO); 1708 (C=O); 1383 (methyl); 2935, 2860 (CH_2). MS: ESI *m*/*z* 301.2 (100%, M + Na). HR-MS (ESI) *m*/*z*: for $C_{18}H_{30}O_2Na$ [M + Na] calcd, 301.21380; found, 301.21388.

((4a′*S*,4b′*S*,7′*S*,8′*S*,8a′*S*,10a′*R*)-4a′,7′,8′-Trimethyldodecahydro-1′*H*-spiro[[1,3]dioxolane-2,2′-phenanthren]-7′-yl)methanol (18). Compound **18** was prepared according to general procedure VII (cyclic ketal formation). Starting from compound **17** (550 mg, 1.98 mmol), compound **18** (542 mg, 85%) was obtained by column chromatography (10% ethyl acetate in petroleum ether with 1% of triethyl amine) as an oily product: $[\alpha]_D^{20}$ −2.7 (*c* 0.26, $CHCl_3$). ^1H NMR (400 MHz, $CDCl_3$): δ 0.70 (3H, s, H_{4a}-Me), 0.78 (3H, d, J = 6.3, H_8-Me), 0.92 (3H, s, H_7-Me), 3.35 (2H, dd, J_1 = 89, J_2 = 10.9, CH_2OH), 3.93 (4H, OCH_2CH_2O). ^{13}C NMR (101 MHz, $CDCl_3$): δ 110.20, 71.76, 64.37, 64.22, 40.60, 40.59, 39.28, 38.15, 38.00, 35.78, 35.66, 34.99, 34.00, 30.32, 27.02, 25.90, 23.27, 20.69, 15.69, 12.58. IR spectrum ($CHCl_3$): 3630 (OH); 1030 (COH); 2976, 2881, 1381 (methyl); 2928, 1471 (CH_2); 1471, 1094, 947 (OCH_2CH_2O). MS: CI *m*/*z* 321.2 (52%, M − H), 323.2 (54%, M + H). HR-MS (CI) *m*/*z*: for $C_{20}H_{33}O_3$ [M − H] calcd, 321.2433; found, 321.2430.

(4a*S*,4b*S*,7*S*,8*S*,8a*S*,10a*R*)-7-(Methoxymethyl)-4a,7,8-trimethyldodecahydrophenanthren-2(3*H*)-one (20). Compound **19** was prepared according to general procedure VIII (Williamson ether synthesis). Starting from compound **18** (430 mg, 1.33 mmol), compound **19** was prepared (400 mg). Then, the crude residue was dissolved in acetone (10 mL), and 5% aq HCl (150 μL) was added to the stirred solution. After 1 h of stirring at room temperature, the reaction mixture was quenched with saturated aqueous solution of sodium bicarbonate (10 mL) and the product was extracted with ethyl acetate. The combined organic fraction was washed with brine, dried over Na_2SO_4, and the solvents were evaporated affording compound **20** (322 mg, 83%, 2 steps) as an oily product: $[\alpha]_D^{20}$ −3.5 (*c* 0.37, $CHCl_3$/MeOH, 2.034:0.139). ^1H NMR (400 MHz, $CDCl_3$): δ 0.72 (3H, s, H_{4a}-Me), 0.80 (3H, d, J = 6.3, H_8-Me), 0.98 (3H, s, H_7-Me), 3.09 (2H, dd, J_1 = 129.6, J_2 = 9.1, CH_2O), 3.32 (3H, OCH_3). ^{13}C NMR (101 MHz, $CDCl_3$): δ 213.49, 81.78, 59.45, 44.12, 42.39, 40.75, 40.11, 37.76, 37.40, 36.94, 36.34, 35.32, 29.85, 26.94, 25.44, 22.80, 20.85, 15.99, 12.59. IR spectrum ($CHCl_3$): 1101 (COC); 1707 (C=O); 1382 (methyl); 2928 (CH_2). MS: CI *m*/*z* 293.2 (72%, M + H). HR-MS (CI) *m*/*z*: for $C_{19}H_{33}O_2$ [M + H] calcd, 293.2481; found, 293.2477.

(2*R*,4a*S*,4b*S*,7*S*,8*S*,8a*S*,10a*R*)-7-(Methoxymethyl)-4a,7,8-trimethyltetradecahydrophenanthren-2-ol (21). Compound **21** was prepared according to general procedure IX (sodium borohydride reduction). Starting from compound **20** (400 mg, 1.37 mmol), compound **21** (323 mg, 80%) was obtained by column chromatography (7% acetone in petroleum ether): mp 106−108 °C (acetone/*n*-heptane); $[\alpha]_D^{20}$ −9.2 (*c* 0.37, $CHCl_3$). ^1H NMR (400 MHz, $CDCl_3$): δ 0.69 (3H, s, H_{4a}-Me), 0.77 (3H, d, J = 6.4, H_8-Me), 0.88 (3H, s, H_7-Me), 3.07 (2H, dd, J_1 = 114.3, J_2 = 9.1, H-17), 3.32 (3H, OCH_3), 3.57−3.66 (1H, m, H-2). ^{13}C NMR (101 MHz, $CDCl_3$): δ 82.11, 72.04, 59.45, 41.85, 40.93, 39.88, 38.11, 37.71, 36.48, 36.46, 35.20, 34.96, 30.78, 27.48, 26.06, 23.52, 20.54, 15.96, 12.68. IR spectrum ($CHCl_3$): 3609 (OH); 2977 (CH_3); 1100 (COC). MS: ESI *m*/*z* 317.2 (100%, M + Na). HR-MS (ESI) *m*/*z*: for $C_{19}H_{34}O_2Na$ [M + Na] calcd, 317.24510; found, 317.24510.

(1*R*,2*S*,4a*S*,4b*S*,7*S*,8a*R*,10a*R*)-7-Hydroxy-2,4b-dimethyl-1-((*E*)-(3-oxoindolin-2-ylidene)methyl)tetradecahydrophenanthrene-2-carboxylic Acid (23). Solution of *o*-nitrobenzaldehyde (2.75 g) in methanol (25 mL) was added to a solution of 3β-hydroxy-5β-androstan-17-one (**22**) (5.0 g, 17.22 mmol) in 125 mL of 4% methanolic solution of potassium hydroxide. The reaction mixture was allowed to stand at room temperature for 18 h, and then a solution of potassium hydroxide (0.5 g) in methanol (1 mL) and solution of *o*-nitrobenzaldehyde (275 mg) in methanol (2.5 mL) were added. After 20 h the reaction mixture was concentrated ($^1/_3$ of the volume) and acidified with dilute hydrochloric acid (to pH ≈ 1). The resulting yellow precipitate was collected by filtration, washed with water, and dried affording compound **23** (6.1 g, 84%): mp 242−245 °C (methanol/water); $[\alpha]_D^{20}$ −182.2 (*c* 0.29, CH_3OH). ^1H NMR (400 MHz, CD_3OD): δ 0.98 (3H, s, H_{4b}-Me), 1.24 (3H, s, H_2-Me), 2.86 (1H, dd, J_1 = 11.4, J_2 = 10.0, H-1), 4.02−4.07 (1H, m, H-7), 5.81 (1H, d, J = 11.6, CH=C(CO−)NH), 6.79 (1H, t, J = 7.7), 6.93 (1H, d, J = 8.2), 7.41(1H, t, J = 7.7), 7.52 (1H, d, J = 7.7). ^{13}C NMR (101 MHz, CD_3OD): δ 187.72, 181.39, 155.99, 140.14, 137.88, 125.48, 121.86, 119.96, 117.67, 112.83, 67.68, 48.85, 48.09, 39.98, 38.12, 37.64, 37.60, 36.53, 34.23, 30.63, 28.55, 27.74, 27.64, 24.26, 21.01, 16.09. IR spectrum (KBr): 3445, 3343 (OH + NH); 1003 (C−OH); 2613 (OH, dimer); 1708 (C=O, dimer); 1693 (C=O, indolone); 1639 (C=C); 1613, 1486, 1468, 1448 (ring, indolone); 2976, 1383 (methyl). MS: ESI *m*/*z*: 446.3 (100%, M + Na), 424.3 (45%, M + H). HR-MS (ESI) *m*/*z*: for $C_{26}H_{33}O_4NNa$ [M + Na] calcd, 446.2302; found, 446.2301.

(1*R*,2*S*,4a*S*,4b*S*,7*S*,8a*R*,10a*R*)-Methyl 7-Hydroxy-2,4b-dimethyl-1-((*E*)-(3-oxoindolin-2-ylidene)methyl)tetradecahydrophenanthrene-2-carboxylate (24). A freshly prepared ethereal diazomethane was added to a suspension of acid **23** (5 g, 11.80 mmol) in ether while stirring at 0 °C. The progress of the reaction was checked by TLC. Then, the excess of diazomethane was evaporated affording compound **24** (5.1 g, 98%): mp 143−145 °C (methanol); $[\alpha]_D^{20}$ −208.1 (*c* 0.26, $CHCl_3$). ^1H NMR (400 MHz, $CDCl_3$): δ 0.97 (3H, s, H_{4b}-Me), 1.24 (3H, s, H_2-Me), 2.72 (1H, t, J = 10.7, H-1), 3.56 (1H, s, OCH_3), 4.12−4.14 (1H, m, H-7), 5.77 (1H, d, J = 11.1, CH=C(CO−)NH), 6.87 (1H, t, J = 7.7), 6.93 (1H, d, J = 8.2), 7.42 (1H, t, J = 7.7), 7.66 (1H, d, J = 7.7). ^{13}C NMR (101 MHz, $CDCl_3$): δ 185.93, 179.78, 154.04, 138.80, 136.25, 125.06, 122.45, 119.89, 116.52, 112.22, 67.03, 52.44 (OCH_3), 47.65, 47.54, 38.67, 37.81, 36.59, 36.33, 35.60, 33.58, 29.64, 28.00, 26.94, 26.51, 23.85, 19.91, 16.00. IR spectrum ($CHCl_3$): 3616 (OH); 1003 (COH); 1716 (C=O); 1249, 1032 (C−O); 1701 (C=O, indolone); 1644 (C=C); 1615, 1485, 1470, 1448 (ring, indolone); 2979, 1435, 1384 (methyl). MS: ESI *m*/*z* 460.4 (100%, M + Na), 438.4 (52%, M + H). HR-MS (ESI) *m*/*z*: for $C_{27}H_{36}O_4N$ [M + H] calcd, 438.2639; found, 438.2639.

(1*R*,2*S*,4a*S*,4b*S*,7*S*,8a*R*,10a*R*)-Methyl 7-Acetoxy-2,4b-dimethyl-1-((*E*)-(3-oxoindolin-2-ylidene)methyl)tetradecahydrophenanthrene-2-carboxylate (25). Acetic anhydride (46 mL) was added dropwise to a solution of methyl ester **24** (7.2 g, 16.45 mmol) and 4-(dimethylamino)pyridine (200 mg, 1.64 mmol) in pyridine (50 mL) at 0 °C while stirring. The reaction mixture was allowed to attain room temperature. After 2 h, excess of reagent was quenched with small portion of water (5 mL). The mixture was poured into 5% aqueous solution of HCl (150 mL) and extracted with ethyl acetate (3 × 50 mL). The combined organic extracts were washed with water, saturated aqueous solution of sodium bicarbonate and brine, dried over $MgSO_4$, and the solvents were evaporated affording compound **25** (7.0 g, 89%): mp 217−219 °C (methanol); $[\alpha]_D^{20}$ −221.1 (*c* 0.27, $CHCl_3$). ^1H NMR (400 MHz, $CDCl_3$): δ 0.98 (3H, s, H_{4b}-Me), 1.24 (3H, s, H_2-Me), 2.04 (3H, s, OAc), 2.73 (1H, t, J = 10.7, H-1), 3.56 (3H, s, OCH_3), 5.05−5.11 (1H, m, H-7), 5.76 (1H, d, J = 11.2, CH=C(CO−)NH), 6.87 (1H, t, J = 7.7), 6.93 (1H, d, J = 8.2), 7.42 (1H, t, J = 7.7), 7.65 (1H, d, J = 7.7). ^{13}C NMR (101 MHz, $CDCl_3$): δ 185.92, 179.66, 170.81, 154.04, 138.83, 136.28, 125.04, 122.43, 119.90, 116.31, 112.23, 70.55, 52.44, 47.61, 38.82, 47.46, 37.74, 37.14, 36.60, 35.35, 30.63, 30.46, 26.82, 26.36, 25.18, 23.80, 21.62, 19.90, 16.00. IR spectrum ($CHCl_3$): 1727 (C=O, OAc); 1261 (C−O, OAc); 1367 (CH_3, OAc); 1717 (C=O, COOMe); 1249, 1025 (C−O, COOMe); 1435 (CH_3, COOMe); 1702 (C=O, indolone); 1645 (C=C); 1615, 1485, 1470, 1448 (ring, indolone); 2979, 1385, 1379 (methyl). MS: ESI *m*/*z* 502.4 (100%, M + Na), 480.4 (30%, M + H). HR-MS (ESI) *m*/*z*: for $C_{29}H_{38}O_5$ [M + H] calcd, 480.2745; found, 480.2746.

(1*S*,2*S*,4a*S*,4b*S*,7*S*,8a*R*,10a*R*)-Methyl 7-Acetoxy-1-formyl-2,4b-dimethyltetradecahydrophenanthrene-2-carboxylate (26). A solution of **25** (7.0 g, 14.60 mmol) in dichloromethane (120 mL) and glacial acetic acid (15 mL) was ozonized at −70 °C until the blue color persisted. Then, dimethyl sulfide (3.4 mL) was added in

DOI: 10.1021/acs.jmedchem.6b00079
J. Med. Chem. 2016, 59, 4724−4739

small portions and the reaction mixture was stirred at room temperature for 1 h. Solvents were evaporated, the product was extracted with chloroform (3 × 60 mL), combined organic extracts were washed with water, dried over $MgSO_4$, and solvents were evaporated. The residue was purified by column chromatography on silica gel (6% acetone in petroleum ether), affording compound **26** (4.27 g, 80%). The structure of the compound was confirmed by NMR spectra, and then it was directly used into the next step: ^{1}H NMR (400 MHz, $CDCl_3$): δ 0.99 (3H, s, H_{4b}-Me), 1.24 (3H, s, H_2-Me), 2.04 (3H, s, OAc), 2.62 (1H, dd, J_1 = 11.2, J_2 = 3.0, H-14), 3.69 (3H, s, OCH_3), 5.05−5.11 (1H, m, H-7), 9.72 (1H, d, J = 3.0, CHO). ^{13}C NMR (101 MHz, $CDCl_3$): δ 204.77, 177.45, 170.75, 70.45, 60.18, 52.32, 38.45, 45.24, 36.97, 36.85, 35.27, 32.41, 30.58, 30.51, 26.33, 26.26, 25.10, 23.71, 21.61, 19.73, 16.89.

(2*S*,4a*S*,4b*S*,7*S*,8a*R*,10a*S*)-Methyl 7-Acetoxy-2,4b-dimethyltetradecahydrophenanthrene-2-carboxylate (27). Compound **27** was prepared according to general procedure III (Wilkinson's decarbonylation). Starting from compound **26** (2 g, 5.49 mmol), compound **27** (1.31 g, 71%) was obtained by column chromatography (3% acetone in petroleum ether) as an oily product: $[\alpha]_D^{20}$ +14.6 (c 0.31, $CHCl_3$). ^{1}H NMR (400 MHz, $CDCl_3$): δ 0.95 (3H, s, H_{4b}-Me), 1.19 (3H, s, H_2-Me), 2.05 (3H, s, OAc), 3.66 (3H, s, OCH_3), 5.03−5.1 (1H, m, H-7). ^{13}C NMR (101 MHz, $CDCl_3$): δ 179.37, 170.84, 70.79, 51.89, 42.43, 39.41, 37.56, 34.97, 34.49, 31.73, 30.65, 30.32, 28.82, 26.53, 25.21, 23.93, 21.65, 20.57, 20.51. IR spectrum ($CHCl_3$): 1722 (C=O); 2975, 2941, 1491, 1378 (methyl); 1262, 1243, 1025 (C-O). MS: ESI m/z 359.2 (100%, M + Na). HR-MS (ESI) m/z: for $C_{20}H_{32}O_4Na$ [M + Na] calcd, 359.2193; found, 359.2191.

(2*S*,4a*S*,4b*S*,7*S*,8a*R*,10a*S*)-Methyl 7-Hydroxy-2,4b-dimethyltetradecahydrophenanthrene-2-carboxylate (28). Compound **28** was prepared according general procedure IV (hydrolysis with potassium hydroxide). Starting from compound **27** (1.7 g, 5.1 mmol), compound **28** (1.24 g, 83%) was obtained as an oily product: $[\alpha]_D^{20}$ +13.5 (c 0.47, $CHCl_3$). ^{1}H NMR (400 MHz, $CDCl_3$): δ 0.94 (3H, s, H_{4b}-Me), 1.19 (3H, s, H_2-Me), 3.66 (3H, s, OCH_3), 4.07−4.15 (1H, m, H-7). ^{13}C NMR (101 MHz, $CDCl_3$): δ 179.45, 67.19, 51.87, 42.49, 39.26, 36.76, 35.22, 34.53, 33.54, 31.71, 29.50, 28.96, 28.06, 26.68, 23.97, 20.57, 20.51. IR spectrum ($CHCl_3$): 1719 (C=O); 1381 (methyl); 1245, 1033 (C-O). MS: ESI m/z 317.2 (100%, M + Na). HR-MS (ESI) m/z: for $C_{18}H_{30}O_3Na$ [M + Na] calcd, 317.2087; found, 317.2087.

(2*S*,4a*S*,4b*S*,8a*R*,10a*S*)-Methyl 2,4b-Dimethyl-7-oxotetradecahydrophenanthrene-2-carboxylate (29). Jones reagent was added to a solution of compound **28** (300 mg, 1.02 mmol) in acetone (5 mL). After stirring for 10 min at room temperature, the excess of reagent was decomposed with methanol (2 mL). Then, the reaction mixture was diluted with saturated aqueous solution of sodium bicarbonate and extracted with ethyl acetate (3 × 15 mL). Combined organic extracts were again washed with saturated aqueous solution of sodium bicarbonate, water, dried over Na_2SO_4, and evaporated affording compound **29** (250 mg, 84%): $[\alpha]_D^{20}$ +22.9 (c 0.38, $CHCl_3$). ^{1}H NMR (400 MHz, $CDCl_3$): δ 1.00 (3H, s, H_{4b}-Me), 1.22 (3H, s, H_2-Me), 3.66 (3H, s, OCH_3). ^{13}C NMR (101 MHz, $CDCl_3$): δ 213.04, 179.09, 51.93, 44.51, 42.38, 42.24, 40.24, 37.38, 36.61, 35.02, 34.38, 31.58, 29.83, 28.38, 26.66, 22.75, 20.60, 20.55. IR spectrum ($CHCl_3$): 1720, 1711 (C=O); 2980, 2934, 1465, 1435, 1383 (methyl); 1244, 1124 (C−O). MS: ESI m/z 315.2 (100%, M + Na). HR-MS (ESI) m/z: for $C_{18}H_{28}O_3Na$ [M + Na] calcd, 315.1931; found, 315.1929.

(2*S*,4a*S*,4b*S*,7*R*,8a*R*,10a*S*)-Methyl 7-Hydroxy-2,4b-dimethyltetradecahydrophenanthrene-2-carboxylate (30). A solution of compound **29** (100 mg, 0.34 mmol) in THF (10 mL) was cooled to −40 °C, and then lithium tri-*tert*-butoxyaluminum hydride (104 mg, 0.41 mmol) was added portionwise while stirring. After 2 h, the reaction mixture was allowed to attain room temperature and then quenched with 5% aqueous solution of HCl (20 mL). The product was extracted with $CHCl_3$ (3 × 15 mL), washed with saturated aqueous solution of sodium bicarbonate, brine, and dried over Na_2SO_4. Evaporation of solvents followed by chromatography (6% acetone in petroleum ether) gave compound **30** (71 mg, 71%) as an oily product: $[\alpha]_D^{20}$ +21.6 (c 0.19, $CHCl_3$). ^{1}H NMR (400 MHz, $CDCl_3$): δ 0.90 (3H, s, H_{4b}-Me), 1.18 (3H, s, H_2-Me), 3.66 (3H, s, OCH_3), 3.58−3.65 (1H, m, H-7). ^{13}C NMR (101 MHz, $CDCl_3$): δ 179.37, 71.94, 51.88, 42.41, 42.39, 42.33, 39.98, 36.52, 34.91, 34.66, 34.48, 31.91, 30.82, 29.10, 27.22, 23.46, 20.59, 20.33. IR spectrum ($CHCl_3$): 3608 (OH); 192, 1126, 1036, 1022 (C−O); 1720 (C=O); 2976, 2936, 1435, 1389 (methyl); 2936, 2865 (CH_2). MS: ESI m/z 317.2 (100%, M + Na). HR-MS (ESI) m/z: for $C_{18}H_{30}O_3Na$ [M + Na] calcd, 317.2087; found, 317.2088.

(2*S*,4a*S*,4b*S*,7*S*,8a*S*,10a*R*)-7-(Hydroxymethyl)-4a,7-dimethyltetradecahydrophenanthren-2-ol (31). Compound **31** was prepared according to general procedure V (LAH reduction). Starting from compound **27** (1.25 g, 3.71 mmol), compound **31** (905 mg g, 92%) was obtained: mp 139−140 °C (ethyl acetate/*n*-heptane); $[\alpha]_D^{20}$ +13.1 (c 0.29, $CHCl_3$). ^{1}H NMR (400 MHz, $CDCl_3$): δ 0.89 (3H, s, H_{4a}-Me), 0.95 (3H, s, H_7-Me), 3.24−3.30 (2H, m, CH_2OH), 4.08−4.14 (1H, m, H-2). ^{13}C NMR (101 MHz, $CDCl_3$): δ 74.89, 67.29, 42.71, 39.88, 39.08, 35.85, 35.34, 34.37, 33.59, 31.92, 29.62, 29.34, 28.10, 26.79, 24.09, 20.74, 20.32. IR spectrum ($CHCl_3$): 3630, 3618 (OH); 2936, 2863 (CH_2); 1031, 998 (C−OH). MS: ESI m/z 289.2 (100%, M + Na). HR-MS (CI) m/z: for $C_{17}H_{29}O_2$ [M − H] calcd, 265.2168; found, 265.2170.

(4a*S*,4b*S*,7*S*,8a*S*,10a*R*)-7-(Hydroxymethyl)-4a,7-dimethyldodecahydrophenanthren-2(3*H*)-one (32). Compound **32** was prepared according to general procedure VI (sodium hypochlorite oxidation). Starting from compound **31** (80 mg, 0.30 mmol), compound **32** (48 mg, 60%) was obtained by column chromatography (4−10% acetone in petroleum ether) as an oily product: $[\alpha]_D^{20}$ +26.1 (c 0.38, $CHCl_3$). ^{1}H NMR (400 MHz, $CDCl_3$): δ 0.92 (3H, s, H_{4a}-Me), 1.01 (3H, s, H_7-Me), 3.24−3.34 (2H, m, CH_2OH). ^{13}C NMR (101 MHz, $CDCl_3$): δ 213.36, 74.67, 44.65, 42.48, 42.47, 40.85, 37.42, 36.74, 35.86, 35.14, 34.24, 31.79, 28.77, 26.76, 22.85, 20.84, 20.28. IR spectrum ($CHCl_3$): 3630 (OH); 1034 (CCO); 1705 (C=O); 1383 (methyl); 2931, 2867 (CH_2). MS: ESI m/z 287.2 (100%, M + Na). HR-MS (ESI) m/z: for $C_{17}H_{28}O_2Na$ [M + Na] calcd, 287.1982; found, 287.1981.

((4a′*S*,4b′*S*,7′*S*,8a′*S*,10a′*R*)-4a′,7′-Dimethyldodecahydro-1′*H*-spiro[[1,3]dioxolane-2,2′-phenanthren]-7′-yl)methanol (33). Compound **33** was prepared according to general procedure VII (cyclic ketal formation). Starting from compound **32** (350 mg, 1.32 mmol), compound **33** (336 mg, 82%) was obtained by column chromatography (10% ethyl acetate in petroleum ether with 1% of triethyl amine) as an oily product: $[\alpha]_D^{20}$ +19.5 (c 0.11, $CHCl_3$). ^{1}H NMR (400 MHz, $CDCl_3$): δ 0.89 (3H, s, $H_{4a'}$-Me), 0.93 (3H, s, $H_{7'}$-Me), 3.26 (2H, s, CH_2OH), 3.93 (4H, s, OCH_2CH_2O). ^{13}C NMR (101 MHz, $CDCl_3$): δ 110.20, 74.94, 64.39, 64.22, 42.70, 41.22, 39.96, 35.82, 35.75, 34.77, 34.39, 33.86, 31.90, 30.37, 29.23, 26.86, 23.30, 20.74, 20.27. IR spectrum ($CHCl_3$): 3630, 3475 (OH); 1183, 1093, 1068, 947 (COCOC); 1382, 1364 (methyl); 1034 (CCO). MS: ESI m/z 331.3 (100%, M + Na). HR-MS (ESI) m/z: for $C_{19}H_{32}O_3Na$ [M + Na] calcd, 331.2244; found, 331.2246.

(4a′*S*,4b′*S*,7′*S*,8a′*S*,10a′*R*)-7′-(Methoxymethyl)-4a′,7′-dimethyldodecahydro-1′*H*-spiro[[1,3]dioxolane-2,2′-phenanthrene] (34). Compound **34** was prepared according to general procedure VIII (Williamson ether synthesis). Starting from compound **33** (250 mg, 0.81 mmol), compound **34** (240 mg, 92%) was prepared as an oily material: $[\alpha]_D^{20}$ +15.9 (c 0.41, $CHCl_3$). ^{1}H NMR (400 MHz, $CDCl_3$): δ 0.89 (3H, s, $H_{4a'}$-Me), 0.92 (3H, s, $H_{7'}$-Me), 2.99 (2H, s, CH_2O), 3.33 (3H, s, OCH_3), 3.93 (4H, m, OCH_2CH_2O). ^{13}C NMR (101 MHz, $CDCl_3$): δ 110.24, 85.24, 64.37, 64.21, 59.54, 43.20, 41.25, 39.85, 35.75, 35.23, 34.91, 34.76, 33.87, 31.87, 30.36, 29.19, 26.89, 23.30, 20.81, 20.73. IR spectrum ($CHCl_3$): 1186, 1094, 1068, 947 (COCOC); 2832, 1438, 1387, 1381, 1366 (methyl); 1102 (COC); 2928, 1449 (CH_2). MS: ESI m/z 345.3 (55%, M + Na). HR-MS (ESI) m/z: for $C_{20}H_{35}O_3$ [M + H] calcd, 323.2581; found, 323.2580.

(4a*S*,4b*S*,7*S*,8a*S*,10a*R*)-7-(Methoxymethyl)-4a,7-dimethyldodecahydrophenanthren-2(3*H*)-one (35). Cyclic ketal **34** (145 mg, 0.45 mmol) was dissolved in acetone (2.5 mL), and 5% aqueous solution of HCl (50 μL) was added to the stirred solution. After 1 h of stirring at room temperature, the reaction mixture was quenched with saturated aqueous solution of sodium bicarbonate (10 mL), and the product was extracted with ethyl acetate (3 × 5 mL). Combined organic fraction was washed with brine, dried over Na_2SO_4, and the solvents were evaporated affording compound **35** (120 mg, 96%) as an oily product: $[\alpha]_D^{20}$ + 24.8 (c 0.42, $CHCl_3$). ^{1}H NMR (400 MHz, $CDCl_3$): δ 0.91 (3H, s, H_{4a}-Me),

DOI: 10.1021/acs.jmedchem.6b00079
J. Med. Chem. 2016, 59, 4724−4739

1.00 (3H, s, H_7-Me), 3.02 (2H, s, CH_2OH), 3.34 (3H, s, OCH_3). ^{13}C NMR (101 MHz, $CDCl_3$): δ 213.45, 84.91, 59.55, 46.05, 42.93, 42.49, 40.71, 37.43, 36.77, 35.27, 35.13, 34.70, 31.77, 28.72, 26.79, 22.85, 20.85, 20.83. IR spectrum ($CHCl_3$): 1706 (C=O); 1102 (COC); 1383 (methyl); 2931, 2866 (CH_2). MS: ESI m/z 301.3 (100%, M + Na), 279.3 (20%, M + H). HR-MS (ESI) m/z: for $C_{18}H_{30}O_2Na$ [M + Na] calcd, 301.2138; found, 301.2138.

(2*R*,4a*S*,4b*S*,7*S*,8a*S*,10a*R*)-7-(Methoxymethyl)-4a,7-dimethyltetradecahydrophenanthren-2-ol (36). Compound **36** was prepared according to general procedure IX (sodium borohydride reduction). Starting from compound **35** (40 mg, 0.14 mmol), compound **36** (28 mg, 70%) was obtained by column chromatography (10% acetone in petroleum ether) as an oily product: $[\alpha]_D^{20}$ +19.7 (*c* 0.44, $CHCl_3$). ^1H NMR (400 MHz, $CDCl_3$): δ 0.88 (3H, s, H_{4a}-Me), 0.89 (3H, s, H_7-Me), 3.00 (2H, s, CH_2OH), 3.33 (3H, s, OCH_3), 3.58−3.67 (1H, m, H-2). ^{13}C NMR (101 MHz, $CDCl_3$): δ 85.22, 72.05, 59.55, 43.15, 42.44, 40.48, 36.53, 35.21, 35.00, 34.88, 34.73, 32.06, 30.82, 29.40, 27.32, 23.54, 20.79, 20.52. IR spectrum ($CHCl_3$): 3609, 3451 (OH); 1036 (C-OH); 2956, 2865, 1388, 1380 (methyl); 1102 (COC). MS: ESI m/z 303.4 (100%, M + Na). HR-MS (ESI) m/z: for $C_{18}H_{32}O_2Na$ [M + Na] calcd, 303.2295; found, 303.2295.

(2*S*,4a*S*,4b*S*,8a*R*,10a*S*)-2,4b-Dimethyl-7-oxotetradecahydrophenanthrene-2-carbaldehyde (37). Anhydrous sodium acetate (158 mg, 1.93 mmol) and pyridinium chlorochromate (826 mg, 3.86 mmol) were added to a solution of the **31** (320 mg, 1.20 mmol) in dichloromethane (20 mL). After stirring for 2 h at room temperature under inert atmosphere, the reaction mixture was diluted with ethyl acetate (60 mL), filtered through a column of alumina (12 g) and the product was eluted with ethyl acetate (3 × 10 mL). Collected filtrate was evaporated yielding 280 mg (89%) of aldehyde **37** which was used in the next reaction step without further purification: ^1H NMR (400 MHz, $CDCl_3$): δ 1.02 (3H, s, H_{4a}-Me), 1.12 (3H, s, H_7-Me), 9.41 (1H, s, CHO). ^{13}C NMR (101 MHz, $CDCl_3$) δ 212.89, 206.05, 44.45, 42.37, 40.38, 39.05, 37.35, 36.57, 35.11, 31.29, 31.17, 29.85, 28.45, 26.60, 22.81, 20.02, 17.58.

(2*R*,4a*S*,4b*S*,7*R*,8a*S*,10a*R*)-4a,7-Dimethyltetradecahydrophenanthren-2-ol (39a). Compound **39a** was prepared according general procedure III (Wilkinson's decarbonylation). Starting from compound **37** (280 mg, 1.07 mmol), inseparable mixture **38** of saturated derivative and two olefins (210 mg, 91.1:4.3:4.6 according to ^1H NMR) were obtained. The mixture was dissolved in THF (18 mL) and cooled to −40 °C. Then, lithium tri-*tert*-butoxyaluminum hydride (210 mg, 0.83 mmol) was added portionwise. After 2 h, the reaction mixture was allowed to attain room temperature and the reaction was quenched with 5% aqueous solution of HCl (20 mL). The products were extracted with $CHCl_3$ (3 × 15 mL), washed with saturated aqueous solution of sodium bicarbonate, brine, and dried over Na_2SO_4. Evaporation of the solvents afforded a mixture of hydroxy derivatives. The crude residue was dissolved in dichloromethane (15 mL), and a mixture of sodium acetate (66 mg, 0.81 mmol), water (0.6 mL), and peracetic acid (9% solution, 2.4 mL) was added. After stirring for 2 h at room temperature, sodium sulfite (5 mL) was added. The products were extracted with $CHCl_3$ (3 × 15 mL), combined organic extracts were washed with water, dried over $MgSO_4$, and solvents were evaporated. Purification by column chromatography (5% acetone in petroleum ether) afforded white waxy solid **39a** (90 mg, 36%, 3 steps): $[\alpha]_D^{20}$ +24.0 (*c* 0.30, $CHCl_3$). ^1H NMR (400 MHz, $CDCl_3$): δ 0.79 (3H, s, H_7-Me), 0.84 (3H, d, J = 7.3, H_{4a}-18), 3.53 (1H, tt, J_1 = 11.1, J_2 = 4.7, H-2). ^{13}C NMR (101 MHz, $CDCl_3$): δ 72.11, 42.49, 41.02, 40.80, 36.58, 34.86, 34.81, 32.70, 30.95, 30.87, 29.48, 27.81, 27.37, 23.62, 19.35, 18.31. IR spectrum ($CHCl_3$): 3608 (OH); 2958, 2866 (methyl); 1038, 1029 (C-OH). MS: CI m/z 236.2 (8%, M), 235.2 (15%, M − H). HR-MS (CI) m/z: for $C_{16}H_{27}O$ [M − H] calcd, 235.2062; found, 235.2070.

■ ASSOCIATED CONTENT

Supporting Information

The Supporting Information is available free of charge on the ACS Publications website at DOI: 10.1021/acs.jmedchem.6b00079.

Correlation between the experimental ΔG_{exp} values and ΔG_{solv} (transfer from *n*-octanol to water for neutral systems) and log *P* and log *D* values for compounds **1**−**10** (PDF)

Molecular formula strings (CSV)

■ AUTHOR INFORMATION

Corresponding Author

*Phone: +420-220-183-273. Fax: +420-220-183-578. E-mail: kudova@uochb.cas.cz.

Author Contributions

‖The computational analysis was done by M.N.

Notes

The authors declare no competing financial interest.

■ ACKNOWLEDGMENTS

This work was supported by Grant TE01020028 Center for Development of Original Drugs from the Technology Agency of the Czech Republic, Grant 303/12/1464 from the Grant Agency of the Czech Republic, Research Project of the RVO 67985823, RVO 61388963, and LQ1604 NPU II provided by MEYS and CZ.1.05/1.1.00/02.0109 BIOCEV provided by ERDF and MEYS. The Czech Science Foundation [Grant P208/12/G016] supported the computational study by M.N. We thank M. Sedlackova and D. Hybsova for their excellent technical assistance. The authors thank Dr. Laurel McGrane for language corrections.

■ ABBREVIATIONS USED

NMDA, *N*-methyl-D-aspartate; TLC, thin layer chromatography

■ REFERENCES

(1) Citri, A.; Malenka, R. C. Synaptic plasticity: multiple forms, functions, and mechanisms. *Neuropsychopharmacology* **2008**, *33*, 18−41.

(2) Hynd, M. R.; Scott, H. L.; Dodd, P. R. Glutamate-mediated excitotoxicity and neurodegeneration in Alzheimer's disease. *Neurochem. Int.* **2004**, *45*, 583−595.

(3) Dong, X.; Wang, Y.; Qin, Z. Molecular mechanism of excitotoxicity and their relevance to pathogenesis of neurodegenerative disease. *Acta Pharmacol. Sin.* **2009**, *30*, 379−387.

(4) Lai, T. W.; Zhang, S.; Wang, Y. T. Excitotoxicity and stroke: Identifyion novel targets for neuroprotection. *Prog. Neurobiol.* **2014**, *115*, 157−188.

(5) Rambousek, L.; Bubenikova-Valesova, V.; Kacer, P.; Syslova, K.; Kenney, J.; Holubova, K.; Najmanova, V.; Zach, P.; Svoboda, J.; Stuchlik, A.; Chodounska, H.; Kapras, V.; Adamusova, E.; Borovska, J.; Vyklicky, L.; Vales, K. Cellular and behavioural effects of a new steroidal inhibitor of the N-methyl-D-aspartate receptor 3α5β-pregnanolone glutamate. *Neuropharmacology* **2011**, *61*, 61−68.

(6) Kleteckova, L.; Tsenov, G.; Kubova, H.; Stuchlik, A.; Vales, K. Neuroprotective Effect of the 3α5β-pregnanolone glutamate treatment in the model of focal cerebral ischemia in immature rats. *Neurosci. Lett.* **2014**, *564*, 11−15.

(7) Holubova, K.; Nekovarova, T.; Pistovcakova, J.; Sulcova, A.; Stuchlik, A.; Vales, K. Pregnanolone glutamate, a novel use-dependent NMDA receptor inhibitor, exerts antidepressant-like properties in animal models. *Front. Behav. Neurosci.* **2014**, *8*, 130.

(8) Vyklicky, V.; Smejkalova, T.; Krausova, B.; Balik, A.; Korinek, M.; Borovska, J.; Horak, M.; Chvojkova, M.; Kleteckova, L.; Vales, K.; Cerny, J.; Nekardova, M.; Chodounska, H.; Kudova, E.; Vyklicky, L. Preferential inhibition of tonically over phasically activated NMDA receptors by pregnane derivatives. *J. Neurosci.* **2016**, *36*, 2161−2175.

(9) Vyklicky, V.; Krausova, B.; Cerny, J.; Balik, A.; Zapotocky, M.; Novotny, M.; Lichnerova, K.; Smejkalova, T.; Kaniakova, M.; Korinek, M.; Petrovic, M.; Kacer, P.; Horak, M.; Chodounska, H.; Vyklicky, L.

DOI: 10.1021/acs.jmedchem.6b00079
J. Med. Chem. 2016, 59, 4724−4739

Block of NMDA receptor channels by endogeneous neurosteroids: implications for the agonist induced conformational states of the channel vestibule. *Sci. Rep.* **2015**, *5*, 10935.
(10) Kudova, E.; Chodounska, H.; Slavikova, B.; Budesinsky, M.; Nekardova, M.; Vyklicky, V.; Krausova, B.; Svehla, P.; Vyklicky, L. A new class of potent N-methyl-D-aspartate receptor inhibitors: Sulfated neuroactive steroids with lipophilic D-ring modifications. *J. Med. Chem.* **2015**, *58*, 5950−5966.
(11) Weaver, C. E.; Land, M. B.; Purdy, R. H.; Richards, K. G.; Gibbs, T. T.; Farb, D. H. Geometry and charge determine pharmacological effects of steroids on N-methyl-D-aspartate receptor-induced Ca^{2+} accumulation and cell death. *J. Pharmacol. Exp. Ther.* **2000**, *293*, 747−754.
(12) Borovska, J.; Vyklicky, V.; Stastna, E.; Kapras, V.; Slavikova, B.; Horak, M.; Chodounska, H.; Vyklicky, L., Jr. Access of inhibitory neurosteroids to the NMDA receptor. *Br. J. Pharmacol.* **2012**, *166*, 1069−1083.
(13) Weaver, C. E., Jr.; Marek, P.; Park-Chung, M.; Tam, S. W.; Farb, D. H. Neuroprotective activity of a new class of steroidal inhibitors of the N-methyl-D-aspartate receptor. *Proc. Natl. Acad. Sci. U. S. A.* **1997**, *94*, 10450−10454.
(14) Lapchak, P. A. The neuroactive steroid 3-alpha-ol-5-beta-pregnan-20-one hemisuccinate. A selective NMDA receptor antagonist improves behavioral performance following spinal cord ischemia. *Brain Res.* **2004**, *997*, 152−158.
(15) Hassner, A.; Haddadin, M. J.; Catsoulacos, P. Steroidal indoxyl, indoles, and quinolines. *J. Org. Chem.* **1966**, *31*, 1363−1369.
(16) Hewett, C. L. 16-Heterocyclic amino steroids. U.S. Patent 3,026,318, March 20, 1962.
(17) Zhang, H.; Padwa, A. Application of a stereospecific $RhCl(PPh_3)_3$ decarbonylation reaction for the total synthesis of 7-(±)-deoxypancratistatin. *Tetrahedron Lett.* **2006**, *47*, 3905−3908.
(18) Hu, Y.; Zorumski, C. F.; Covey, D. F. Neurosteroid analogues: Structure-activity studies of benz[e]indene modulators of $GABA_A$ receptor function. 1. The effect of 6-methyl substitution on the electrophysiological activity of 7-substituted benz[e]indene-3-carbonitriles. *J. Med. Chem.* **1993**, *36*, 3956−3967.
(19) Kapras, V. Synthesis and Properties of Neuroactive Steroids. Ph.D. Dissertation Charles University, Prague, Czech Republic, 2016.
(20) Petrovic, M.; Sedlacek, M.; Horak, M.; Chodounska, H.; Vyklicky, L., Jr. 20-oxo-5beta-pregnan-3alpha-yl sulfate is a use-dependent NMDA receptor inhibitor. *J. Neurosci.* **2005**, *25*, 8439−8450.
(21) Flint, A. C.; Maisch, U. S.; Weishaupt, J. H.; Kriegstein, A. R.; Monyer, H. NR2A Subunit expression shortens NMDA receptor synaptic currents in developing neocortex. *J. Neurosci.* **1997**, *17*, 2469−2476.
(22) Patneau, D. K.; Vyklicky, L., Jr.; Mayer, M. L. Hippocampal neurons exhibit cyclothiazide-sensitive rapidly desensitizing responses to kainate. *J. Neurosci.* **1993**, *13*, 3496−3509.
(23) Faassen, F.; Kelder, J.; Lenders, J.; Onderwater, R.; Vromans, H. Physicochemical properties and transport of steroids across Caco-2 cells. *Pharm. Res.* **2003**, *20*, 177−186.
(24) Kah, M.; Brown, C. D. LogD: Lipophilicity for ionisable compounds. *Chemosphere* **2008**, *72*, 1401−1408.
(25) Faucher, F.; Cantin, L.; Luu-The, V.; Labrie, F.; Breton, R. The crystal structure of human Delta4-3-ketosteroid 5beta-reductase defines the functional role of the residues of the catalytic tetrad in the steroid double bond reduction mechanism. *Biochemistry* **2008**, *47*, 8261−8270.
(26) *The PyMOL Molecular Graphics System*, version 1.5.0.4; Schrödinger, LLC.
(27) Ahlrichs, R.; Bar, M.; Haser, M.; Horn, H.; Kolmel, C. Electronic structure calculations on workstation computers: The program system Turbomole. *Chem. Phys. Lett.* **1989**, *162*, 165−169.
(28) Jurecka, P.; Cerny, J.; Hobza, P.; Salahub, D. Density functional theory augmented with an empirical dispersion term. Interaction energies and geometries of 80 noncovalent complexes compared with ab initio quantum mechanics calculations. *J. Comput. Chem.* **2007**, *28*, 555−569.
(29) Klamt, A.; Schüürmann, G. COSMO: A new approach to dielectric screening in solvents with explicit expressions for the screening energy and its gradient. *J. Chem. Soc., Perkin Trans. 2* **1993**, *5*, 799−805.
(30) (a) Rezac, J.; Fanfrlik, J.; Salahub, D.; Hobza, P. Semiempirical quantum chemical PM6 method augmented by dispersion and H-bonding correction terms reliably describes various types of noncovalent complexes. *J. Chem. Theory Comput.* **2009**, *5*, 1749−1760. (b) Rezac, J.; Hobza, P. Advanced corrections of hydrogen bonding and dispersion for semiempirical quantum mechanical methods. *J. Chem. Theory Comput.* **2012**, *8*, 141−151.
(31) Grimme, S.; Antony, J.; Ehrlich, S.; Krieg, H. A Consistent and accurate *ab initio* parametrization of pensity functional dispersion correction (DFT-D) for the 94 elements H-Pu. *J. Chem. Phys.* **2010**, *132*, 154104−154119.
(32) Marenich, A. V.; Cramer, C. J.; Truhlar, D. G. Universal solvation model based on solute electron density and on a continuum model of the solvent defined by the bulk dielectric constant and atomic surface tensions. *J. Phys. Chem. B* **2009**, *113*, 6378−6396.
(33) Frisch, M. J.; Trucks, G. W.; Schlegel, H. B.; Scuseria, G. E.; Robb, M. A.; Cheeseman, J. R.; Scalmani, G.; Barone, V.; Mennucci, B.; Petersson, G. A.; Nakatsuji, H.; Caricato, M.; Li, X.; Hratchian, H. P.; Izmaylov, A. F.; Bloino, J.; Zheng, G.; Sonnenberg, J. L.; Hada, M.; Ehara, M.; Toyota, K.; Fukuda, R.; Hasegawa, J.; Ishida, M.; Nakajima, T.; Honda, Y.; Kitao, O.; Nakai, H.; Vreven, T.; Montgomery, J. A., Jr.; Peralta, J. E.; Ogliaro, F.; Bearpark, M.; Heyd, J. J.; Brothers, E.; Kudin, K. N.; Staroverov, V. N.; Kobayashi, R.; Normand, J.; Raghavachari, K.; Rendell, A.; Burant, J. C.; Iyengar, S. S.; Tomasi, J.; Cossi, M.; Rega, N.; Millam, N. J.; Klene, M.; Knox, J. E.; Cross, J. B.; Bakken, V.; Adamo, C.; Jaramillo, J.; Gomperts, R.; Stratmann, R. E.; Yazyev, O.; Austin, A. J.; Cammi, R.; Pomelli, C.; Ochterski, J. W.; Martin, R. L.; Morokuma, K.; Zakrzewski, V. G.; Voth, G. A.; Salvador, P.; Dannenberg, J. J.; Dapprich, S.; Daniels, A. D.; Farkas, Ö.; Foresman, J. B.; Ortiz, J. V.; Cioslowski, J.; Fox, D. J. *Gaussian 09*; Gaussian Inc., Wallingford, CT, 2009.
(34) Kolar, M.; Fanfrlik, J.; Lepsik, M.; Forti, F.; Luque, F. J.; Hobza, P. Assessing the accuracy and performance of implicit solvent models for drug molecules: conformational ensemble approaches. *J. Phys. Chem. B* **2013**, *117*, 5950−5962.
(35) Marvin was used for drawing, displaying, and characterizing chemical structures, substructures, and reactions. *Marvin*, version 15.1.19; ChemAxon, 2015 (http://www.chemaxon.com).
(36) Cais, O.; Sedlacek, M.; Horak, M.; Dittert, I.; Vyklicky, L., Jr. Temperature dependence of NR1/NR2B NMDA receptor channels. *Neuroscience* **2008**, *151*, 428−438.
(37) Korinek, K.; Sedlacek, M.; Cais, O.; Dittert, I.; Vyklicky, L. Temperature dependence of N-methyl-D-aspartate receptor excitatory postsynaptic currents. *Neuroscience* **2010**, *165*, 736−748.

DOI: 10.1021/acs.jmedchem.6b00079
J. Med. Chem. 2016, 59, 4724−4739